



Universiteit  
Leiden  
The Netherlands

## Platinum electrochemistry through a magnifying glass

Jacobse, L.

### Citation

Jacobse, L. (2018, November 29). *Platinum electrochemistry through a magnifying glass*. Retrieved from <https://hdl.handle.net/1887/67104>

Version: Not Applicable (or Unknown)

License: [Licence agreement concerning inclusion of doctoral thesis in the Institutional Repository of the University of Leiden](#)

Downloaded from: <https://hdl.handle.net/1887/67104>

**Note:** To cite this publication please use the final published version (if applicable).

Cover Page



Universiteit Leiden



The handle <http://hdl.handle.net/1887/67104> holds various files of this Leiden University dissertation.

**Author:** Jacobse, L.

**Title:** Platinum electrochemistry through a magnifying glass

**Issue Date:** 2018-11-29

# **Platinum Electrochemistry** *through a magnifying glass*

## **Proefschrift**

ter verkrijging van  
de graad van Doctor aan de Universiteit Leiden,  
op gezag van Rector Magnificus prof. mr. C.J.J.M. Stolker  
volgens besluit van het College voor Promoties  
te verdedigen op donderdag 29 november 2018  
klokke 10:00

door

**Leon Jacobse**

geboren te Rotterdam in 1990

## **Promotiecomissie:**

**Promotor:** Prof. dr. M.T.M. Koper

**Co-promotor:** Dr. M.J. Rost

**Overige leden:** Prof. dr. J.M. Feliu (University of Alicante)  
Prof. dr. rer. nat. A. Stierle (DESY NanoLab)  
Dr. I.M.N. Groot  
Prof. dr. J.M. van Ruitenbeek  
Prof. dr. H.S. Overkleef

ISBN: 978-94-92679-62-8

Printing: Print Service Ede

Cover illustration: Alexandra Hunts ([www.alexandrahunts.com](http://www.alexandrahunts.com))

*Avoid the crowd. Do your own thinking independently.  
Be the chess player, not the chess piece.*

Ralph Charell

# Table of Contents

<b>1</b>	<b>Introduction</b>	<b>1</b>
1.1	Electrochemistry . . . . .	2
1.2	Model catalysts . . . . .	4
1.3	Electrochemical scanning probe microscopy . . . . .	6
1.4	Outline of this thesis . . . . .	8
<b>2</b>	<b>Electrochemical nanoisland growth on Pt(111)</b>	<b>11</b>
2.1	Electrochemical measurements . . . . .	13
2.2	<i>in situ</i> EC-STM . . . . .	14
2.3	Quantitative roughness analysis . . . . .	19
2.4	Conclusions . . . . .	25
<b>3</b>	<b>Identifying surface sites during the roughening of Pt(111)</b>	<b>29</b>
3.1	Electrochemical measurements . . . . .	31
3.2	EC-STM site densities . . . . .	34
3.3	Correlating site densities to reactivity . . . . .	38
3.4	Conclusions . . . . .	45
<b>4</b>	<b>Voltammetric SECCM: dynamic imaging of hydrazine oxidation</b>	<b>49</b>
4.1	Voltammetric SECCM . . . . .	51
4.2	Hydrazine oxidation at Pt electrodes . . . . .	54
4.3	Voltammetric SECCM imaging . . . . .	56
4.4	Hydrazine oxidation in air . . . . .	62
4.5	Conclusions . . . . .	65
<b>5</b>	<b>The reactivity of platinum microelectrodes</b>	<b>69</b>
5.1	Electrode characterization . . . . .	71
5.2	Catalytic reactivity . . . . .	74
5.3	UME vs. macroelectrode . . . . .	79
5.4	Conclusions . . . . .	81
<b>A</b>	<b>EC-STM methods and general data processing</b>	<b>85</b>
A.1	Methods . . . . .	85
A.2	EC-STM images . . . . .	87
A.3	Cyclic voltammetry . . . . .	87

<b>B</b>	<b>Roughening analysis of Pt(111)</b>	<b>91</b>
B.1	Vacancy evolution . . . . .	91
B.2	Scaling analysis . . . . .	91
B.3	Correlation coefficient . . . . .	95
<b>C</b>	<b>Surface site identification of roughened Pt(111)</b>	<b>97</b>
C.1	Average nanoisland . . . . .	97
C.2	Structural fits . . . . .	99
C.3	Site densities . . . . .	100
C.4	CV fits . . . . .	108
<b>D</b>	<b>Platinum nanoisland structures</b>	<b>109</b>
<b>E</b>	<b>Details on SECCM experiments</b>	<b>111</b>
E.1	Methods . . . . .	111
E.2	Cyclic voltammetry . . . . .	112
E.3	Droplet residues . . . . .	112
E.4	Quantitative multimicroscopy . . . . .	114
<b>F</b>	<b>UME methods</b>	<b>117</b>
	<b>Summary and Outlook</b>	<b>121</b>
	<b>Samenvatting</b>	<b>127</b>
	<b>List of publications</b>	<b>132</b>
	<b>Curriculum vitae</b>	<b>134</b>



# 1 | Introduction

During a chemical reaction, reactant molecules need to encounter each other at exactly the right place, at the right time, and with the right orientation. As a result, many bulk reactions occur only at extremely low rates. Adding energy to the system, typically in the form of heat or pressure, leads to increased reaction rates. However, most of this energy is used to overcome the so-called reaction barrier (see Fig. 1.1), and is therefore not used efficiently. Catalysts provide a much more effective pathway to store and release chemical energy.<sup>1</sup> A perfect catalyst binds reactant molecules in a way that is optimal for the reaction of interest to occur, such that the reaction barrier is as low as possible. This does not only increase the rate of product formation (the activity), but by choosing the right catalyst and operating conditions, one can also influence which product is formed (the selectivity). Catalysts are generally considered to be regenerated at the end of the catalytic cycle, or even to remain unaltered during the reaction. In this way, a single catalyst could be used indefinitely without ever being consumed.

Catalysts play a prominent role in the production processes of approximately 90% of all our chemicals and materials.<sup>2</sup> As such, they have a huge impact on our society, although most people are unaware of this. Most large-scale industrial processes make use of heterogeneous catalysis, in which the catalyst is in a different phase (typically solid) than the reactants (gas or liquid). Unfortunately, it turns out that most catalysts do not exhibit the ideal textbook behavior. Although reaction barriers are decreased (see Fig. 1.1) and a single catalyst remains active for many catalytic cycles, the input of additional energy and ‘fresh’ catalyst material are still required. The implications of these phenomena at the industrial scale can not be overestimated. For example, the synthesis of ammonia (the key step in the production of artificial fertilizers) consumes more than 1% of the global energy supply.<sup>3</sup> The production of gasoline from otherwise unusable fractions of crude oil (using fluid catalytic cracking) consumes approximately 2300 tons of catalyst per day.<sup>4</sup> With this in mind, it comes at no surprise that many research efforts in catalysis focus on the development of catalysts that exhibit both increased reactivity and stability.

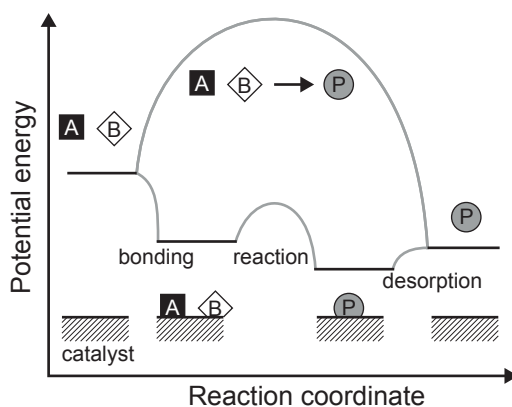


**Fig. 1.1 | Potential energy diagram:** Schematic overview of the energy needed for a chemical reaction to occur with and without a catalyst present. Figure adapted from Ref. [5].

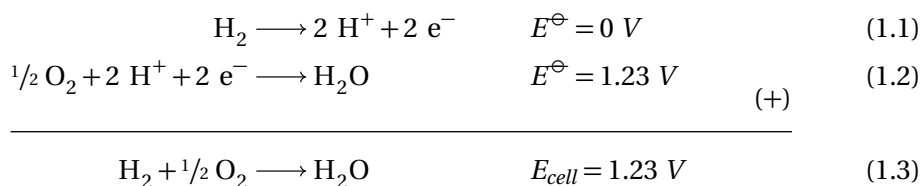
The source of the input energy provides another important reason to study catalysis. Since the industrial revolution, energy is largely generated by the combustion of fossil fuels. However, the supply of fossil fuels is limited and often dependent on politically unstable regions. Furthermore, the emission of  $\text{CO}_2$  into the atmosphere is the main contributor to anthropogenic global warming.<sup>6</sup> In recent years, more and more people have realized that fossil fuels are not suitable as energy source for a modern society and that we need to switch to more sustainable alternatives. The main energy source of the future will be the sun; directly via solar panels, and/or indirectly for example using wind turbines. This implies that energy supply will be in the form of electricity, which makes one wonder about possibilities to use this electricity in a direct way to drive chemical reactions. The reverse process of converting chemical energy into electricity is of interest to make electricity available when and where it is required. Electrochemistry is the field that considers these challenges.

## 1.1 Electrochemistry

Large scale industrial applications of electrochemistry are found in the production of chlorine gas (chloralkali process), the production of aluminum (Hall-Héroult process), and electroplating.<sup>7,8</sup> Closer to home, electrochemistry is applied in batteries when portability is important and the energy consumption is relatively low and short. Interestingly, the very first electric 'cars' were already constructed

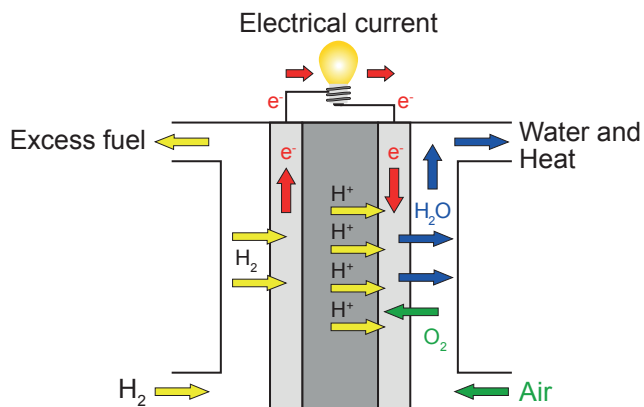
in the first half of the 19<sup>th</sup> century, although they were soon outcompeted by combustion engines.<sup>9</sup> With the improvement of technology during the last centuries, the application of electrochemistry for mobility has gained renewed interest. A promising approach, besides using stored charge from a battery, is to convert external fuels into electricity using a fuel cell. The most obvious fuel for such a device would be hydrogen,<sup>10</sup> but also other chemicals with a high energy-density, like methanol<sup>11</sup> and hydrazine,<sup>12</sup> are used in some applications.

Figure 1.2 shows a schematic overview of a hydrogen fuel cell. At one of the electrodes, the hydrogen gas is oxidized to form protons and electrons (Reaction 1.1). The protons diffuse through the electrolyte to the other electrode, whereas the electrons will move through the external electric circuit. At the other electrode, the protons and electrons are consumed to reduce molecular oxygen, forming water (Reaction 1.2). Thus, the overall reaction becomes:



which should deliver a potential of 1.23 V. If a potential above 1.23 V is applied between the electrodes, as is done in an electrolyzer, the reaction is reversed. One of the most suitable catalyst materials for both reactions is platinum.<sup>13</sup> However, even with a platinum catalyst, significant amounts of energy are lost during the reduction/formation of oxygen. Moreover, the electrodes used in this reaction tend to degrade over time. Fundamental studies providing insight in these processes are necessary to boost the application of this sustainable energy technology.

To study electrocatalysts, the overall electrochemical process (Reaction 1.3) is separated into the reactions occurring at the two different electrodes, so-called half-reactions (Reactions 1.1 and 1.2). The electrode that is studied is the working electrode and its potential is controlled with respect to a reference electrode by a potentiostat. A counter electrode delivers the current necessary to close the electronic circuit. The most common electrochemical experiment is to scan the potential of the working electrode and record the resulting current; a (cyclic) voltammogram. By combining results from different experiments, the electrochemical current can be related to the (half-)reactions occurring at the working electrode.



**Fig. 1.2 | Hydrogen fuel cell:** Schematic overview of a fuel cell that converts  $\text{H}_2$  and  $\text{O}_2$  into electricity and water. Figure adapted from Ref. [5].

## 1.2 Model catalysts

Heterogeneous catalysts are only active where they come into contact with reactants, i.e. the surface. To use the (often expensive) catalyst material in an optimal way, one should therefore maximize the surface to volume ratio. Thus, a typical application will contain large number of electrocatalytically active nanoparticles, deposited on a porous, conducting support. Zooming in on a typical nanoparticle (see Fig. 1.3A), it becomes clear that its surface is composed of a wide variety of atomic arrangements. One can distinguish different kinds of facets that are connected via edge and corner sites. It turns out that not only the material, but also these specific arrangements have a large influence on the catalytic activity.<sup>14</sup>

To study the relationship between the atomic surface structure and the electrochemical reactivity, it is most convenient to make use of well-defined (single crystalline) model samples containing only a few different surface geometries. Combining the data from different samples ultimately delivers the reactivity of single surface sites. Figure 1.3 provides several examples of different surface structures. These surfaces can be classified according to the orientation of the surface plane with respect to the smallest repetitive unit (unit cell) of the bulk material. This orientation is referred to as a Miller index. Figure 1.3B shows the three most densely packed facet geometries: the  $(111)^*$  surface with a hexagonal unit cell; the

\* In the Miller index notation,  $()$  indicate specific surface planes and  $\{\}$  indicate families of equivalent surface planes.

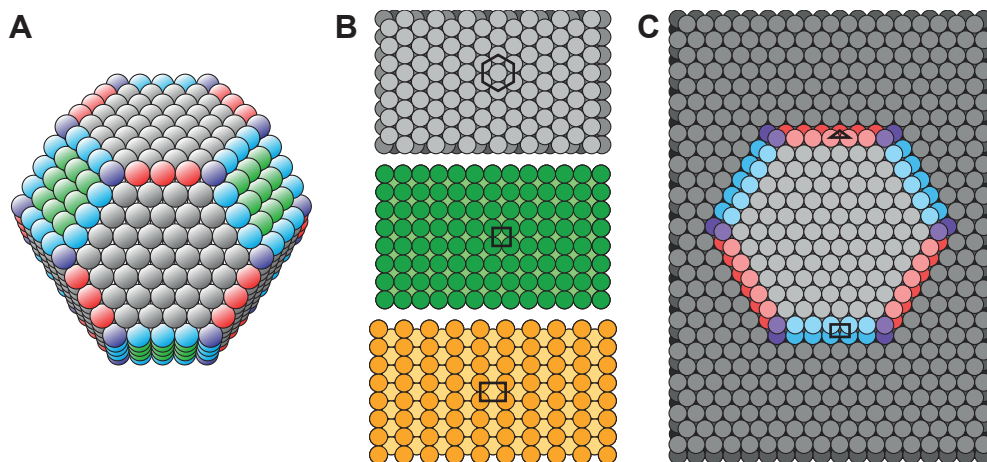


**Fig. 1.3 | Atomic scale surface structures:** (A) A model nanoparticle containing different facet-, edge-, and corner-sites. Figure by Richard van Lent. (B) The three most densely packed surface structures, from top to bottom: (111), (100), and (110). (C) Adatom island on an (111) surface containing {100} (blue) and {111} (red) type step edges separated by corner sites.

(100) surface with a square unit cell; and the (110) surface with a rectangular unit cell. Figure 1.3C shows an example of an adatom island on a (111) terrace, leading to the formation of step edges. These edges themselves also exhibit different geometries, as shown here for the {100} (blue) and {111} (red) step edges.

Although single crystal experiments provide detailed information on structure-activity relationships, it is difficult to apply this information directly in a real application. An approach to bridge this gap is by studying only small parts of a heterogeneous (polycrystalline) sample at a time. Experimental techniques to perform such experiments are discussed in the next section.

Since it was discovered that (single crystalline) platinum electrodes can relatively easily be prepared by flame-annealing, the knowledge of their fundamental electrochemical properties has drastically improved.<sup>15</sup> However, there are still open questions considering electrode degradation processes and structure-activity relationships. To answer these questions, one cannot rely on electrochemical experiments alone. Information on the electrode surface structure, preferably within the electrochemical cell (*in situ*) or even during the reaction (*operando*), is of crucial importance. Various experimental techniques have been developed to reach this goal, each with their own specific advantages and drawbacks. The

techniques used in this thesis are part of the ‘electrochemical scanning probe microscopy’ techniques (EC-SPM). They make use of a physical probe that is scanned across the electrode to visualize its structure and/or activity at the nano- to micrometer length scale.

### 1.3 Electrochemical scanning probe microscopy

The fast development of scanning probe techniques since the 1980s opened up complete new research fields to directly study interfacial processes.<sup>16,17</sup> Although many different approaches are available, there are three techniques that are of special interest within the scope of this thesis. These techniques are electrochemical scanning tunneling microscopy (EC-STM), scanning electrochemical microscopy (SECM), and scanning electrochemical cell microscopy (SECCM). An overview of these techniques is provided here, but the interested reader is referred to various textbooks and reviews that are available in the literature.<sup>18-21</sup>

In STM, a sharp metallic tip is brought at a close distance (a few Å) to a conductive sample. When a bias voltage is applied, electrons will tunnel through the gap in between the tip and sample electrodes. As the tunneling probability depends exponentially on the tip-to-sample distance, STM exhibits a height resolution down to 0.01 nm. Scanning the tip across the surface while maintaining a constant tunneling current or constant tip height, generates an image of the local surface structure.\* The maximum lateral resolution is slightly lower than the height resolution, but still on the subatomic scale, routinely leading to atomically resolved images.

The working principle of an STM can also be applied under electrochemical conditions, although this leads to some experimental complications. However, the added value of directly visualizing electrode structures under (reactive) electrochemical conditions makes it worthwhile to meet these challenges. Most importantly, one has to realize that the sample and tip currents no longer just depend on the tip-to-sample distance and the bias voltage, but also on the electrochemical conditions. Reactions occurring at either of these electrodes lead to additional electrochemical (faradaic) currents, which interfere with the imaging experiment. To minimize the faradaic contribution to the tunneling current, the tip electrode

---

\* The image represents the ‘local density of electronic states’, which for a homogeneous sample can be considered equivalent to the surface structure.

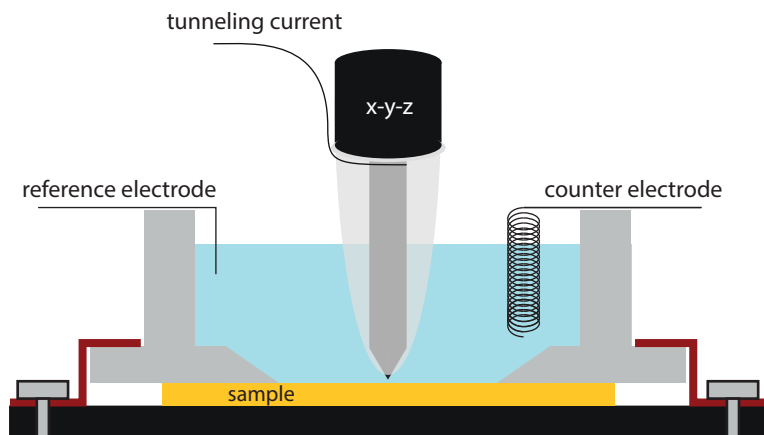


**Fig. 1.4 | EC-STM cell:** Schematic overview of the EC-STM cell. The sample and cell are clamped down onto a baseplate. The electrochemical current is recorded via the sample, the tunneling current via the tip. All potentials are controlled using a bipotentiostat.

is coated with a non-conductive material leaving only the very apex exposed. The stability of the tip material should also be considered. Tungsten is widely used to prepare STM tips for vacuum experiments because of its mechanical properties and because it is easily etched into sharp tips. In EC-STM, a PtIr alloy is commonly applied. Finally, one should realize that in EC-STM the potentials of the tip and the sample have to be controlled individually (using a bipotentiostat), whereas otherwise only the bias voltage has to be controlled. A schematic overview of the EC-STM cell is shown in Fig. 1.4.

Scanning electrochemical microscopy (SECM), like EC-STM, also makes use of a small metallic tip that is scanned across the sample surface. A typical tip consists of a disk electrode with a radius of a few micrometers down to a few nanometers (ultramicroelectrode, UME). This tip is scanned across the sample at a distance that is similar to its radius. The tip signal originates from an electrochemical current that occurs at the UME surface. As a result, the spatial resolution is on the order of the dimensions of the used tip. The highest resolution reported so far is about 1 nm, although these results are expected to be affected by a tunneling current.<sup>22,23</sup> The current-distance relationship depends on the nature of the sample and the SECM operating mode. The most common mode is the feedback mode, where products formed at the sample react at the UME, leading to an increased UME current for decreasing distance. SECM is a flexible technique to image micrometer-

resolved electrochemical activity and is applied in a wide range of research areas from catalyst screening to imaging of living cells.

A disadvantage of standard SECM modes is that the electrochemical signal is convoluted with the topographical information. In the feedback mode, for example, it is not directly clear if an increase in the UME current results from a catalytically more active part of the sample or from a decreased tip-to-sample distance. One way to circumvent this problem is by using scanning electrochemical cell microscopy, schematically illustrated in Fig. 1.5.

In SECCM, the probe is not a metallic electrode, but a double-barrel quartz capillary filled with electrolyte. At the apex of the capillary, an electrolyte droplet is formed which defines the electrochemical cell. Only those parts of the sample that are in contact with this droplet will contribute to the overall faradaic signal, as the rest of the sample remains exposed to a gas atmosphere. In this way, the local electrochemical activity (via the sample) can be measured simultaneously with the electrode topography (via additional electrodes in both barrels of the capillary). As in SECM, the spatial resolution is mainly determined by the dimensions of the used probe and chosen according to the studied sample. These probes can be reproducibly fabricated with diameters ranging from a few micrometers to tens of nanometers. In addition, SECCM is easily combined with other techniques to characterize the sample in more detail.

## 1.4 Outline of this thesis

The main goal of this thesis is to study fundamental platinum electrochemistry, making use of EC-SPM techniques. Chapters 2 and 3 use EC-STM to study the degradation of a Pt(111) electrode upon the application of oxidation-reduction cycles. In this process we observe the formation of Pt nanoislands all over the atomically flat surface. Chapter 2 describes the evolution of the overall roughness of the electrode and correlates this to its total electrochemical signal. From this analysis we identify two different growth regimes: a 'nucleation & early growth' regime of nanoisland formation, and a 'late growth' regime after island coalescence. In Chapter 3, the EC-STM data are analyzed in more detail to correlate the evolution of individual surface site densities to the complex evolution of the voltammetric signal. Here, we disentangle the electrochemical signal of individual step-, facet-, and vacancy-sites.

Chapter 4 describes a new mode of SECCM, in which a full electrochemical measurement can be made at each position of the surface. This voltammetric

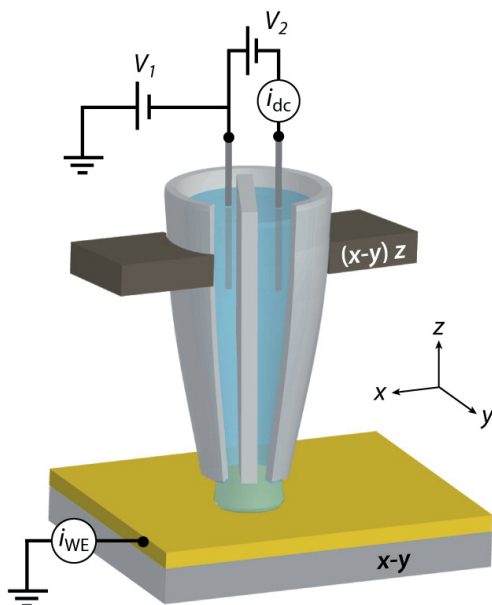


**Fig. 1.5 | SECCM setup:** Schematic overview of the SECCM technique. The electrochemical cell is defined by the droplet at the apex of the capillary. The faradaic current is measured at the sample. The current between the two electrodes in the capillary provides the topographical information. The potential of the working electrode is controlled by the offset ( $V_1$ ) and bias ( $V_2$ ) voltages, applied via the capillary using a bipotentiostat. Figure reproduced from Ref. [21]

SECCM mode is used to study the oxidation of hydrazine at a polycrystalline platinum electrode. We demonstrate that voltammetric SECCM is able to visualize differences in activity that are related to the (average) local surface structure. Additionally, it is shown that the reactivity is dramatically decreased in the presence of oxygen, which is ascribed to the presence of a nonfaradaic hydrazine oxidation pathway.

Chapter 5 describes the electrochemical reactivity of platinum ultramicroelectrodes. UMEs are not only used as SECCM tips, but also in many other catalytic studies to overcome limitations due to reactant diffusion or electrolyte resistance. However, they cannot be cleaned by flame-annealing and many studies using UMEs do not provide any information on the cleanliness of the UME surface. By comparing the reactivity of UMEs to that of flame-annealed electrodes, it is shown that UMEs exhibit a decreased reactivity towards surface sensitive reactions. The limited possibilities to clean UMEs are argued to cause these observations.

## References

1. Niemantsverdriet, J. *Spectroscopy in Catalysis: An Introduction* (Wiley, 2008).
2. Bowker, M. *The basis and applications of heterogeneous catalysis* (Oxford University Press, Incorporated, 1998).
3. International Fertilizer Association. *Energy Efficiency and CO<sub>2</sub> Emissions in Ammonia Production* tech. rep. (2009), 4.
4. Vogt, E. T. C. & Weckhuysen, B. M. Fluid catalytic cracking: recent developments on the grand old lady of zeolite catalysis. *Chem. Soc. Rev.* **44**, 7342–7370 (20 2015).
5. Den Dunnen, A. *Surface-structure dependencies in catalytic reactions* PhD thesis (Leiden University, 2015), 2.
6. Davis, S. J., Caldeira, K. & Matthews, H. D. Future CO<sub>2</sub> Emissions and Climate Change from Existing Energy Infrastructure. *Science* **329**, 1330–1333 (2010).
7. Botte, G. G. Electrochemical Manufacturing in the Chemical Industry. *Electrochem. Soc. Interface* **23**, 49–55 (3 2014).
8. Schlesinger, M. & Paunovic, M. *Modern Electroplating* (Wiley, 2011).
9. Guarnieri, M. *Looking back to electric cars* in *History of Electrotechnology Conference* (IEEE, 2012), 1–6.
10. Hydrogen on the rise. *Nature Energy* **1**, 16127 (2016).
11. Hamnett, A. in *Handbook of Fuel Cells* (John Wiley & Sons, Ltd, Chichester, UK, 2010).
12. Kohnke, H. in *Handbook of Fuel Cells* (John Wiley & Sons, Ltd, Chichester, UK, 2010).
13. Holton, O. T. & Stevenson, J. W. The Role of Platinum in Proton Exchange Membrane Fuel Cells. *Platinum Metals Rev* **57**, 259–271 (2013).
14. Koper, M. T. M. Structure sensitivity and nanoscale effects in electrocatalysis. *Nanoscale* **3**, 2054–2073 (2011).
15. Climent, V. & Feliu, J. M. Thirty years of platinum single crystal electrochemistry. *J. Solid State Electrochem.* **15**, 1297–1315 (2011).
16. Binnig, G., Rohrer, H., Gerber, C. & Weibel, E. Surface Studies by Scanning Tunneling Microscopy. *Phys. Rev. Lett.* **49**, 57–61 (1 1982).
17. Bard, A. J., Fan, F. R. F., Kwak, J. & Lev, O. Scanning Electrochemical Microscopy. Introduction and Principles. *Anal. Chem.* **61**, 132–138 (1989).
18. Smith, T. & Stevenson, K. in *Scanning Probe Microscopy* (eds Kalinin, S. & Gruverman, A.) 280–314 (Springer New York, 2007).
19. Amemiya, S., Bard, A. J., Fan, F.-R. F., Mirkin, M. V. & Unwin, P. R. Scanning Electrochemical Microscopy. *Annu. Rev. Anal. Chem.* **1**, 95–131 (2008).
20. Bard, A. & Mirkin, M. *Scanning Electrochemical Microscopy* 2nd ed. (CRC Press, 2012).
21. Ebejer, N. *et al.* Scanning Electrochemical Cell Microscopy: A Versatile Technique for Nanoscale Electrochemistry and Functional Imaging. *Annu. Rev. Anal. Chem.* **6**, 329–351 (2013).
22. Blanchard, P. Y. *et al.* Scanning Electrochemical Microscopy Study of Permeability of a Thiolated Aryl Multilayer and Imaging of Single Nanocubes Anchored to It. *Langmuir* **32**, 2500–2508 (2016).
23. Kai, T., Zoski, C. G. & Bard, A. J. Scanning electrochemical microscopy at the nanometer level. *Chemical Communications* **54**, 1934–1947 (2018).

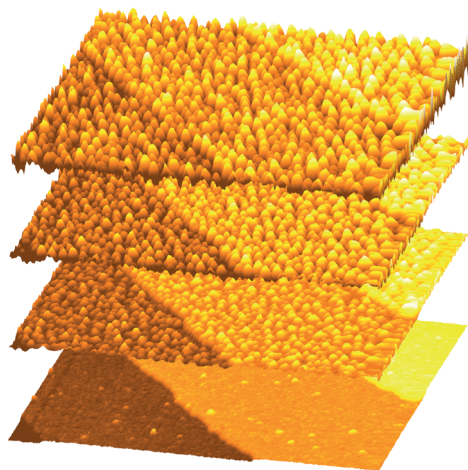
## 2

# Correlation of surface site formation to nanoisland growth in the electrochemical roughening of Pt(111)

---

*Platinum plays a central role in a variety of electrochemical devices. Its practical applications depend on the prevention of electrode degradation. This is particularly important under conditions of repeated oxidation and reduction, which induce irreversible surface structure changes. However, the underlying atomic processes are far from understood. Here, we examine the correlation between the evolution of the electrochemical signal of Pt(111) and its surface roughening by simultaneously performing cyclic voltammetry and in situ electrochemical scanning tunneling microscopy (EC-STM). We identify: a ‘nucleation & early growth’ regime of nanoisland formation, and a ‘late growth’ regime after island coalescence, which continues up to at least 170 cycles. The correlation analysis shows that each step site that is created in the ‘late growth’ regime contributes equally strong to both the electrochemical and the roughness evolution. In contrast, steps created in the ‘nucleation & early growth’ regime contribute to the roughness, but not to the electrochemical signal.*

---



---

This chapter is based on Jacobse, L., Huang, Y.-F., Koper, M.T.M. & Rost, M.J. *Nat. Mater.* **17**, 277–282 (2018).

Early attempts to resolve the structure of the roughened Pt(111) surface were made by *ex situ* low energy electron diffraction (LEED)<sup>1,2</sup>, *in situ* x-ray reflectivity<sup>3-5</sup>, and *in situ* EC-STM<sup>6-10</sup> experiments. From these studies it was concluded that the roughened surface is covered with nanoscale islands of (at most) a few atoms high. Indications were found that the resulting surface structure depends on the number of oxidation-reduction cycles (ORCs), the upper potential limit (or transferred charge), and the potential scan rate. However, it has as yet been impossible to fully resolve the island evolution. Importantly, the corresponding electrochemical data for all spatially-resolved studies is either absent or incomplete.

Based on electrochemical experiments, insights in the average surface evolution were obtained during the first 20 ORCs.<sup>11-15</sup> Initially both {100} and {111} steps\* form on the roughened surface, while eventually only {111} steps remain. Advanced *in situ* EC-STM<sup>16,17</sup> and x-ray reflectivity<sup>18-22</sup> experiments are ideal tools to study this system at the atomic level. Using x-ray scattering experiments and following the surface evolution for 20 ORCs, Ruge *et al.* observed an increasing island size with increasing cycle number and decreasing upper potential limit.<sup>21</sup> However, there is no single publication that provides both the detailed structural information and the complete electrochemical characterization from the very same experiment. This is a prerequisite for a true correlation, a deeper understanding of the roughening process, and the interpretation of the voltammetric signals.

The experiments presented here and in Chapter 3 are measured using a home-built EC-STM described previously.<sup>23-25</sup> In these experiments, STM images and cyclic voltammograms (CVs) were recorded alternately for 170 ORCs. The presented data originate from one single experiment, which was reproduced four times to ensure its representative character (for details see Appendix A). We first discuss the observed electrochemical signals that have been measured *in situ* during the EC-STM experiment and will then turn to the STM results and their analysis.

---

\* More precisely, these step sites should be denoted as  $\langle 110 \rangle / \{100\}$  and  $\langle 110 \rangle / \{111\}$  respectively, i.e. steps along a direction equivalent (according to the symmetry) to [110] and exhibiting a square {100} or hexagonal {111} geometry.

## 2.1 Electrochemical measurements

Figure 2.1 shows, from black to white, the CVs of the Pt(111) electrode of 170 ORCs between 0.06 and 1.35 V. From the evolution of the CVs, one notices the appearance and disappearance of ‘peaks’ and ‘shoulders’ upon increasing cycle number. The changes in the hydrogen adsorption/desorption region ( $< 0.4$  V) can be related to the presence and appearance of specific step or defect-like surface structures.<sup>11,12,14,26–31</sup> With increasing potential, first OH is adsorbed on the terrace (0.8 V), followed by the formation of a 2D oxide (1.05 V) and a 3D oxide ( $> 1.1$  V).<sup>15,32,33</sup> Not all atoms reach their original positions upon reduction of the 3D oxide, leading to surface roughening. Simultaneously, a small amount of  $\text{Pt}^{2+}$  dissolves in the electrolyte, a part of which will be reduced on the surface once the potential is decreased.<sup>34,35</sup> The identification of specific surface sites is typically performed in the hydrogen region. Initially, this region consists only of a single broad band, associated with hydrogen adsorbed on Pt(111) terrace sites. The charge related to this process, indicated by the dark blue area in Fig. 2.1, is  $168 \mu\text{C}\cdot\text{cm}^{-2}$ . The agreement of this value with the literature<sup>36</sup> and the absence of any other peaks confirm the cleanliness and efficacy of our setup, sample treatment, and preparation.

Starting from this well-defined situation, two new peaks ( $A_1$  and  $A_2$ ) appear when the sample is subjected to the first ORCs. The  $A_1$  peak is attributed to {100} step sites and starts decreasing again already after three cycles. In contrast, the  $A_2$  peak that is attributed to {111} step sites, stabilizes after approximately 20 cycles. These observations agree well with reported data.<sup>14</sup> Interestingly, we find a third, not earlier reported, peak ( $A_3$ ) that develops slowly with increasing cycle number starting around the 30<sup>th</sup> cycle. Based on other single crystal experiments, it might be related to the formation of {100} terrace sites.<sup>37,38</sup>

The total charge related to hydrogen desorption ( $q_H$ ) can be obtained by integrating the anodic, double-layer corrected current between 0.06 and 0.4 V (see Appendix A). As  $q_H$  is directly related to the number of surface sites, it should be possible to convert it into a measure for the surface roughness. However, for converting a terrace site into the various undercoordinated (step) sites one has to take into account different stoichiometric coefficients.<sup>26–29</sup> For fewer than 20 ORCs, there is no linear relationship between the charge corresponding to  $A_1$  and  $A_2$  peaks, leading to  $q_H$  being a complex function of the created as well as annihilated adsorption sites. Further complications arise as the stoichiometric

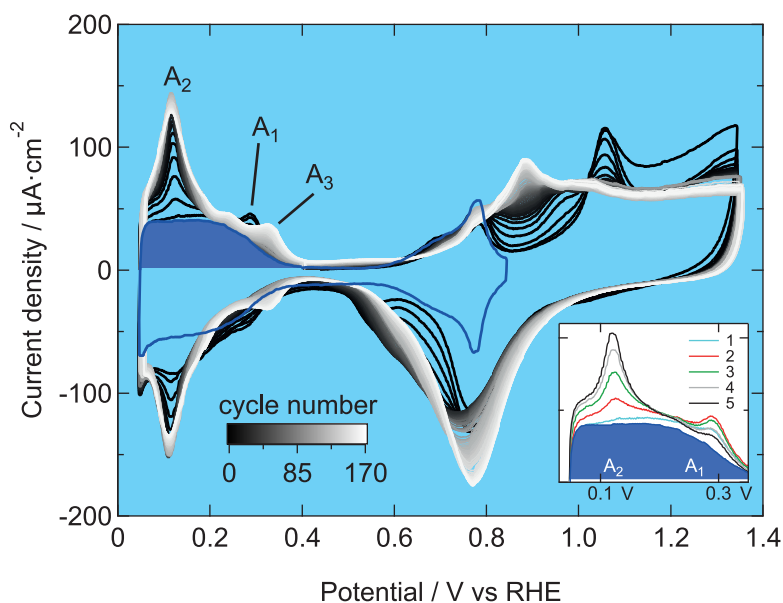


**Fig. 2.1 | Cyclic voltammograms of consecutive oxidation-reduction cycles:** The CV of the pristine Pt(111) surface is shown in blue and the blue shaded area indicates the initial charge related to hydrogen desorption. The scan rate is  $50 \text{ mV}\cdot\text{s}^{-1}$ . The inset shows the evolution of the  $A_1$  and  $A_2$  peaks during the first five cycles.

coefficients in the kinetic model describing the roughening process<sup>11,12</sup> differ from the ones determined for the ideally stepped single crystal surfaces. This suggests that the formed adsorption sites should not be considered as regular step edges, although they might be so geometrically, as finite size effects are known to change the local potential energy landscape of the sites.<sup>39-41</sup> In the following, we will use  $q_H$  to describe the electrochemically observed roughening, which we compare to the roughness derived from the EC-STM data.

## 2.2 *in situ* EC-STM

Although our STM is capable of measuring under *operando* conditions (e.g. during a CV), our aim was to record high-quality snapshots, in which the complete imaged surface has transformed in the same way. Therefore, all images are acquired in the double layer region at constant tip and sample potential ( $U_t=0.45 \text{ V}$  and  $U_s=0.4 \text{ V}$ , respectively). The full set of STM images is provided as movie in Ref. [42] and Fig. 2.2 shows four selected images illustrating the key situations in the roughening

evolution. We first describe the surface changes qualitatively, before turning to a quantitative analysis.

Panel (A) shows the starting situation with large (111) terraces confirming the well-prepared and clean surface. The few islands on the terraces are remainders of our flame-annealing procedure to approximately 1250 K. During cooling down, the thermally activated equilibrium adatom density has to decrease and all adatoms that can not reach a step edge within their diffusion length, will nucleate as small islands.<sup>\*,45,46</sup>

During the first ~25 ORCs small, monoatomic-high adatom islands nucleate on the surface and existing islands undergo a lateral and slight height growth. This is illustrated in the STM image after 8 cycles (Fig. 2.2B). We refer to this phase as the ‘nucleation & early growth’ regime of the roughening process. Simultaneous with the formation of adatom islands, vacancy islands should be created to balance the total mass. However, small vacancy islands are extremely hard to resolve using an STM, due to their convolution with the tip shape. This is probably the reason that the early EC-STM studies only reported the formation of adatom islands,<sup>6–8</sup> whereas ‘holes’<sup>16</sup> and ‘pits’<sup>17</sup> were observed only more recently. We have clear evidence for the formation of vacancy islands. Firstly we do observe small areas that are lower than the original pristine terrace, see the darker spots between the islands in Fig. 2.2B. As not all of them show a depth of exactly one step height (some half a step height), one might argue that these are oxide-like remainders from the oxidation-reduction process. However, this is unlikely, since our holes do not change at a constant reducing sample potential in between the ORCs (see Appendix B). Furthermore, the vacancy islands depth increases with increasing cycle number, which is interpreted as lateral growth, thereby reducing the effect of the tip convolution. Finally, the height line after cycle 170 in Fig. 2.3 clearly shows that the original terrace is etched more than 2 monolayers deep.

With further ORCs, the nucleation of new islands stops and any further changes are related to the growth of existing islands both in lateral size and height. The original, unaffected terrace area decreases until the islands eventually coalesce as shown in panel (C) after 31 cycles. Tip convolution prevents the determination of the exact moment of coalescence between the 20<sup>th</sup> and 30<sup>th</sup> cycle. Depending on

---

\* This is confirmed by the denuded zone in front of the lower step edge, the missing denuded zone at the upper step edge (Ehrlich-Schwoebel barrier<sup>43,44</sup>), the distances between the islands, their size, and the fact that these islands show the standard Pt(111) step-height.

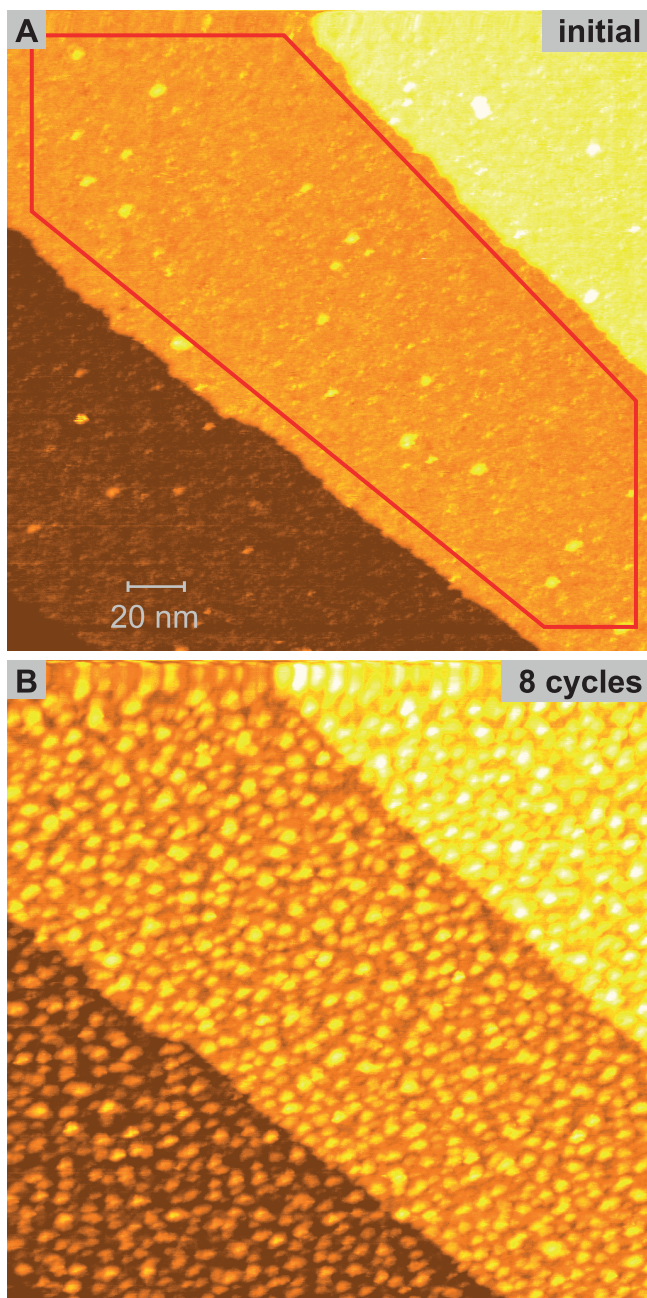
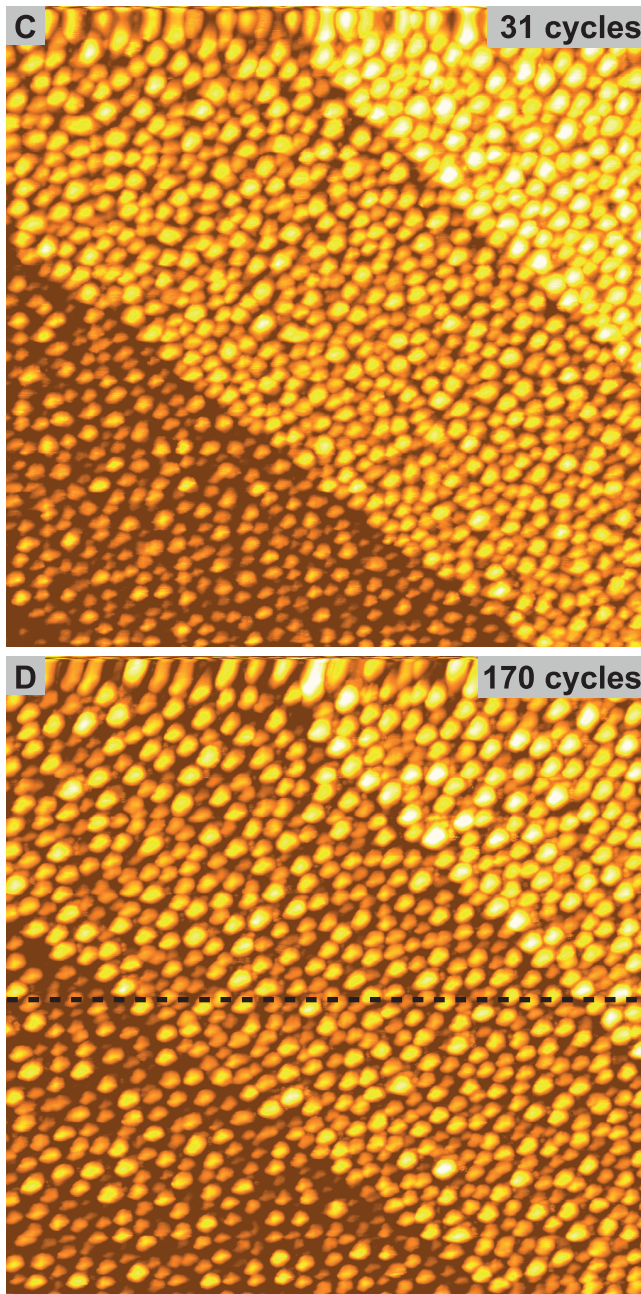


**Fig. 2.2 | STM images after oxidation-reduction cycles: (A)** the pristine Pt(111) surface after cleaning. A few Pt adatom islands are visible that remain from the flame annealing. The solid red line shows the typical area that we used for our analysis. **(B)** After 8 cycles, several islands, predominantly of monoatomic height, have nucleated. In between the islands, one sees the original terrace and even some vacancy islands.



(C) After 31 cycles, the islands have grown in size such that they touch each other and cover the complete terrace. (D) After 170 cycles, the islands have continued growing, primarily in height, as is clarified in Fig. 2.3, which compares the height profiles of the surface at the position indicated by the dashed black line. All images ( $230 \times 230 \text{ nm}^2$ ) were recorded on the same part of the surface with  $U_t = 0.45 \text{ V}$ ,  $U_s = 0.4 \text{ V}$ , and  $I_t < 300 \text{ pA}$ .

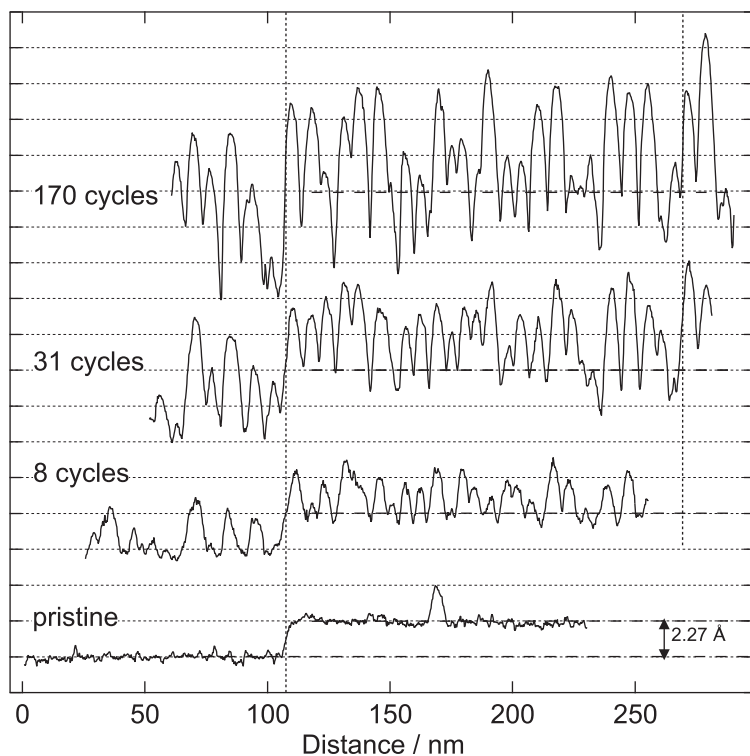


**Fig. 2.3 | Height lines extracted from the STM images in Fig. 2.2:** The lines are measured at the same position of the surface allowing a direct comparison. The original step positions are indicated with the vertical dotted lines. The well-prepared, flat terrace evolves into a roughness with islands that span 6 MLs in total. The data is vertically offset for clarity. The horizontal dashed lines indicate the original, roughened height of the upper terrace. Although the grid indicates integer step heights, one should be aware of the tip-surface convolution and, more importantly, of the low probability that a single height line captures the maximum height (depth). The fact that the original terrace is etched more than 2 MLs deep after cycle 170 proves the formation of vacancy islands.

the precise mechanism for the island nucleation and evolution, one might expect that stagnation sets in at this point and that the surface has adapted its growth equilibrium (steady-state) structure for this process.<sup>47,48</sup> However, even up to the 170<sup>th</sup> cycle (panel (D)), the surface changes significantly. We describe this as the ‘late growth’ phase. To fully acknowledge the differences, we extracted 4 height lines, plotted in Fig. 2.3, from the STM images taken at the position indicated by the dashed line in Fig. 2.2D. These height lines show that initially monoatomic-high islands nucleate on the flat terrace and that the final height variation (after 170 ORCs) spans six monolayers. From the horizontal line that indicates the original terrace, it is clear that the increasing height variation is caused both by an increased island height and an increased ‘depression’ depth, the latter of which is due to vacancy island formation.

There have been two earlier EC-STM studies on the prolonged roughening of Pt(111) by ORCs, from the groups of Itaya<sup>8</sup> and Shibata<sup>10</sup>, using a different supporting electrolyte (0.5 M H<sub>2</sub>SO<sub>4</sub> instead of 0.1 M HClO<sub>4</sub>) and a slightly higher upper potential limit (1.5 V). Itaya concluded that no further surface evolution takes place after the 10<sup>th</sup> cycle while measuring up to 100 cycles. Shibata, on the other hand, reported island growth for at least 100 cycles as determined by EC-STM. Although the surface was subjected to 1000 ORCs in the latter study, it is unclear if this led to any additional island growth. Our real-space observation following exactly the same part of the surface in the form of STM images enables a detailed roughness analysis which, combined with the evolution of the CVs, proves that the surface keeps evolving up to the 170<sup>th</sup> cycle, although the changes become less pronounced with increasing cycle number.

### 2.3 Quantitative roughness analysis

To quantify the roughness and its evolution, we calculate from our STM images so-called height-difference correlation functions (HDCFs).<sup>49</sup> We use the second-order form of the family of HDCFs, because this provides direct access to the root-mean-square (RMS) roughness value.

$$C_2(\mathbf{x}_0, \mathbf{r}) = \langle |h(\mathbf{x}_0 + \mathbf{r}) - h(\mathbf{x}_0)|^2 \rangle^{1/2} \quad (2.1)$$

Specifically, we calculate the average for all different data points of the surface and for the full range of radii

$$C_2(r) = \langle C_2(\mathbf{x}_0, \mathbf{r}) \rangle_{|\mathbf{r}|=r, |\mathbf{x}_0|} \quad (2.2)$$

For a self-affine surface,  $C_2(r)$  can be described with scaling parameters

$$C_2(r) = \xi_{\perp} \cdot f(r/\xi_{\parallel}) \quad \text{with} \quad \begin{aligned} f(x) &\sim r^H & \text{for } r \ll \xi_{\parallel} \\ f(x) &= \sqrt{2} & \text{for } r \gg \xi_{\parallel}, \end{aligned} \quad (2.3)$$

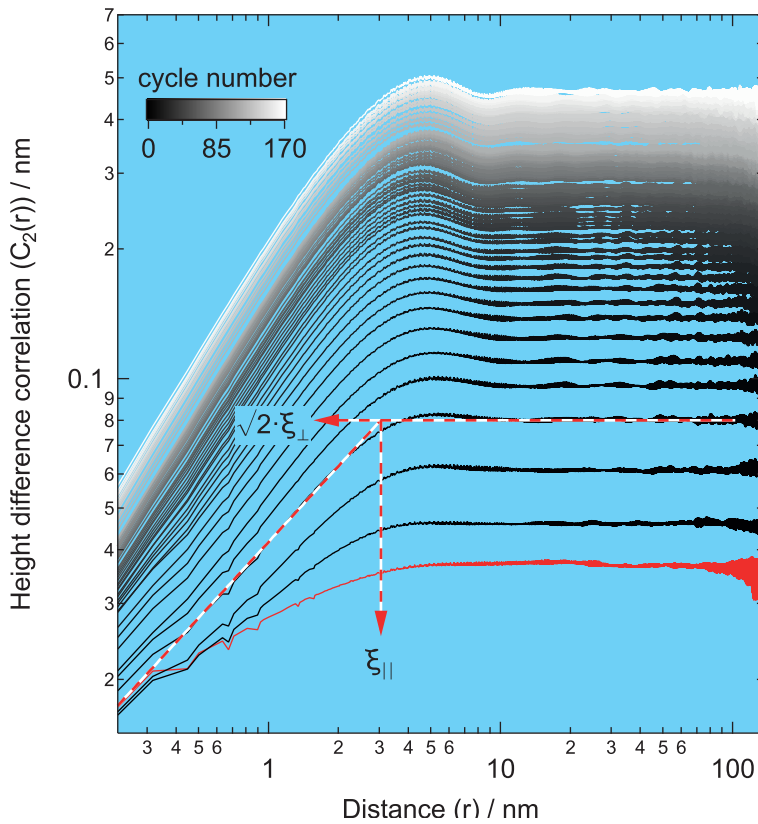
in which  $\xi_{\perp}$  is the perpendicular correlation length (surface width or RMS roughness),  $\xi_{\parallel}$  is the parallel correlation length, and  $H$  is the so-called Hurst exponent. The surface width describes the surface roughness, the parallel correlation length describes the lateral distance one needs to travel to reach the surface roughness, and the Hurst exponent describes how the roughness is locally built up.

Figure 2.4 shows  $C_2(r)$  for all our STM images from the pristine surface until after the 170<sup>th</sup> ORC (68 images in total, see Appendix A). To avoid contributions from the slope of the sample and the step edges, we analyzed only a background corrected part of a single terrace (see red area in Fig. 2.2A and Appendix A). For all images we observe a plateau value ( $\sqrt{2} \cdot \xi_{\perp}$ ) for large distances, which confirms that the chosen image size is indeed large enough to capture the full terrace roughness. At short distances,  $C_2(r)$  shows a power law dependence.  $\xi_{\parallel}$  is determined by calculating the intersection between  $\xi_{\perp}$  and a power law fit through the first 20 data points ( $r < 1.4$  nm) as illustrated by the red/white dashed lines in Fig. 2.4. Initially,  $\xi_{\parallel}$  depends on both the island size and the nucleation distance. After coalescence,  $\xi_{\parallel}$  depends only on the island size. The slight increase in the ‘late growth’ regime, indicates lateral island growth. Although  $\xi_{\parallel}$  cannot directly be translated into an absolute island size, it can be derived from the first local minimum of  $C_2(r)$ . Between 31 and 170 cycles, our average island size is  $8.9 \pm 0.1$  nm.\* This value is slightly larger than reported literature values<sup>6–10</sup>, which fits with the observed trend of increasing island size with decreasing upper potential limit.<sup>21</sup>

Equipped with both the electrochemical information on the number of hydrogen adsorption sites ( $q_H$ ) and the detailed real-space information on the roughness ( $\xi_{\perp}$ ), we quantify their dependence in Fig. 2.5A. Figure 2.5B shows that the evolution of the two curves deviates from each other until  $\sim 30^{\text{th}}$  cycle, i.e. in the ‘nucleation & early growth’ phase. As mentioned before, this is also the regime where the voltammetry exhibits a complex and not yet understood behavior. In the ‘late growth’ regime, however, there is a very good agreement between both curves.

---

\* This error is based on the variation of the position of the local minimum in the different images after radially averaging the HDCE. In the individual images, the radial variation of this minimum is about 0.9 nm.



**Fig. 2.4 | Height-difference correlation functions ( $C_2(r)$ ) as function of ORC number:**

The number of the oxidation-reduction cycles is indicated in the legend and covers from black to white all 170 cycles. The result for the pristine surface is shown in red. The red/white dashed lines illustrate the determination of the surface width ( $\xi_{\perp}$ ) and the parallel correlation length ( $\xi_{\parallel}$ ).

To quantify the correlation between  $q_H$  and  $\xi_{\perp}$ , we calculate the cumulative correlation coefficient  $r(n)$  shown in the inset of Fig. 2.5B (see Appendix A). In the ‘nucleation & early growth’ regime, the value for the correlation is rather low. At the end of the ‘nucleation & early growth’ regime,  $r(n)$  starts to increase significantly (while also becoming more accurate), eventually reaching a maximum of  $r = 0.87 \pm 0.02$  after 170 ORCs. Actually, omitting the initial ORCs, one would find a maximum correlation of  $r(31-170) = 0.96 \pm 0.01$ . Thus, the transition between the two regimes occurs between the 21<sup>st</sup> (the minimum of  $r(n)$ ) and the 31<sup>st</sup> cycle. This analysis demonstrates that there is a strong and significant linear correlation between  $q_H$  and  $\xi_{\perp}$  in the ‘late growth’ phase: it implies that the number of newly generated step edges contributing to the surface roughness is a constant fraction of the total number of newly generated hydrogen adsorption sites. The strong correlation between  $q_H$  and  $\xi_{\perp}$  is in line with the qualitative observation that the islands grow predominantly in height during the ‘late growth’ phase.

The fact that the correlation holds over a large number of ORCs is rather surprising. On the formed nanoscale islands, one expects finite size effects (due to stress relaxations and step-step interactions<sup>39–41</sup>) to change the atomic distances and the local potential energy landscape, leading to a more complicated evolution of the electrochemical signals. The derivation of an atomic model that describes the island shapes during the evolution based on the EC-STM data should lead to a deeper insight into (the evolution of) the voltammetric features.

More detailed information on the roughening mechanism can be obtained by further analyzing the time evolution of  $\xi_{\perp}$  and  $\xi_{\parallel}$ . If the underlying mechanism would remain the same during the entire experiment and the continuous process can be described by one set of differential equations, so-called *scaling* should occur and the time evolution should adhere to the following three power law dependencies:

$$\begin{aligned}\xi_{\perp} &\sim t^{\beta} \\ \xi_{\parallel} &\sim t^{1/z} \sim t^{\beta/\alpha} \\ \xi_{\perp} &\sim \xi_{\parallel}^{\alpha}\end{aligned}\tag{2.4}$$

The values of the scaling exponents  $(\alpha, \beta, z)$  allow to classify data according to specific universality classes.<sup>49</sup> The different classes describe for example the influences of diffusion via the surface or the electrolyte, mass conservation, or etching/deposition flux dependence on the surface dynamics.<sup>49</sup> Strictly speaking, scaling is applicable only to a continuous evolution in time. However, it was

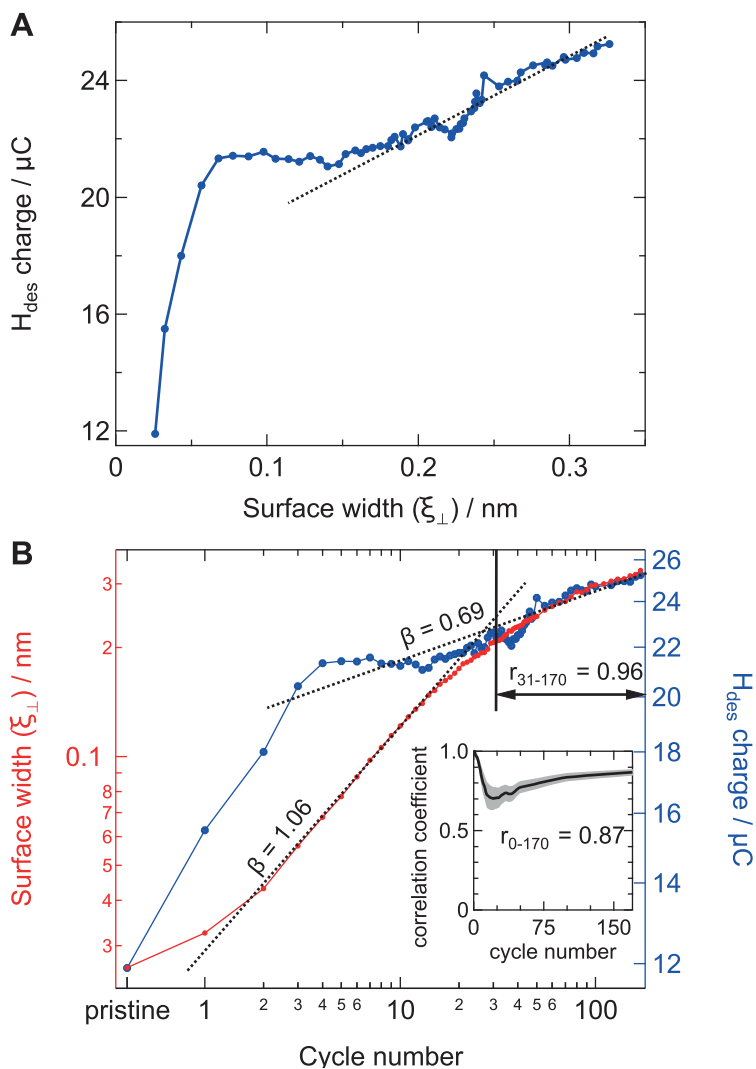


**Fig. 2.5 | Correlation between electrochemical and STM data:** (A) the hydrogen desorption charge as function of the surface width. The dotted black line, indicating the linear correlation in the ‘late growth’ regime, is drawn to guide the eye. (B) the surface width (red, from STM images) is shown together with the charge related to hydrogen desorption (blue, from cyclic voltammetry). Both data are plotted logarithmically to easily identify possible power-law regimes. The y-axes are chosen such that the data for the initial and final situation overlap. The two black dotted lines indicate the two possible scaling regimes as discussed in the main text. Details on the determination of the exponent  $\beta$  are provided in Appendix B. The inset shows the cumulative correlation coefficient quantifying the correlation between the STM and electrochemical data. The shaded area indicates its probable error.<sup>50</sup>

demonstrated that this formalism holds also for our kind of electrochemical experiments, with interrupted growth and surface evolution, as long as all surface changes occur only during the oxidation/reduction transition (negligible surface diffusion in between).<sup>3</sup>

If ideal scaling would occur, the logarithmic representation of  $\xi_{\perp}$  vs. cycle number in Fig. 2.5B should yield a single straight line. However, we observe at least two slopes, and therefore scaling does not apply over all 170 cycles. Considering the two growth regimes already identified, this is expected. As nucleation may also follow scaling laws<sup>51</sup>, the roughness in Fig. 2.5 might be described by two sets of exponents for the different regimes, indicated by the two black dotted lines.

Previously, You and Nagy concluded from x-ray reflectivity experiments on the same system that scaling *does* occur during the first 9 ORCs.<sup>3</sup> Slight differences in the roughening process might occur as they kept the surface at 1.25 V for 15 minutes, whereas we scan the sample potential to 1.35 V. However, You and Nagy discussed only the first of the three power laws in Eq. 2.4, which cannot indisputably prove scaling. In our case, the nonlinear behavior of  $\xi_{\parallel}$  with a pronounced maximum during the first 9 ORCs (see Appendix B), leads to the conclusion that scaling does not occur in this regime.

The ‘late growth’ regime can be described by the power laws in Eq. 2.4, but this analysis does not lead to consistent values for the exponents, which would be necessary to definitely prove scaling (see Appendix B). This is a well-known issue, as the ‘ideal’ values for the scaling exponents are approached asymptotically when the growth mechanism changes from one process to another.<sup>49</sup> Therefore, we can also not say that scaling does not occur in the ‘late growth’ regime. An even larger number of ORCs would be necessary to provide more insight.

If scaling does not occur and the growth is conserved, the surface profile might end in a steady-state situation in the ‘late growth’ regime.<sup>47,48</sup> However, a small fraction of a monolayer of platinum dissolves during each ORC.<sup>34,35</sup> Moreover, the amount of Pt that dissolves during each ORC, increases with increasing cycle number for at least 100 ORCs.<sup>52</sup> Although it would be possible to reach a steady-state surface structure while losing material into the electrolyte during each cycle<sup>47,48</sup>, the fact that the dissolved amount changes with each cycle means that the surface cannot reach such a steady-state.

## 2.4 Conclusions

In this chapter, we have for the first time directly linked electrochemical observations to structural information obtained from high-resolution, real-space EC-STM images of Pt(111) subjected to oxidation-reduction cycles. This approach allows for a quantitative correlation between electrochemical and STM data. Our experiments show that the total roughening process can be divided into two regimes: ‘nucleation & early growth’ followed by ‘late growth’. During the ‘nucleation & early growth’ phase the electrode surface is covered with an increasing number of nanoscale islands. Simultaneously, these islands also increase in radius and slightly in height. In this regime, the roughness extracted from the STM images is not linearly correlated to the hydrogen desorption charge determined from cyclic voltammetry, as geometrically created step sites do not contribute to the electrochemical signal.

The analysis to identify the underlying mechanism during the ‘nucleation & early growth’ phase, indicates that no scaling occurs. Once the islands have coalesced, the existing islands keep growing, predominantly in height. In this ‘late growth’ phase, there is a linear correlation between the surface roughness and the hydrogen desorption charge. In this regime, in contrast to the ‘nucleation & early growth’ regime, each created step site contributes equally to both the electrochemical signal as well as the roughness. Future research is necessary to understand the lack of correlation in the ‘nucleation & early growth’ regime. Our experiment consisting of 170 ORCs is not extensive enough to completely (dis)prove scaling during the ‘late growth’ phase. A key factor in the long-term evolution of the roughened Pt(111) surface is probably the increasing amount of dissolving Pt with prolonged potential cycling.

## References

1. Wagner, F. T. & Ross, P. N. LEED spot profile analysis of the structure of electrochemically treated Pt(100) and Pt(111) surfaces. *Surf. Sci.* **160**, 305–330 (1985).
2. Aberdam, D., Durand, R., Faure, R. & El-Omar, F. Structural changes of a Pt(111) electrode induced by electrosorption of oxygen in acidic solutions: a coupled voltammetry, LEED and AES study. *Surf. Sci.* **171**, 303–330 (1986).
3. You, H. & Nagy, Z. Oxidation-reduction-induced roughening of platinum (111) surface. *Phys. B Condens. Matter* **198**, 187–194 (1994).
4. You, H., Zurawski, D. J., Nagy, Z. & Yonco, R. M. In-situ x-ray reflectivity study of incipient oxidation of Pt(111) surface in electrolyte solutions. *J. Chem. Phys.* **100**, 4699 (1994).
5. Nagy, Z. & You, H. Applications of surface X-ray scattering to electrochemistry problems. *Electrochim. Acta* **47**, 3037–3055 (2002).

- Sugawara, S. & Itaya, K. In situ scanning tunnelling microscopy of a platinum {111} surface in aqueous sulphuric acid solution. *J. Chem. Soc. Faraday Trans. 1 Phys. Chem. Condens. Phases* **85**, 1351 (1989).
- Itaya, K. In situ scanning tunneling microscopy of platinum (111) surface with the observation of monatomic steps. *J. Vac. Sci. Technol. A Vacuum, Surfaces, Film.* **8**, 515 (1990).
- Sashikata, K., Furuya, N. & Itaya, K. In situ electrochemical scanning tunneling microscopy of single-crystal surfaces of Pt(111), Rh(111), and Pd(111) in aqueous sulfuric acid solution. *J. Vac. Sci. Technol. B Microelectron. Nanom. Struct.* **9**, 457 (1991).
- Breuer, N., Funtikov, A., Stimming, U. & Vogel, R. In situ electrochemical STM imaging of roughened gold and platinum electrode surfaces. *Surf. Sci.* **335**, 145–154 (1995).
- Furuya, N. & Shibata, M. Structural changes at various Pt single crystal surfaces with potential cycles in acidic and alkaline solutions. *J. Electroanal. Chem.* **467**, 85–91 (1999).
- Björling, A., Ahlberg, E. & Feliu, J. M. Kinetics of surface modification induced by submonolayer electrochemical oxygen adsorption on Pt(1 1 1). *Electrochem. commun.* **12**, 359–361 (2010).
- Björling, A. & Feliu, J. M. Electrochemical surface reordering of Pt(111): A quantification of the place-exchange process. *J. Electroanal. Chem.* **662**, 17–24 (2011).
- Björling, A., Herrero, E. & Feliu, J. M. Electrochemical oxidation of Pt (1 1 1) vicinal surfaces: effects of surface structure and specific anion adsorption. *J. Phys. Chem. C*, 15509–15515 (2011).
- Gómez-Marín, A. M. & Feliu, J. M. Pt(111) surface disorder kinetics in perchloric acid solutions and the influence of specific anion adsorption. *Electrochim. Acta* **82**, 558–569 (2012).
- Gómez-Marín, A. M. & Feliu, J. M. Oxide growth dynamics at Pt(111) in absence of specific adsorption: A mechanistic study. *Electrochim. Acta* **104**, 367–377 (2013).
- Löffler, T., Bussar, R., Xiao, X., Ernst, S. & Baltruschat, H. The adsorption of ethene on vicinally stepped electrode surfaces and the effect of temperature. *J. Electroanal. Chem.* **629**, 1–14 (2009).
- Wakisaka, M., Asizawa, S., Uchida, H. & Watanabe, M. In situ STM observation of morphological changes of the Pt(111) electrode surface during potential cycling in 10 mM HF solution. *Phys. Chem. Chem. Phys.* **12**, 4184–4190 (2010).
- Liu, Y., Barbour, A., Komanicky, V. & You, H. X-ray Crystal Truncation Rod Studies of Surface Oxidation and Reduction on Pt(111). *J. Phys. Chem. C* **120**, 16174–16178 (2016).
- Goryachev, A. *et al.* Synchrotron based operando surface X-ray scattering study towards structure-activity relationships of model electrocatalysts. *ChemistrySelect* **1**, 1104–1108 (2016).
- Drnec, J. *et al.* Initial stages of Pt(111) electrooxidation: dynamic and structural studies by surface X-ray diffraction. *Electrochim. Acta* **224**, 220–227 (2017).
- Ruge, M. *et al.* Structural Reorganisation of Pt(111) Electrodes by Electrochemical Oxidation and Reduction. *J. Am. Chem. Soc.* **139**, 4532–4539 (2017).
- Ruge, M. *et al.* Electrochemical Oxidation of Smooth and Nanoscale Rough Pt(111): An In Situ Surface X-ray Scattering Study. *J. Electrochem. Soc.* **164**, H608–H614 (2017).
- Yanson, Y. I. & Rost, M. J. Structural Accelerating Effect of Chloride on Copper Electrodeposition. *Angew. Chemie Int. Ed.* **52**, 2454–2458 (2013).
- Yanson, Y. I., Schenkel, F. & Rost, M. J. Design of a high-speed electrochemical scanning tunneling microscope. *Rev. Sci. Instrum.* **84**, 023702 (2013).
- Rost, M. in *Encyclopedia of Interfacial Chemistry: Surface Science and Electrochemistry* 180–198 (Elsevier, 2018).
- Clavilier, J., El Achi, K. & Rodes, A. In situ characterization of the Pt(S)-[n(111) x (111)] electrode surfaces using electrosorbed hydrogen for probing terrace and step sites. *J. Electroanal. Chem.* **272**, 253–261 (1989).
- Rodes, A., El Achi, K., Zamakhchari, M. A. & Clavilier, J. Hydrogen probing of step and terrace sites on Pt(S)-[n(111) x (100)] electrodes. *J. Electroanal. Chem.* **284**, 245–253 (1990).
- Rodes, A. & Clavilier, J. Electrochemical study of step reconstruction on platinum surfaces belonging to the [011] zone between Pt(311) and Pt(111). *J. Electroanal. Chem.* **344**, 269–288 (1993).
- Clavilier, J. & Rodes, A. Electrochemical Detection and Characterization at Pt(N,N,N-2) Oriented Electrodes of Multiatomic Step Formation Induced by Quenching at High-Temperatures. *J. Electroanal. Chem.* **348**, 247–264 (1993).

30. Solla-Gullón, J., Rodríguez, P., Herrero, E., Aldaz, A. & Feliu, J. M. Surface characterization of platinum electrodes. en. *Phys. Chem. Chem. Phys.* **10**, 1359–73 (2008).
31. Vidal-Iglesias, F. J., Arán-Ais, R. M., Solla-Gullón, J., Herrero, E. & Feliu, J. M. Electrochemical characterization of shape-controlled Pt nanoparticles in different supporting electrolytes. *ACS Catal.* **2**, 901–910 (2012).
32. Van Der Niet, M. J. T. C., Garcia-Araez, N., Hernández, J., Feliu, J. M. & Koper, M. T. M. Water dissociation on well-defined platinum surfaces: The electrochemical perspective. *Catal. Today* **202**, 105–113 (2013).
33. Huang, Y.-F., Kooyman, P. J. & Koper, M. T. M. Intermediate stages of electrochemical oxidation of single-crystalline platinum revealed by in situ Raman spectroscopy. *Nat. Commun.* **7**, 12440 (2016).
34. Topalov, A. A. *et al.* Dissolution of platinum: Limits for the deployment of electrochemical energy conversion? *Angew. Chem. Int. Ed.* **51**, 12613–12615 (2012).
35. Lopes, P. P. *et al.* Relationships between atomic level surface structure and stability/activity of platinum surface atoms in aqueous environments. *ACS Catal.* **6**, 2536–2544 (2016).
36. Gomez, R., Orts, J. M., Alvarez-Ruiz, B. & Feliu, J. M. Effect of Temperature on Hydrogen Adsorption on Pt(111), Pt(110), and Pt(100) Electrodes in 0.1 M HClO<sub>4</sub>. *J. Phys. Chem. B* **108**, 228–238 (2004).
37. Furuya, N. & Koide, S. Hydrogen adsorption on platinum single-crystal surfaces. *Surf. Sci.* **220**, 18–28 (1989).
38. Domke, K., Herrero, E., Rodes, A. & Feliu, J. M. Determination of the potentials of zero total charge of Pt(100) stepped surfaces in the [011] zone. Effect of the step density and anion adsorption. *J. Electroanal. Chem.* **552**, 115–128 (2003).
39. Giesen, M., Schulze Icking-Konert, G. & Ibach, H. Interlayer Mass Transport and Quantum Confinement of Electronic States. *Phys. Rev. Lett.* **82**, 3101–3104 (1999).
40. Giesen, M. & Ibach, H. On the mechanism of rapid mound decay. *Surf. Sci.* **464**, L697–L702 (2000).
41. Lee, J., Lee, J., Tanaka, T. & Mori, H. In situ atomic-scale observation of melting point suppression in nanometer-sized gold particles. *Nanotechnology* **20**, 475706 (2009).
42. Jacobse, L., Huang, Y. F., Koper, M. T. M. & Rost, M. J. Correlation of surface site formation to nanoisland growth in the electrochemical roughening of Pt(111). *Nature Materials* **17**, 277–282 (2018).
43. Ehrlich, G. & Hudda, F. G. Atomic View of Surface Self-Diffusion: Tungsten on Tungsten. *J. Chem. Phys.* **44**, 1039–1049 (1966).
44. Schwoebel, R. L. & Shipsey, E. J. Step Motion on Crystal Surfaces. *J. Appl. Phys.* **37**, 3682–3686 (1966).
45. Michely, T. & Krug, J. *Islands, Mounds and Atoms Springer Series in Surface Sciences* **1**, 313 (Springer Berlin Heidelberg, Berlin, Heidelberg, 2004).
46. Ibach, H. *Physics of Surfaces and Interfaces* 646 (Springer, 2006).
47. Sekerka, R. F. in *Crystal Growth - From Fundamentals to Technology* (eds Georg Müller, J.-J. M. & Rudolph, P.) 1st ed., 55–93 (Elsevier Science, Amsterdam, 2004).
48. Sekerka, R. F. Equilibrium and growth shapes of crystals: How do they differ and why should we care? *Cryst. Res. Technol.* **40**, 291–306 (2005).
49. Meakin, P. *Fractals, scaling and growth far from equilibrium* 119–159 (Cambridge University Press, 1998).
50. Eells, W. C. Formulas for Probable Errors of Coefficients of Correlation. *J. Am. Stat. Assoc.* **24**, 170–173 (1929).
51. Tong, W. M. & Williams, R. S. Kinetics of Surface Growth: Phenomenology, Scaling, and Mechanisms of Smoothing and Roughening. *Annu. Rev. Phys. Chem.* **45**, 401–438 (1994).
52. Sugawara, Y., Sasaki, M., Muto, I. & Hara, N. Dissolution of Platinum Single Crystal Surfaces under Potential Cycling in Sulfuric Acid Solution. *ECS Trans.* **64**, 81–87 (2014).

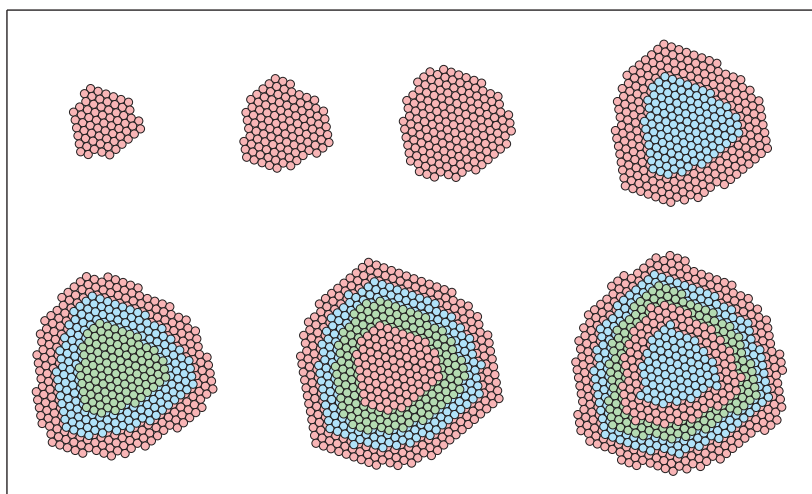


### 3 | Atomic-scale identification of the electrochemical roughening of platinum

---

*Electrode degradation under oxidizing conditions is a major drawback for large scale applications of platinum electrocatalysts. Subjecting Pt(111) to oxidation-reduction cycles is known to lead to the growth of nanoislands. We study this phenomenon using a combination of simultaneous *in situ* electrochemical scanning tunneling microscopy and cyclic voltammetry. Here, we present a detailed analysis of the formed islands deriving the (evolution of the) kinetic-average island shape. From the island shapes, we determine the densities of atomic-scale defect sites, like steps and facets, which show an excellent correlation to the different voltammetric hydrogen adsorption peaks. Thus, we can directly attribute the hydrogen peaks to the presence of individual surface sites. This delivers new insights into the growth and evolution of the nanoislands as well as into the degradation of real electrocatalysts.*

---



---

This chapter is based on Jacobse, L., Rost, M.J. & Koper, M.T.M. submitted.

Subjecting a platinum electrode to oxidation-reduction cycles (ORCs) is one of the most commonly performed experiments in surface electrochemistry. This pre-treatment cleans the platinum surface and results in a reproducible (albeit typically unknown) surface structure.<sup>1-3</sup> It is well-known that the Pt surface undergoes a significant structural transformation during this process, as is most dramatically illustrated when starting with a well-defined Pt(111) single crystal electrode.<sup>4</sup> Understanding the roughening of a Pt(111) electrode by ORCs at the atomic scale has therefore been a long-standing goal in fundamental electrochemistry.

Voltammetric experiments provide a fingerprint of the average surface structure, as the adsorption and desorption of hydrogen is very sensitive to the atomic scale surface sites available for this reaction. However, without direct, *in situ* spatial information, data from cyclic voltammetry (CV) alone have been insufficient to describe the (evolution of) the surface structure at the atomic scale.<sup>4-6</sup> On the other hand, spatially resolved data, from *ex situ* low energy electron diffraction (LEED)<sup>7,8</sup>, *in situ* x-ray reflectivity<sup>9-16</sup>, and *in situ* electrochemical scanning tunneling microscopy (EC-STM)<sup>17-23</sup> experiments, have also not been able to explain the complex evolution of the electrochemical fingerprint signal. By combining *in situ* EC-STM with CVs in a single experiment, we have recently demonstrated that the growth of nano-scale islands, and therefore the electrode roughness, is directly correlated to the integrated hydrogen desorption in the voltammetric signal. This integrated correlation, however, is 'blind' to the different contributions from individual local surface geometries/sites.

In this chapter, we extract the kinetic, atomic-scale nanoisland shape (as a function of the number of applied ORCs) from the EC-STM images and use these shapes to determine the densities of specific undercoordinated ('defect') sites, like steps, facets, and kinks. Furthermore, we disentangle the hydrogen desorption region of the CVs, measured in the same experiment, to quantify the different 'defect'-related contributions. Correlating these two sets of data allows for a direct determination of the reactivity of the different sites that are present at the roughened Pt surface. Therefore, we can pinpoint the individual peaks in the electrochemical hydrogen adsorption signal to specific surface sites. Additionally, this information forms crucial input for understanding the stability of platinum electrodes under potential cycling conditions, and it also provides insight into the interpretation of the voltammetric features of a wide variety of Pt samples, from single crystal surfaces to nanoparticles.

### 3.1 Electrochemical measurements

The desorption of underpotential deposited hydrogen ( $H_{\text{UPD}}$ ,  $0 < U_s < 0.4 \text{ V}$ ) contains detailed information on the present average atomic surface structure. Initially, this region only shows a very broad, flat feature related to the hydrogen desorption from the atomically smooth (111) terraces, as indicated by the black line in Fig. 3.1. From this starting situation, the sample potential is cycled between 0.06 and 1.35 V (at  $50 \text{ mV}\cdot\text{s}^{-1}$ ), leading to the growth of nanoislands as was shown in Chapter 2. Simultaneously, the electrochemical fingerprint changes drastically, as shown in Fig. 3.1 from blue to red. The appearance of four distinct new peaks, labeled  $A_{1-4}$ , indicates the formation of new surface geometries.

To enable a correlation of the CV features to the site densities in the average atomic-scale island shape determined from the STM images, it is necessary to disentangle the charge corresponding to these four  $H_{\text{UPD}}$  peaks. Several approaches are presented, for single crystalline and nanoparticle samples, in the literature.<sup>24-27</sup> However, especially for very complex surfaces, deconvoluting the

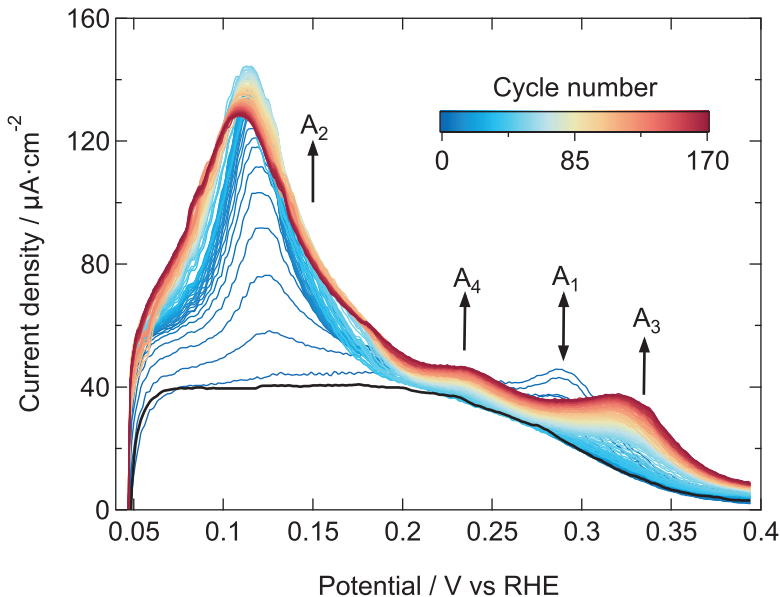


**Fig. 3.1 | Evolution of the electrochemical fingerprint upon surface roughening:**  $H_{\text{UPD}}$  region of the 170 subsequent (from blue to red) oxidation-reduction cycles between 0.06 and 1.35 V. The CV of the initial, well-prepared Pt(111) surface is shown in black. Four ‘defect’-related peaks, labeled  $A_{1-4}$ , are observed during the overall process. The potential scan rate is  $50 \text{ mV}\cdot\text{s}^{-1}$  and the electrolyte is 0.1 M  $\text{HClO}_4$ .

$H_{\text{UPD}}$  region shows some discrepancy with results from other electrochemical experiments.<sup>24,26</sup> One of the underlying reasons for this is that the broad (111) terrace feature (black line in Fig. 3.1) changes its shape for more narrow terraces and, overlaps with all four ‘defect’ peaks.<sup>28</sup> Thus, the terrace feature is typically considered to be a background signal.<sup>6</sup> In our fitting procedure, we therefore also follow this approach by keeping the terrace contribution constant for all cycles. As the number of terrace sites is expected to decrease during the surface roughening, we most likely underestimate the charge related to  $H_{\text{UPD}}$  at ‘defects’. One could imagine to further refine the fitting procedure by using additional data from e.g. regular single crystals or the EC-STM site densities to constrain the fit functions. Such corrections could prove valuable in a more accurate determination of the correlation prefactors (vide infra), but are beyond the scope of this study, as here we aim here for pinpointing certain sites to certain peaks only. Following McCrum and Janik, the broad terrace feature is fitted with an inverse hyperbolic cosine function and the  $A_{1-4}$  peaks are fitted with gaussians.<sup>26</sup> To capture the changing shape of the  $A_2$  peak, it is necessary to use a summation of two gaussians. More information on the fit and its quality is provided in Appendix C.

Figure 3.2A shows the integrated charges of the  $A_{1-4}$  peaks in the CVs as a function of the number of applied ORCs. The overall process can be separated in different regimes: both the  $A_1$  and  $A_2$  peaks increase during the first few ORCs, then  $A_1$  disappears while  $A_2$  keeps increasing continuously. After prolonged cycling, the  $A_3$  and  $A_4$  peaks appear after 36 and 60 ORCs, respectively. The  $A_1$  and  $A_2$  peaks (and their evolution) have been studied in detail and were ascribed to the presence of {100} and {111} steps at the surface, respectively.<sup>4-6</sup> It is expected that steps form during the roughening of an atomically flat surface. However, it is striking that the charge underneath the  $A_2$  peak is increases continuously, whereas the  $A_1$  peak shows a maximum after two cycles, and subsequently decays to completely disappear after 10 ORCs. Based on its peak potential, one expects the  $A_3$  peak to be related to the formation of {100} terraces.<sup>29,30</sup> The  $A_4$  peak is also known as ‘the third hydrogen peak’.<sup>31,32</sup> Although the exact origin of this peak is heavily debated, it appears to be related to the presence of (1x2){110} sites at the surface. Especially for the latter two peaks, it is not clear *a priori* how and if the expected atomic geometries are formed on the roughened surface. Finally, it is important to stress that the  $A_2$  peak changes shape and peak potential upon prolonged potential cycling. This could indicate that this peak actually consists of more than one contribution.

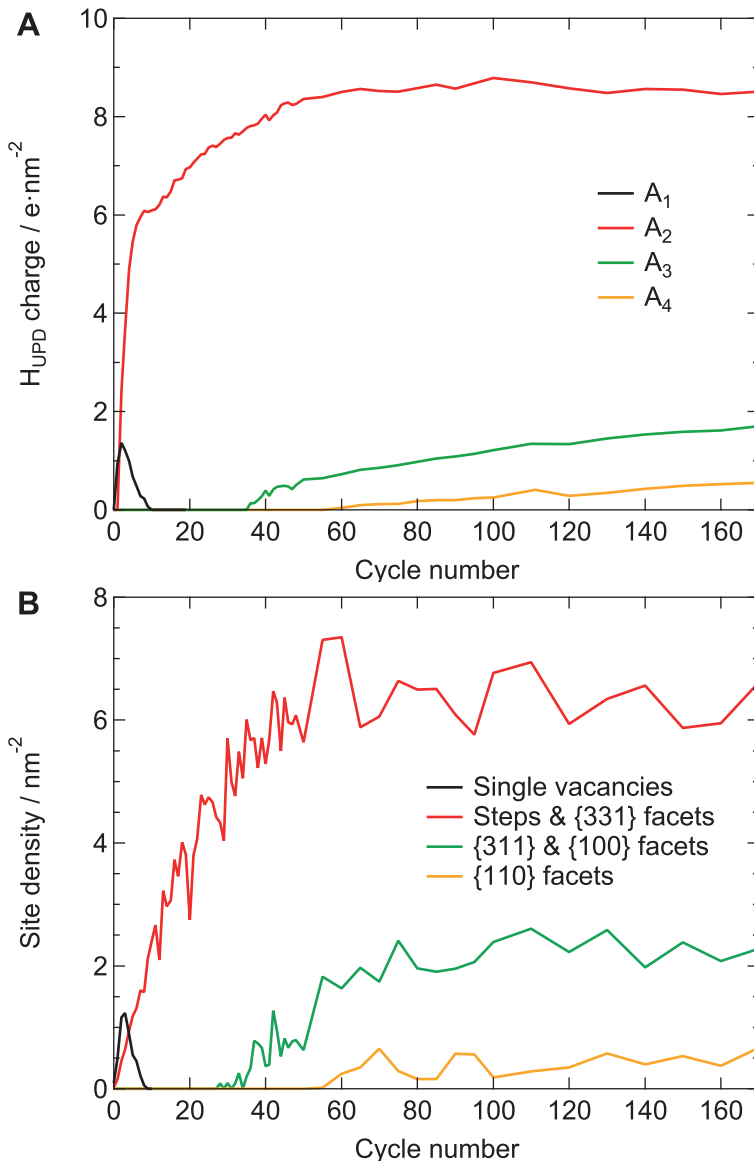


**Fig. 3.2 | Evolution of peak charges and corresponding adsorption site densities:** (A) The integrated charges of the  $A_{1-4}$  peaks in the  $H_{\text{UPD}}$  region shown in Fig. 3.1. (B) The densities of single vacancies, step sites + {331} facets, {311} + {100} facets, and {110} facets as counted from the average atomic-scale island shapes in Fig. 3.3B. Note that {221} and {211} facets (blue in Fig. 3.4) exhibit the same reactivity as ‘separated defects’ (see main text). Further motivations behind grouping (correlating) the various sites are provided in the main text.

## 3.2 EC-STM site densities

In the following, we discuss the origin of the evolution of the electrochemical fingerprint signal by the determination of surface site densities extracted from the average island shapes from the EC-STM images. The result of this analysis is already shown in Fig. 3.2B for comparison.

Figure 3.3A shows parts of the EC-STM images after 0, 4, 8, 15, 28, 50, and 170 ORCs. These images have been selected from the full set of  $230 \times 230 \text{ nm}^2$  images (see Fig. 2.2 and Ref. [33]), which have been measured with constant tip and sample potential (0.45 and 0.4 V, respectively). With a pixel density of  $2.25 \text{ \AA} \cdot \text{pixel}^{-1}$ , our images are not directly atomically resolved. In addition, considering the surface roughness and tip convolution, full atomic resolution would be extremely challenging. Nonetheless, the average atomic-scale island shape representative for a certain number of ORCs can be determined by a careful and detailed data analysis, described in Appendix C. In brief, the images are corrected for drift and height offset; approximate island centers are determined by threshold and watershed functions; and island boundaries are determined by a combination of Laplace filtering and the construction of Voronoi cells. In the next step, height profiles of all individual islands present in one EC-STM image are averaged, using the local maximum as island center. Finally, the average island shape is fitted with an fcc lattice, taking into account the main step directions on the surface.

From repeated experiments (see Appendix C) we argue that the shapes of the islands on our wide terraces are not affected by the step edges present. Thus, any asymmetry deviating from the threefold symmetry of the Pt(111) surface originates from the shape of the STM tip. To minimize this imaging artefact, the fitting procedure imposes a threefold island symmetry. In Chapter 2, we have already shown that the area visualized in our EC-STM images can be used to describe the roughening of the entire Pt(111) surface. Except for the first cycles, when the island density is rather low, the analysed areas typically contain between 400 to 500 individual islands. Because of the large number of averaged islands, the resulting island structure is considered to be representative of the statistical growth shape after a certain number of ORCs.<sup>34</sup> Note that such growth shapes differ from classical Wulff shapes in thermodynamic equilibrium.

The results of the fitting procedure for the EC-STM images in Fig. 3.3A are depicted in Fig. 3.3B. The full series of island structures is provided as a movie in Appendix D. From the atomic island structures it is now possible to determine the

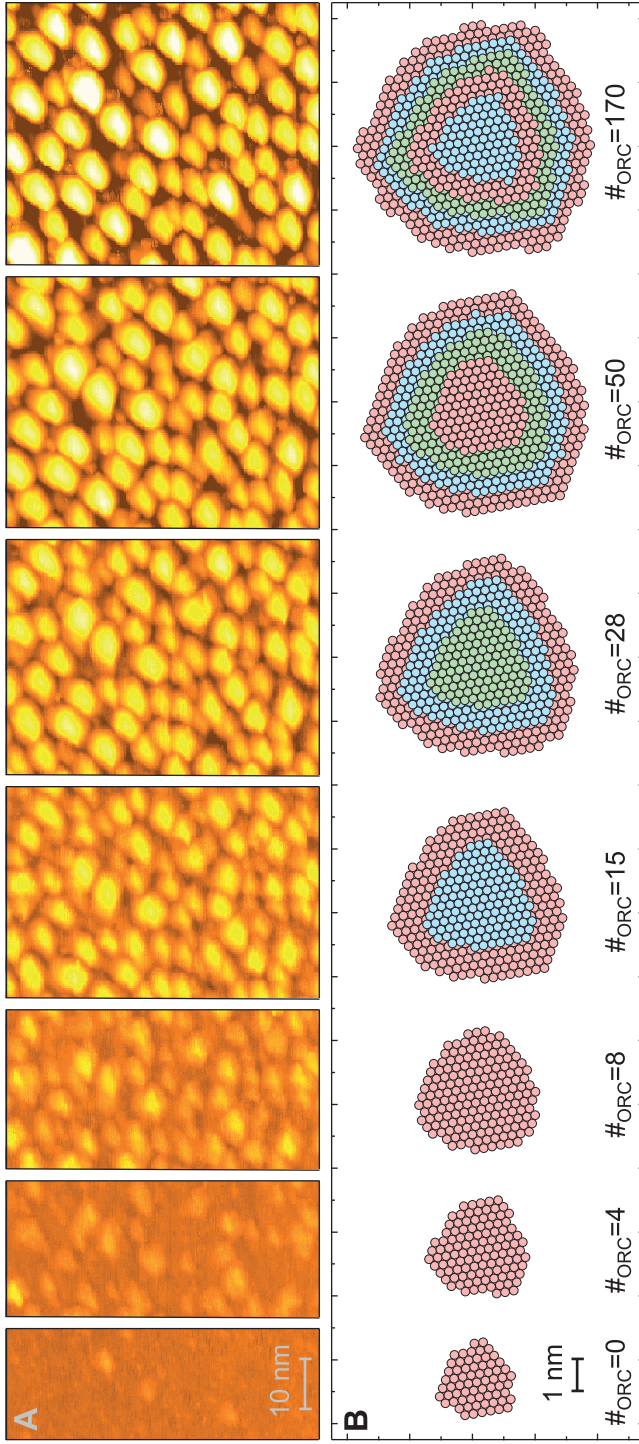


**Fig. 3.3 | EC-STM images and average nanoisland structures:** (A) parts of EC-STM images after 0, 4, 8, 15, 28, 50, and 170 ORCs (from left to right) illustrating the roughening of a single surface area. The original, individual images are  $230 \times 230 \text{ nm}^2$ , recorded with  $U_{\text{tip}} = 0.45 \text{ V}$ ,  $U_{\text{sample}} = 0.4 \text{ V}$ , and  $I_{\text{tunneling}} < 300 \text{ pA}$ . Note that the total contrast is the same for the different images. The full set of EC-STM images is available in Ref. [33]. (B) The average atomic-scale growth structure of the islands as determined from the EC-STM images for the same situations as shown in (A). The different colors indicate the different atomic layers in the island. The full image sequence is provided in Appendix D.

densities of the different sites at the surface. Detailed descriptions and counting rules for the various surface geometries can be found in Appendix C, but we provide here the general considerations. Due to the symmetry of the Pt(111) surface, we distinguish three different directions in the surface plane as shown in Fig. 3.4A-C. In the following, we will refer to these directions according to the step site geometry at the corresponding side of the island: {111} steps are found at the {111}-side (Fig. 3.4A) and {100} steps at the {100}-side (Fig. 3.4C). Step edges in the third direction, oriented at midangle between these two densely packed directions, are typically described as '100% kinked'.<sup>35</sup> As these steps have a {112} geometry, we label this as the {112}-side (Fig. 3.4B). Note that for the {111}-side, a rectangular {110} step unit cell is used for counting. This simplifies the site assignment of the total surface, as the {110} unit cell is orthogonal to the step direction.

Additionally, the spacing between 'defects' (steps) in the different layers is known to have a significant effect on their electrochemical reactivity.<sup>28</sup> Step edges that are separated by less than two terrace atoms (as on the (221) and (211) surfaces) bind hydrogen stronger, indicated by a more positive peak potential, than wider spaced step edges. To capture this effect, we consider: (1) step edges separated by more than two terrace atoms ('separated defects', e.g. {110} and {100} steps); (2) step edges separated by two terrace atoms ('wide facets', e.g. {221} and {211} facets); (3) step edges separated by one terrace atom ('narrow facets', e.g. {331} and {311} facets); and (4) adjacent step edges ('low index facets', e.g. {110} and {100} facets). Unit cells of the steps and facets for both the {111}- and {100}-side are shown in Fig. 3.4A and C, respectively. The terrace width is also taken into account at the {112}-side (see Fig. 3.4B) and when counting corner and kink sites as explained in Appendix C. Finally, we also take into account that terrace sites that are adjacent to a 'defect'-site could exhibit a different reactivity. Corner and kink sites occur not only at very low density, but also show a large variation in density between subsequent ORCs. Sites related to the {112}-side occur at slightly higher densities than kinks, but again with large variations. These variations are most likely fitting artifacts. In the rest of our analysis, we will, therefore, group all different 'defect' sites according to the two most prominent island sides (i.e. the {111}- and {100}-side) and the four different terrace widths (facets) shown in Fig. 3.4A-C. The densities of these eight different groups of sites as a function of cycle number are shown in Fig. 3.4D. It is important to note that kinks at the {111}-side are, due to their geometry, classified as belonging to the {100}-side and *vice versa*.<sup>36</sup>

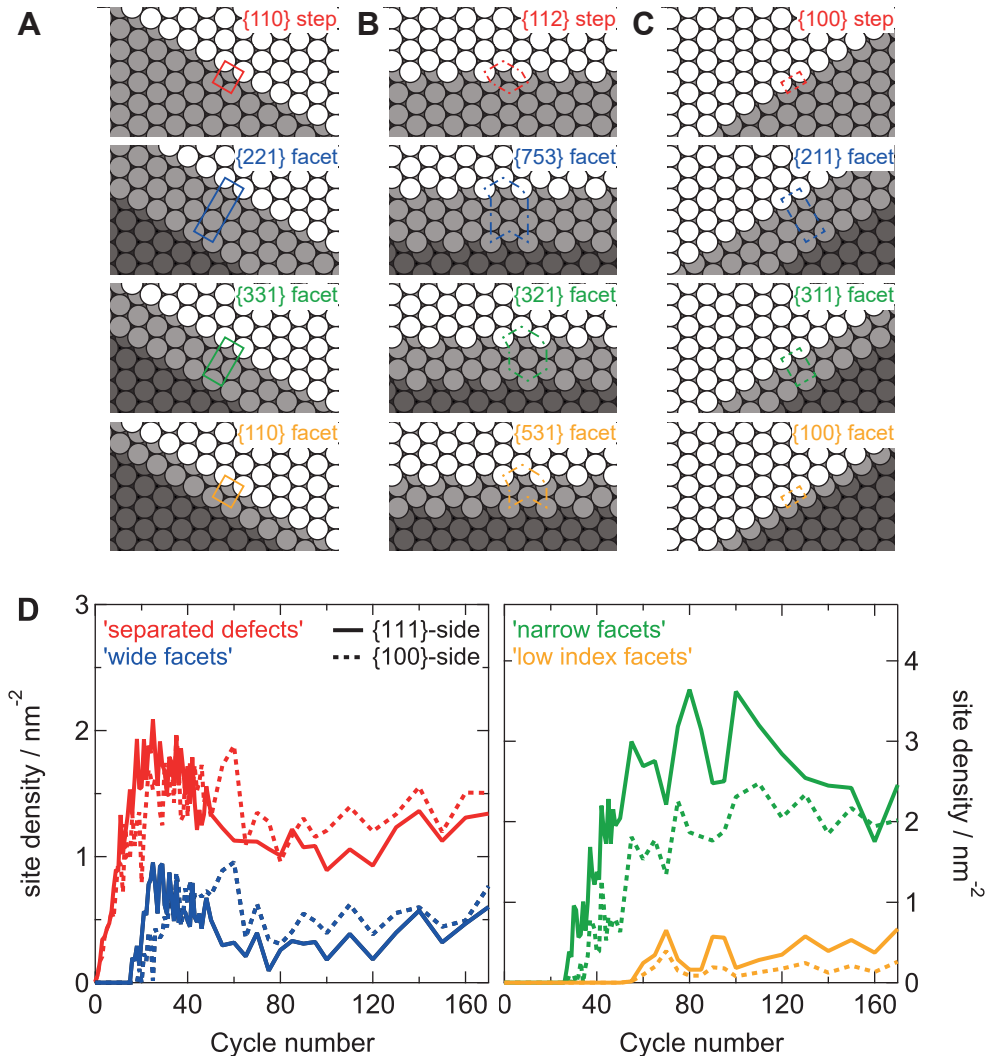


**Fig. 3.4 | Unit cells and time evolution of ‘defect’ site densities derived from average nanoisland structures:** (A-C) Representative unit cells for the {111}, {112}-, and {100}-side step/facet geometries, respectively. The structures range from ‘separated steps’ (top) to ‘low index facets’ (bottom). All counting rules and unit cells for other possible structures, as well as all individual site densities are provided in Appendix C. (D) Site densities for the ‘separated defects’ & ‘wide facets’ (left), and ‘narrow facets’ & ‘low index facets’ (right) for both the {111}- and {100}-side (solid and dashed lines respectively).

Figure 3.4D shows that, initially, only ‘separated defects’ form, whereas the different kinds of facets only appear after prolonged potential cycling (after 16, 27, and 55 ORCs for ‘wide’, ‘narrow’, and ‘low index’ facets, respectively). This is in line with the observations in Chapter 2, where we described that the nanoislands first nucleate and (mainly) grow laterally, before growing in height. Height growth, while keeping the island base fixed, leads to the formation of facets. Although the islands are rather symmetric, the formation of facets is initially seen at slightly higher intensity at the {111}-side. This is because the unit cell of a {110} step is longer than that of a {100} step. The number of terrace sites on the island (see Appendix C) first increases, but starts decreasing when facets are formed. Including also the (original) terrace sites that are not part of the island, a continuous decrease is observed.

### 3.3 Correlating site densities to reactivity

Equipped with both the evolution of the disentangled electrochemical fingerprint and the ‘defect’ site densities, we now correlate these two sets of data to each other. We start the discussion with the simplest case, i.e. the situation between 10 and 30 ORCs. In this regime of the roughening process, the  $A_2$  peak is the only ‘defect’ feature in the CV. The absence of the  $A_1$  peak around 0.27 V indicates that there are no {100} steps at the surface. If the {111}-side is, under all conditions, significantly more stable (lower free energy) than the {100}-side, we should observe triangular nanoislands composed of only {111}-sides. However, the images in Fig. 3.3B, e.g. after 15 ORCs, clearly show extended 100-type step lengths existing in the island shape. The site densities in Fig. 3.4D also clearly indicate substantial densities of {100} step sites. The only way to explain the significant step length at the {100}-side of the island without the actual formation of {100} step sites is by assuming that these step edges are in reality ‘roughened’\* and thereby composed of small segments of {110} steps as illustrated in Fig. 3.5. This hypothesis is supported by literature data on the roughening of Pt(11 10 10), a surface which naturally contains regular {100} steps. These data show that {100} step edges are highly unstable during the ORCs: their voltammetric feature diminishes quickly upon potential cycling (almost completely during the first ORC) and is replaced by a {110} feature.<sup>6</sup> Similar observations were made by Rodes and Clavilier, who

---

\* Note that, strictly speaking, step roughening occurs already at each temperature unequal to 0 K, as there is always enough entropy to place a kink into a step: one only has to increase the step lengths.<sup>36</sup>

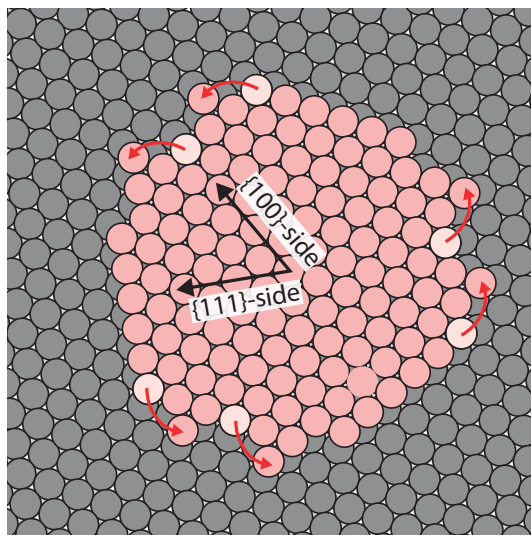


**Fig. 3.5 | Step ‘roughening’ example:** Example of a (mass conserved) step ‘roughening’ to minimize the number of  $\{100\}$  step sites. Such step structures are necessary to explain the island symmetry in combination with the presence of only one ‘defect’ peak in the CVs between 10 and 30 ORCs, see Fig. 3.2.

studied the electrochemical behavior of various single crystal surfaces with  $\{100\}$  step edges as a function of annealing/cooling conditions and potential cycling.<sup>37</sup>

The ‘roughened’ hexagonal islands (Fig. 3.5) will only be preferred over triangular islands if the step sites at the  $\{100\}$ -side are stabilized somewhere during potential cycling. This expectation is supported by DFT calculations, which indicate that Pt(100) is more stable than Pt(110) at high potentials ( $>0.9\text{V}$  for the surface oxide and  $>1.05\text{V}$  for adsorbed O/OH).<sup>38</sup> Unfortunately, the step edge ‘roughening’ is not captured in our fitting results. The reason for this is both the averaging process for the determination of the average island shape and the limited resolution of our EC-STM images. The study by Rodes and Clavilier has shown that when ‘separated’ step edges are roughened, the increase in charge of the  $A_2$  peak is twice the decrease in charge of the  $A_1$  peak.<sup>37</sup> This is ascribed to the formation of two kink sites from one step site. Thus, in our correlation analysis we argue that each ‘separated’  $\{100\}$  step site contributes double to the  $A_2$  peak. The facets at the  $\{100\}$ -side and their ‘roughening’, which could also contribute to the  $A_2$  peak, are discussed below.

Let us now focus on the  $A_3$  and  $A_4$  peaks, which appear after further potential cycling. Their ‘late’ appearance indicates that they are related to the formation of specific facets due to the height growth of the nanoislands. This is confirmed when inspecting the average island shape after 28 ORCs in Fig. 3.3B: all standard step and kink sites are present, but the  $A_3$  and  $A_4$  peaks do not yet contribute to the CV. The charge of the  $A_3$  peak is clearly correlated to the density of {311} facet sites (correlation coefficient  $r=0.92$ , see Appendix C). This is in line with the  $A_3$  peak potential ( $\sim 0.32$  V), which is slightly higher than that of {100} step sites.<sup>28</sup> Interestingly, this correlation must also mean that the {311} facet is stable enough to withstand the step edge ‘roughening’, which occurs for the ‘separated’ {100} step sites. Indeed, roughening experiments of Pt(311) by thermal or electrochemical adsorption of oxygen do not show any formation of {110} step/kink sites. The stabilization of straight step edges for narrow terraces can be ascribed to the repulsive interaction between step edges of equal sign<sup>36</sup> and has been observed before for stepped Pt surfaces.<sup>39</sup> Literature data is not consistent on the stability of the {211} facet. Thermal oxidation experiments indicate that this step edge also withstands step ‘roughening’<sup>37</sup>, but potential cycling experiments suggest the opposite.<sup>40</sup> As the {211} facets appear 10 cycles before the emergence of the  $A_3$  peak, we conclude that also this facet must roughen and thus contribute to the  $A_2$  peak instead. Most likely, the {100} facets contribute as well to the  $A_3$  peak.<sup>28</sup> Indeed, the summation of the densities of {311} and {100} facets (the green line in Fig. 3.2B) leads to a slightly higher correlation coefficient (0.93, see Appendix C).

As the  $A_4$  peak appears later than the  $A_3$  peak, it is expected that this peak is related to the formation of facets that are even narrower than the {311} facets. Considering the peak potential, these sites are likely formed at the {111}-side of the islands. Nonetheless, the correlation between the {110} facets (yellow line in Fig. 3.2B) and the  $A_4$  charge is rather low ( $r=0.54$ ). Upon closer inspection (see Appendix C), it becomes clear that this is mainly due to the large variation in the density of {110} facets between subsequent cycles. After applying a moving average filter (averaging over 5 data points) to the {110} facet density, the correlation coefficient is significantly increased ( $r=0.93$ , see Appendix C).

The  $A_2$  peak for the roughened surface is much broader than for a regularly stepped single crystal. This complicates the separate identification of {111}-side facets, as these features overlap in our CVs. The better correlation between the  $A_2$  charge and the site densities when the {331} facet sites are included ( $r=0.88$  vs 0.76) confirms this overlap. The correlation analysis also indicates that the ‘wide facets’ are better described as ‘separated defects’, i.e. the adjacent terrace

sites do not contribute to the  $A_2$  peak (see Appendix C). This suggests that the small facet-related features as observed for Pt(221) and Pt(211), are actually due to the terrace width distribution of these surfaces.<sup>28</sup> The summation of all sites contributing to the  $A_2$  peak (all ‘separated defects’ and the {331} facets) is shown as the red curve in Fig. 3.2B.

Most puzzling is the observation that there is no surface site in the adatom islands that, after appearing during the first two cycles, disappears completely after 10 ORCs, as suggested by peak  $A_1$ . Importantly, the islands are only one atom high when this peak is present, which excludes that it originates from the formation of some kind of facet site. One could imagine that this peak is related to the presence of ‘separated’ {100} step sites which did not yet ‘roughen’, e.g. due to a very small island size. However, if that would be true, this peak would reappear once a new layer nucleates on top of an existing island, i.e. after 9, 16, 30, and 55 ORCs. This is not the case. Thus, we conclude that this peak must be related to some surface site that is not present in the adatom islands at all. Furthermore, it is also unlikely that this peak originates from a surface miscut. This would neither explain why it increases during the first cycles, nor that the charge is 2-3 orders of magnitude larger than what would be expected for such a signal. In conclusion, we need a surface site that is solely present in the very beginning of the roughening process.

As the surface roughening is (almost completely) mass conserved<sup>41–44</sup>, we observed in Chapter 2 (see also Appendix B) that vacancies form simultaneously with the adatom islands. These small vacancies are extremely difficult to resolve in STM and will, especially at low coverages, not contribute to the average island structure. If we neglect the small amount of dissolving Pt under our experimental conditions, the number of single vacancies must be the same as the number of adatoms forming the average island shape. This implies the existence of additional ‘defect’ features in the form of terrace atoms that are immediately adjacent to a vacancy site. Note that the nucleation of single vacancies into vacancy islands of specific sizes will play a role in the expected current densities. The total electrochemical signal resulting from ‘defects’ adjacent to a vacancy site can thus be described by:

$$\begin{aligned} j_{vac} &\propto A_{island} \cdot (P_{terrace})^{f(n)} \\ j_{vac} &\propto A_{island} \cdot (1 - 2 \cdot A_{island})^{f(n)}, \end{aligned} \quad (3.1)$$

where  $j_{vac}$  is the expected current density due to vacancy-related steps,  $A_{island}$

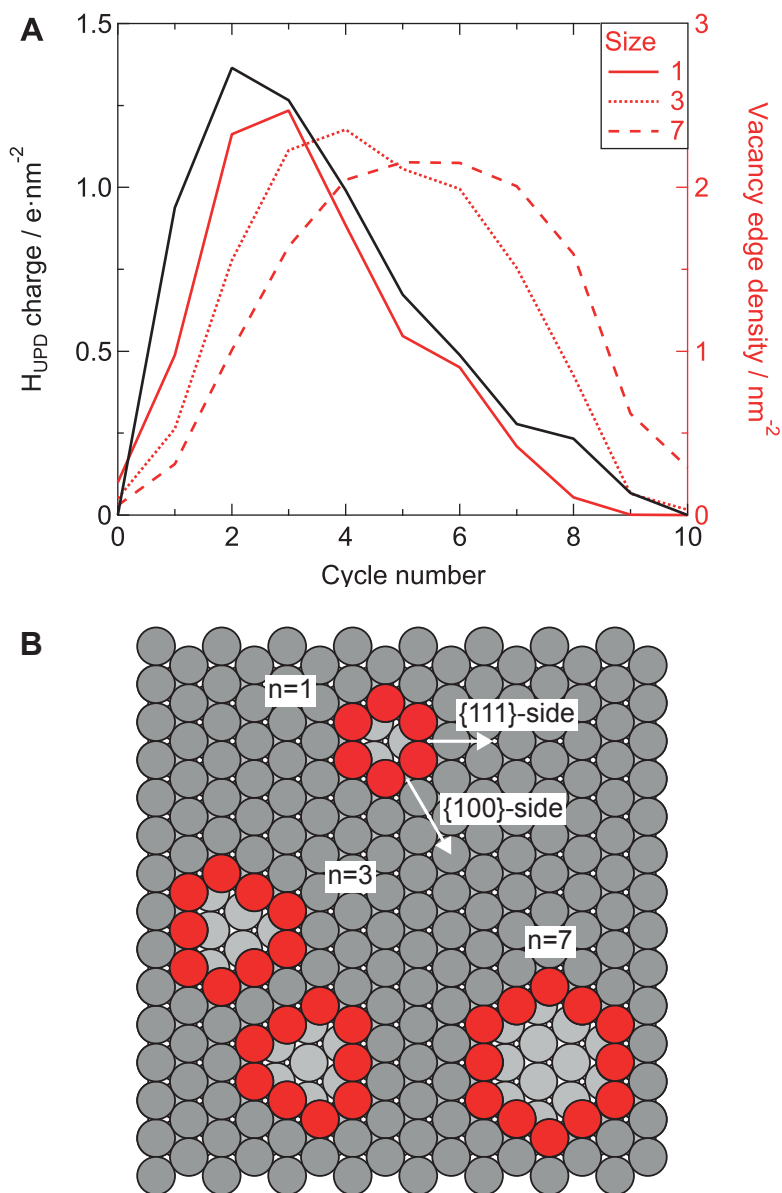


**Fig. 3.6 | Vacancy site formation:** (A) Comparison between the charge of the  $A_1$  peak (black) and the expected vacancy signal (red) according to Eq. 3.1 for single vacancies and vacancy islands of 3 and 7 atoms. (B) Affected vacancy edge sites (red) for single vacancies and vacancy islands of 3 and 7 atoms. The arrows at the single vacancy indicate the two nonequivalent directions. Note that two different island orientations exist for the  $n=3$  vacancy island.

is the adatom island coverage,  $P_{terrace}$  is the probability that the adjacent site was originally a terrace site (i.e. not a vacancy or adatom site), and  $f(n)$  is the number of adjacent terrace sites per vacancy site that has to be present to form a vacancy island of size  $n$  (i.e.  $f(1)=6$ ,  $f(3)=3$ ,  $f(7)=\frac{12}{7}$ ). Note that the distribution and existence of single vacancies and vacancy islands in a Pt(111) surface can be significantly more complicated, as this surface is on the verge of forming a reconstruction.<sup>45–47</sup>

Figure 3.6A shows the expected vacancy signal (red) for the formation of single vacancies and for vacancy islands of 3 and 7 atoms (so-called magic clusters<sup>48</sup>) together with the charge underneath the  $A_1$  peak (black). The corresponding structures are shown in Fig. 3.6B. The best correlation to the charge of the  $A_1$  peak ( $r=0.96$ ) is obtained when we take into account the formation of single, isolated vacancies. This signal is also shown as the black curve in Fig. 3.2B. Considering the simplicity of our approach, the level of correlation is remarkable. When the  $A_1$  peak reaches its maximum, the distance between the vacancies would only be 3-4 atoms. At these (and higher) coverages, one would expect to observe the nucleation of vacancy islands. Thus the total signal would become a weighted average of the different curves shown in Fig. 3.6A, leading to an additional tail after more ORCs. On the other hand, individual vacancy formation is likely to occur within (larger) vacancy islands. In any case, we can conclude that the  $A_1$  peak is related to the formation of vacancy sites, although the full explanation will likely be more complex than our simple model.

The peak potential of the  $A_1$  peak suggests that its signal originates only from  $\{100\}$  sites. As the correlation prefactor is close to two (see the y-axes of Fig. 3.6A and the discussion below), it is tempting to argue that the vacancies lead to the formation of equal amounts of both  $\{100\}$  and  $\{110\}$  step sites. Although a step edge description is probably not directly valid for single vacancies, it is clear that these sites have two nonequivalent sides, as indicated in Fig. 3.6B. Upon nucleation of vacancy islands, ‘step roughening’ could occur such that the vacancy-related ‘defects’ now only contribute to the  $A_2$  peak. However, with the limited information we have on the vacancy sites, it seems impossible to disentangle this signal. Nevertheless, Fig. 3.2 indicates that during the first  $\sim 20$  cycles, the number of sites contributing to the  $A_2$  peak is underestimated (see also Appendix C). The discrepancy is largest during the first three ORCs and then diminishes, which hints at a relationship to the formation of vacancy (island) sites.

The analysis above shows that site densities extracted from EC-STM images are in very good accordance with the evolution of the cyclic voltammetry during the surface roughening. Finally, it is interesting to look at the prefactors of the correlations, which are worked out and shown in detail in Appendix C. In the traditional picture of adsorption/desorption of a single hydrogen atom at each ‘defect’ site, one would expect all prefactors to be unity.<sup>37,49–51</sup> However, recent studies demonstrate that the ‘defect’ features in the H<sub>UPD</sub> region are actually not just adsorption/desorption of hydrogen, but rather a replacement of hydrogen atoms by hydroxyl groups.<sup>52,53</sup> As a result, the expected transferred charge per surface site is somewhat larger than 1 e<sup>-</sup>. Experimental results point in this direction, albeit without quantification, for widely spaced {110} step edges<sup>54</sup>. However, it is not directly clear to what extent these values are affected by the applied fitting procedure. Our prefactors for the A<sub>1</sub> and A<sub>2</sub> peaks (1.07 ± 0.07 and 1.46 ± 0.04 e<sup>-</sup>/site, respectively) match these expectations. The prefactors for the A<sub>3</sub> and A<sub>4</sub>-peaks (0.56 ± 0.02, and 0.77 ± 0.06 e<sup>-</sup>/site, respectively), on the other hand, seem to be too small. However, this can be explained by our fitting procedure, in which we keep the terrace contribution constant. Single crystal experiments show that the broad (111) terrace feature changes shape, i.e. loses intensity mainly at high potentials, due to the formation of narrow terraces.<sup>28</sup> This leads to an underestimation of the ‘defect’-peaks, in particular the A<sub>3</sub> and A<sub>4</sub> peaks, which appear with narrowing terraces. Finally, one should be aware of the limitations of counting absolute site densities from the EC-STM images. As it is impossible to fully correct for tip convolution effects, there will always be some uncertainty in the determined densities; the size of the islands will be slightly overestimated, whereas the depth of the ‘holes’ in between the islands is not fully resolved. Another uncertainty comes from the step edge ‘roughening’, which is also not directly measured. Finally, the available literature data for kinked surfaces is not sufficient to rigorously proof that the corner and fully-kinked step ‘defects’ contribute equally to the {100} and {110}-related CV features. This was an underlying assumption of grouping the site densities as performed in Fig. 3.4D. Thus, although the current values of our prefactors are in the right range, they should be interpreted with some care.

## 3.4 Conclusions

In this chapter, we have shown that the complex evolution of the electrochemical fingerprint of a Pt(111) surface upon ORCs can directly be explained from the (evolution of the) densities of various surface sites. Thus, our analysis provides direct evidence for the electrochemical response of individual ‘defect’ sites. It provides a solid background for the interpretation of the electrochemical response not only of rough (e.g. polycrystalline) platinum surfaces in general, but also for nanoparticles, and even regularly stepped single crystal surfaces. The atomic description of the roughening process also leads to a better understanding of the stability of specific atomic geometries under potential cycling conditions. These insights form valuable input for the further development of platinum electrocatalysts that exhibit both a high activity and a long lifetime.

## References

1. Bard, A. J. & Faulkner, L. R. *Electrochemical methods : fundamentals and applications* 833 (Wiley, 2001).
2. Schmickler, W. and Santos, E. *Interfacial electrochemistry* 272 (Springer-Verlag Berlin Heidelberg, 2010).
3. Santos, E. and Schmickler, W. *Catalysis in Electrochemistry: From Fundamental Aspects to Strategies for Fuel Cell Development* 516 (John Wiley & Sons, Inc., 2011).
4. Gómez-Marín, A. M. & Feliu, J. M. Pt(111) surface disorder kinetics in perchloric acid solutions and the influence of specific anion adsorption. *Electrochim. Acta* **82**, 558–569 (2012).
5. Björling, A., Ahlberg, E. & Feliu, J. M. Kinetics of surface modification induced by submonolayer electrochemical oxygen adsorption on Pt(1 1 1). *Electrochem. commun.* **12**, 359–361 (2010).
6. Björling, A. & Feliu, J. M. Electrochemical surface reordering of Pt(111): A quantification of the place-exchange process. *J. Electroanal. Chem.* **662**, 17–24 (2011).
7. Wagner, F. T. & Ross, P. N. LEED spot profile analysis of the structure of electrochemically treated Pt(100) and Pt(111) surfaces. *Surf. Sci.* **160**, 305–330 (1985).
8. Aberdam, D., Durand, R., Faure, R. & El-Omar, F. Structural changes of a Pt(111) electrode induced by electrosorption of oxygen in acidic solutions: a coupled voltammetry, LEED and AES study. *Surf. Sci.* **171**, 303–330 (1986).
9. You, H. & Nagy, Z. Oxidation-reduction-induced roughening of platinum (111) surface. *Phys. B Condens. Matter* **198**, 187–194 (1994).
10. You, H., Zurawski, D. J., Nagy, Z. & Yonco, R. M. In-situ x-ray reflectivity study of incipient oxidation of Pt(111) surface in electrolyte solutions. *J. Chem. Phys.* **100**, 4699 (1994).
11. Nagy, Z. & You, H. Applications of surface X-ray scattering to electrochemistry problems. *Electrochim. Acta* **47**, 3037–3055 (2002).
12. Liu, Y., Barbour, A., Komanicky, V. & You, H. X-ray Crystal Truncation Rod Studies of Surface Oxidation and Reduction on Pt(111). *J. Phys. Chem. C* **120**, 16174–16178 (2016).
13. Goryachev, A. *et al.* Synchrotron based operando surface X-ray scattering study towards structure-activity relationships of model electrocatalysts. *ChemistrySelect* **1**, 1104–1108 (2016).
14. Drnec, J. *et al.* Initial stages of Pt(111) electrooxidation: dynamic and structural studies by surface X-ray diffraction. *Electrochim. Acta* **224**, 220–227 (2017).
15. Ruge, M. *et al.* Structural Reorganisation of Pt(111) Electrodes by Electrochemical Oxidation and Reduction. *J. Am. Chem. Soc.* **139**, 4532–4539 (2017).

16. Ruge, M. *et al.* Electrochemical Oxidation of Smooth and Nanoscale Rough Pt(111): An In Situ Surface X-ray Scattering Study. *J. Electrochem. Soc.* **164**, H608–H614 (2017).
17. Sugawara, S. & Itaya, K. In situ scanning tunnelling microscopy of a platinum {111} surface in aqueous sulphuric acid solution. *J. Chem. Soc. Faraday Trans. 1 Phys. Chem. Condens. Phases* **85**, 1351 (1989).
18. Itaya, K. In situ scanning tunneling microscopy of platinum (111) surface with the observation of monatomic steps. *J. Vac. Sci. Technol. A Vacuum, Surfaces, Film.* **8**, 515 (1990).
19. Sashikata, K., Furuya, N. & Itaya, K. In situ electrochemical scanning tunneling microscopy of single-crystal surfaces of Pt(111), Rh(111), and Pd(111) in aqueous sulfuric acid solution. *J. Vac. Sci. Technol. B Microelectron. Nanom. Struct.* **9**, 457 (1991).
20. Breuer, N., Funtikov, A., Stimming, U. & Vogel, R. In situ electrochemical STM imaging of roughened gold and platinum electrode surfaces. *Surf. Sci.* **335**, 145–154 (1995).
21. Furuya, N. & Shibata, M. Structural changes at various Pt single crystal surfaces with potential cycles in acidic and alkaline solutions. *J. Electroanal. Chem.* **467**, 85–91 (1999).
22. Löffler, T., Bussar, R., Xiao, X., Ernst, S. & Baltruschat, H. The adsorption of ethene on vicinally stepped electrode surfaces and the effect of temperature. *J. Electroanal. Chem.* **629**, 1–14 (2009).
23. Wakisaka, M., Asizawa, S., Uchida, H. & Watanabe, M. In situ STM observation of morphological changes of the Pt(111) electrode surface during potential cycling in 10 mM HF solution. *Phys. Chem. Chem. Phys.* **12**, 4184–4190 (2010).
24. Solla-Gullón, J., Rodríguez, P., Herrero, E., Aldaz, A. & Feliu, J. M. Surface characterization of platinum electrodes. *Phys. Chem. Chem. Phys.* **10**, 1359–1373 (2008).
25. Vidal-Iglesias, F. J., Arán-Ais, R. M., Solla-Gullón, J., Herrero, E. & Feliu, J. M. Electrochemical characterization of shape-controlled Pt nanoparticles in different supporting electrolytes. *ACS Catalysis* **2**, 901–910 (2012).
26. McCrum, I. T. & Janik, M. J. Deconvoluting Cyclic Voltammograms To Accurately Calculate Pt Electrochemically Active Surface Area. *J. Phys. Chem. C* **121**, 6237–6245 (2017).
27. Arán-Ais, R. M., Solla-Gullón, J., Herrero, E. & Feliu, J. M. On the quality and stability of preferentially oriented (100) Pt nanoparticles: An electrochemical insight. *J. Electroanal. Chem.* **808**, 433–438 (2018).
28. García-Aráez, N., Climent, V. & Feliu, J. M. Potential-dependent water orientation on Pt(1 1 1) stepped surfaces from laser-pulsed experiments. *Electrochim. Acta* **54**, 966–977 (2009).
29. Furuya, N. & Koide, S. Hydrogen adsorption on platinum single-crystal surfaces. *Surf. Sci.* **220**, 18–28 (1989).
30. Domke, K., Herrero, E., Rodes, A. & Feliu, J. M. Determination of the potentials of zero total charge of Pt(100) stepped surfaces in the [011] zone. Effect of the step density and anion adsorption. *J. Electroanal. Chem.* **552**, 115–128 (2003).
31. Gómez, R. & Clavilier, J. Electrochemical behaviour of platinum surfaces containing (110) sites and the problem of the third oxidation peak. *J. Electroanal. Chem.* **354**, 189–208 (1993).
32. Diaz-Morales, O., Hersbach, T. J. P., Badan, C., Garcia, A. C. & Koper, M. T. M. Hydrogen adsorption on nano-structured platinum electrodes. *Faraday Discuss.* (2018).
33. Jacobse, L., Huang, Y. F., Koper, M. T. M. & Rost, M. J. Correlation of surface site formation to nanoisland growth in the electrochemical roughening of Pt(111). *Nature Materials* **17**, 277–282 (2018).
34. Sekerka, R. F. Equilibrium and growth shapes of crystals: How do they differ and why should we care? *Cryst. Res. Technol.* **40**, 291–306 (2005).
35. Schulze Icking-Konert, G., Giesen, M. & Ibach, H. Novel method for the experimental determination of step energies. *Phys. Rev. Lett.* **83**, 3880–3883 (1999).
36. Ibach, H. *Physics of Surfaces and Interfaces* 646 (Springer, 2006).
37. Rodes, A. & Clavilier, J. Electrochemical study of step reconstruction on platinum surfaces belonging to the [011] zone between Pt(311) and Pt(111). *J. Electroanal. Chem.* **344**, 269–288 (1993).
38. McCrum, I. T., Hickner, M. A. & Janik, M. J. First-Principles Calculation of Pt Surface Energies in an Electrochemical Environment: Thermodynamic Driving Forces for Surface Faceting and Nanoparticle Reconstruction. *Langmuir* **33**, 7043–7052 (2017).

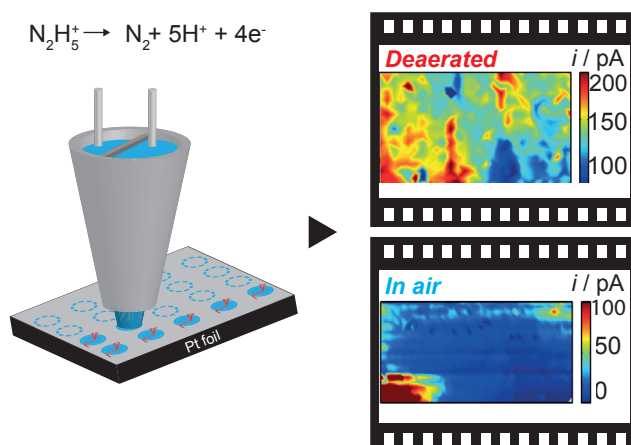
39. Walter, A. L. *et al.* X-ray photoemission analysis of clean and carbon monoxide-chemisorbed Pt(111) stepped surfaces using a curved crystal. *Nat. Commun.* **6**, 8903 (2015).
40. Clavilier, J., Armand, D., Sun, S. & Petit, M. Electrochemical adsorption behaviour of platinum stepped surfaces in sulphuric acid solutions. *J. Electroanal. Chem.* **205**, 267–277 (1986).
41. Topalov, A. A. *et al.* Dissolution of platinum: Limits for the deployment of electrochemical energy conversion? *Angew. Chem. Int. Ed.* **51**, 12613–12615 (2012).
42. Lopes, P. P. *et al.* Relationships between atomic level surface structure and stability/activity of platinum surface atoms in aqueous environments. *ACS Catal.* **6**, 2536–2544 (2016).
43. Sugawara, Y., Sasaki, M., Muto, I. & Hara, N. Dissolution of Platinum Single Crystal Surfaces under Potential Cycling in Sulfuric Acid Solution. *ECS Trans.* **64**, 81–87 (2014).
44. Rost, M. J., Jacobse, L. & Koper, M. T. M. The Dualism between Adatom- and Vacancy-based Single Crystal Growth Models (to be submitted).
45. Bott, M., Hohage, M., Michely, T. & Comsa, G. Pt(111) reconstruction induced by enhanced Pt gas-phase chemical potential. *Phys. Rev. Lett.* **70**, 1489–1492 (1993).
46. Hohage, M., Michely, T. & Comsa, G. Pt(111) network reconstruction: structure, growth and decay. *Surf. Sci.* **337**, 249–267 (1995).
47. Michely, T., Hohage, M., Esch, S. & Comsa, G. The effect of surface reconstruction on the growth mode in homoepitaxy. *Surf. Sci.* **349**, L89–L94 (1996).
48. Wang, S. C. & Ehrlich, G. Structure, stability, and surface diffusion of clusters: Irx on Ir(111). *Surf. Sci.* **239**, 301–332 (1990).
49. Clavilier, J., El Achi, K. & Rodes, A. In situ characterization of the Pt(S)-[n(111) x (111)] electrode surfaces using electroadsorbed hydrogen for probing terrace and step sites. *J. Electroanal. Chem.* **272**, 253–261 (1989).
50. Rodes, A., El Achi, K., Zamakhchari, M. A. & Clavilier, J. Hydrogen probing of step and terrace sites on Pt(S)-[n(111) x (100)] electrodes. *J. Electroanal. Chem.* **284**, 245–253 (1990).
51. Clavilier, J. & Rodes, A. Electrochemical Detection and Characterization at Pt(N,N,N-2) Oriented Electrodes of Multiatomic Step Formation Induced by Quenching at High-Temperatures. *J. Electroanal. Chem.* **348**, 247–264 (1993).
52. McCrum, I. T. & Janik, M. J. pH and Alkali Cation Effects on the Pt Cyclic Voltammogram Explained Using Density Functional Theory. *J. Phys. Chem. C* **120**, 457–471 (2016).
53. Chen, X., McCrum, I. T., Schwarz, K. A., Janik, M. J. & Koper, M. T. Co-adsorption of Cations as the Cause of the Apparent pH Dependence of Hydrogen Adsorption on a Stepped Platinum Single-Crystal Electrode. *Angew. Chem. Int. Ed.* **56**, 15025–15029 (2017).
54. Van Der Niet, M. J., Garcia-Araez, N., Hernández, J., Feliu, J. M. & Koper, M. T. Water dissociation on well-defined platinum surfaces: The electrochemical perspective. *Catal. Today* **202**, 105–113 (2013).



## 4

## Voltammetric scanning electrochemical cell microscopy: dynamic imaging of hydrazine oxidation on platinum electrodes

*Electrochemical imaging is of interest for visualizing electrochemical processes at interfaces and provides valuable information about the associated kinetics, mass transport and localized activity. Typically, such experiments are performed at constant sample potentials, whereas ‘conventional’ electrochemical experiments are mostly performed under potentiodynamic conditions. Here, we describe a combination of ‘hopping mode’ scanning electrochemical cell microscopy (SECCM) and cyclic voltammetry (CV), which enable dynamic imaging with high spatial resolution. Supporting techniques allow for a correlation between local (electrochemical) reactivity of platinum towards hydrazine oxidation and the orientation of the grains in the polycrystalline sample. Furthermore we demonstrate that this reactivity is dramatically influenced by the presence of O<sub>2</sub> under ambient conditions.*



This chapter is based on Chen, C.H., Jacobse, L., McKelvey, K., Lai, S.C.S., Koper, M.T.M., & Unwin, P.R. *Anal. Chem.* **87**, 5782–5789 (2015).

Dynamic electrochemical imaging was first reported by Wipf<sup>1,2</sup> and Schuhmann<sup>3</sup> by combining scanning electrochemical microscopy (SECM) with time-dependent techniques, such as cyclic voltammetry (CV) and potential pulse methods. However, this strategy has not been widely adopted and has also not been used to gain information on heterogeneous electrode surface activity, having employed rather large probe electrodes. Our group has been particularly interested in developing SECCM as a new way to reveal electrode surface activity, as demonstrated by a number of applications.<sup>4–8</sup> Recently, we have adopted a pseudo-single-crystal approach, which combines SECCM and electron backscatter diffraction (EBSD), to study structure–activity relationships at polycrystalline Pt, which comprises high-index Pt facets and grain boundaries.<sup>9,10</sup> However, like other electrochemical imaging approaches<sup>11–13</sup>, SECCM has also been limited to imaging experiments at fixed potentials. Using voltammetric SECCM imaging, a full CV is recorded at a number of locations (pixels) on the substrate, which are arranged in a (rectangular) grid. A wealth of information can be obtained from these measurements that can then be visualized in different ways (e.g., equipotential maps or spatially resolved CVs).

Here, we focus on spatially resolved studies of the electrocatalytic oxidation of hydrazine on a polycrystalline Pt electrode, and compare these results to those obtained on traditional macro- and microscale electrodes. Hydrazine ( $\text{N}_2\text{H}_4$ ) is of practical interest due to its wide application in the fields of electroanalysis and electrocatalysis. Liquid hydrazine is easily transferred and its oxidation offers relatively high power density with carbon-free products, making it a promising fuel for low temperature fuel cells.<sup>14–16</sup> Hydrazine is also important in the pharmaceutical industry, as a common starting material in the synthesis of many pharmaceutical compounds.<sup>17,18</sup> However, it is often a key impurity in pharmaceutical products, and its high toxicity has led to the development of (electrochemical) hydrazine sensors.<sup>19–21</sup> Voltammetric and amperometric hydrazine analysis is usually performed in air, and the role of oxygen in hydrazine detection is rarely taken into account.<sup>22</sup> This is an important consideration, because hydrazine can (catalytically) reduce oxygen on various surfaces, a process that is exploited for corrosion protection.<sup>23–26</sup> Thus, the faradaic response for hydrazine electro-oxidation (especially at trace levels) might be expected to change in the presence of  $\text{O}_2$  in a manner that depends on the electrode structure, as we consider herein.

Pt and Pt-based electrodes are relatively active for hydrazine electro-oxidation, and the mechanism and kinetics of hydrazine oxidation on Pt have received ample attention.<sup>27–29</sup> The overall reaction oxidizes hydrazine to molecular nitrogen and depends on the pH of the solution:



Various possible intermediates and (pH-dependent) reaction pathways have been proposed. In general, no oxygen-containing compounds are detected by online electrochemical mass spectrometry (OLEMS)<sup>28</sup> and the N–N bond is found to remain intact through isotopic labeling.<sup>30</sup> As this is a catalytic reaction, the role of surface structure is of interest and has been investigated using Pt single crystal electrodes.<sup>31–33</sup> For Pt in a weakly adsorbing electrolyte (perchloric acid), the reactivity (in terms of peak potential) for the basal planes decreases in the order of Pt(100) > Pt(111) > Pt(110).<sup>32</sup> While single-crystal research provides valuable information for basal planes, less is known about high-index surfaces and grain boundaries, of practical importance in polycrystalline or nanoparticle-based sensors.

In this chapter, we use voltammetric SECCM to study hydrazine oxidation at a polycrystalline platinum electrode in air and in a nitrogen atmosphere. Equipotential images and dynamic movies obtained from pixel-resolved CV measurements allow direct visualization of hydrazine oxidation across Pt surfaces at multiple different potentials and surface orientations. In the absence of oxygen, the structure-dependent reactivity of hydrazine oxidation for high-index surfaces is established. In air, the electrochemical current for hydrazine oxidation is found to decrease dramatically for most Pt facets, with important implications for hydrazine electroanalysis.

## 4.1 Voltammetric SECCM

The setup for voltammetric SECCM is illustrated in Fig. 4.1A. Briefly, a dual barrel pipet with a small opening (in this study  $\pm 1 \mu\text{m}$  diameter) is used to make a series of voltammetric measurements across an area of interest on the Pt sample. The meniscus at the end of the pipet forms an small electrochemical cell at the sample and defines the working electrode area at each pixel. A bias voltage ( $V_1$ , in this study 200 mV or 500 mV) is applied between two Pd–H<sub>2</sub> quasi-reference counter electrodes (QRCEs, one in each barrel) to generate an ion conductance current

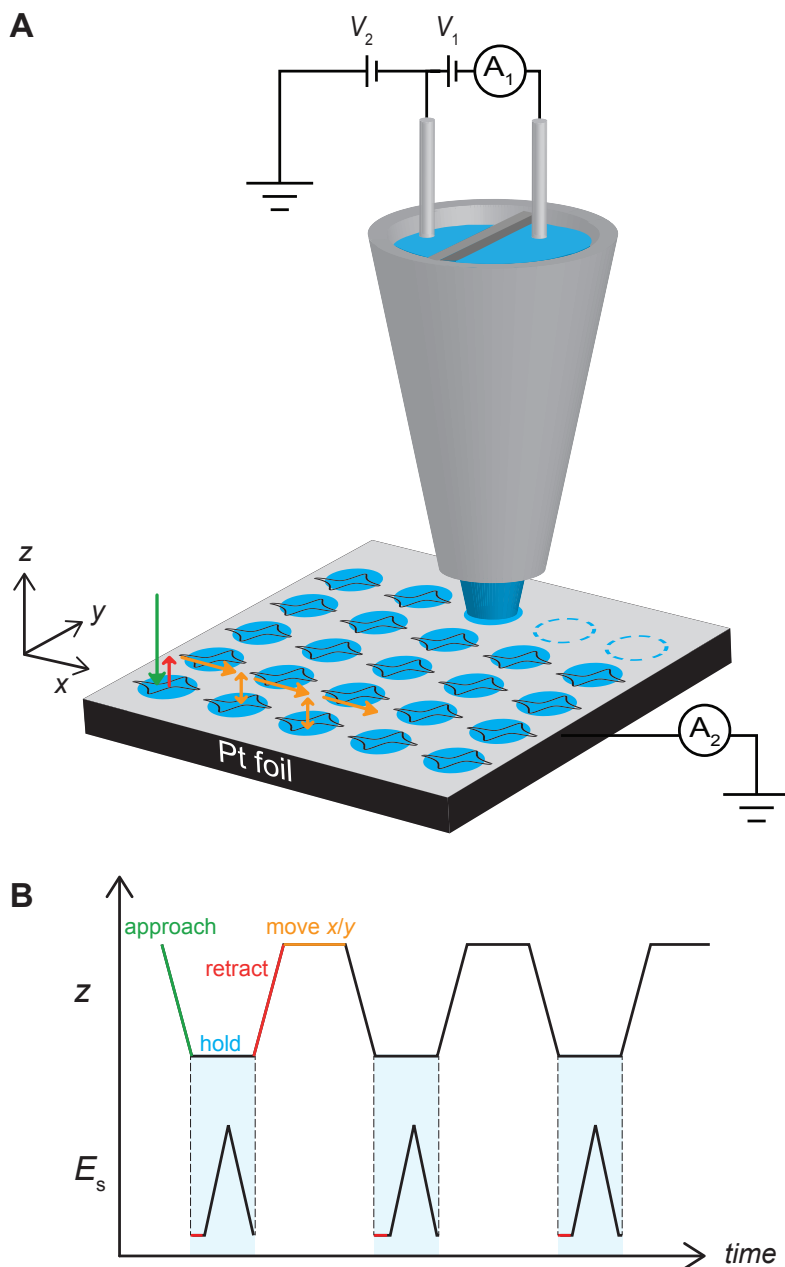


**Fig. 4.1 | Hopping mode voltammetric SECCM:** (A) Schematic overview of the experimental setup.  $V_1$  and  $V_2$  control the bias and sample voltage.  $A_1$  and  $A_2$  measure the bias and sample current, respectively. The blue circles indicate the probed areas of the sample. The arrows indicate the movement of the pipet. (B) Schematic time profiles of the pipet-to-sample separation (top) and the sample potential (bottom).

( $i_{DC}$ ) between the barrels across the liquid meniscus. The working electrode potential ( $E_s$ ) is determined by both  $V_1$  and a voltage ( $V_2$ ) applied to one of the QRCEs,  $E_s = -(V_2 + 0.5 \cdot V_1)$ . Modulation of the z-position of the tip (66 or 266 Hz, 25–50 nm peak amplitude) produces an AC component in the ion conductance current ( $i_{AC}$ ). A constant tip-to-sample distance is maintained by using the magnitude of  $i_{AC}$  as input for the feedback.<sup>4–10</sup>

In previous SECCM and related studies, the sample was scanned by the probe using a continuous scanning<sup>10</sup> (for flat substrates) or approach–hold–withdraw (hopping) mode (for rough substrates and/or dissolution studies),<sup>34,35</sup> while the sample, if a conductor, was held at a constant potential ( $E_s$ ). To obtain potentiodynamic data for a wide potential range in a single experiment, we combine this latter hopping mode SECCM with a potential sweep at each position. As a result, we get a complete, spatially resolved, cyclic voltammogram. Figure 4.1B illustrates the tip-to-sample distance as a function of time during imaging, together with the corresponding applied sample potential. The complete scanning process consists of the following steps: slow approach of the pipet ( $0.5 \mu\text{m}\cdot\text{s}^{-1}$ ); once in meniscus contact, the pipet position and sample potential are held for 1 s to allow the droplet cell to stabilize; a potential sweep ( $0.1 \text{V}\cdot\text{s}^{-1}$ ) to obtain the CV was then applied; quick retraction ( $2.0 \mu\text{m}\cdot\text{s}^{-1}$ ) of the pipet far enough to break the meniscus; and movement in the xy-plane to repeat the process for the next pixel. The retract distance is chosen based on the tip size and the roughness/flatness of the substrate and is typically 1–1.5  $\mu\text{m}$ . For the CV measurement, current data are recorded at least every 1 mV, to produce potentiodynamic movies containing many hundreds of frames. SECCM experiments in deaerated conditions are carried out in an environmental cell, which is placed over the Pt sample and the pipet and is flushed with humidified  $\text{N}_2$  (through a vial containing water) before starting the experiment and during imaging.

The resolution of this mode of SECCM imaging is ultimately not determined by the size of pipet apex, but by the distance in between adjacent pixels. This spacing was chosen such (2–3  $\mu\text{m}$ ) that there was no overlap between each probed area (diameter  $\pm 1 \mu\text{m}$ ). This ensures that a ‘fresh’ surface (i.e., a region of the surface that has not yet been in contact with the electrolyte solution) is encountered for each pixel, such that all CVs recorded in the SECCM imaging are the first CV at that particular position. Another important factor to determine the pixel spacing is the total imaging time which is typically several hours. Obviously, maintaining

stable and clean imaging conditions at such time scales is challenging. A two-dimensional linear interpolation is applied to the SECCM images in this chapter to guide the eye. We argue that this is reasonable, as in most grains the current was fairly uniform across the grain. More information on the data representation and further experimental details are provided in Appendix E.

## 4.2 Hydrazine oxidation at Pt electrodes

To study the electrochemistry of hydrazine and provide a comparison for the SECCM results, CV measurements are carried out at polycrystalline platinum electrodes at different length scales. Typical CVs for hydrazine oxidation recorded on a mm-scale platinum wire, on a 25  $\mu\text{m}$  diameter Pt ultramicroelectrode (UME), and on a polycrystalline Pt foil using a 1  $\mu\text{m}$  diameter SECCM pipet are shown in Fig. 4.2. All CVs are recorded in a deaerated solution of 2 mM  $\text{N}_2\text{H}_4$  in 0.1 M  $\text{HClO}_4$  at 100  $\text{mV}\cdot\text{s}^{-1}$ .

At the macroscopic Pt electrode, hydrazine oxidation in an acidic electrolyte starts just after the hydrogen desorption region and then quickly reaches a peak current at ca. 0.48 V. In the case of the UME, (diffusional) mass transport is much faster than that for the macroelectrode. In competition with the surface kinetics for hydrazine electro-oxidation, this leads to an apparent shift in the onset potential to ca. 0.45 V. A steady-state current is observed at potentials above 0.80 V. Similar with CVs reported in literature, hydrazine oxidation is a reasonably facile process at both the macro- and the microscale, leading to mass transport limited reactivity at intermediate overpotentials.<sup>29,36</sup>

Figure 4.2C shows a typical CV for hydrazine oxidation at a platinum foil recorded in the SECCM setup. The oxidation of hydrazine has a similar onset potential as on the UME, but there is a small transient peak in the current at 0.80 V before a quasi-steady state at more anodic potentials. Importantly, Fig. 4.2C shows no features due to oxygen reduction (which would be manifested in observable reduction currents well above the present cathodic onset of  $\pm 0.1$  V). This confirms the performance of the environmental cell, as the fast diffusion of  $\text{O}_2$  from the surroundings across the meniscus to the surface would lead to a noticeable current.<sup>10</sup> Furthermore, as we will show below, the presence of oxygen leads to significantly distorted features in the voltammetric profile for the oxidation of hydrazine. The diffusion coefficient ( $D$ )\* calculated from the UME experiments

---

\*  $i_{lim} = 4nFDcr$ ,<sup>37</sup> where  $n$  is the number of electrons transferred per hydrazine molecule ( $n = 4$ ),  $F$  is the Faraday constant,  $c$  is the bulk hydrazine concentration, and  $r$  is the UME radius.

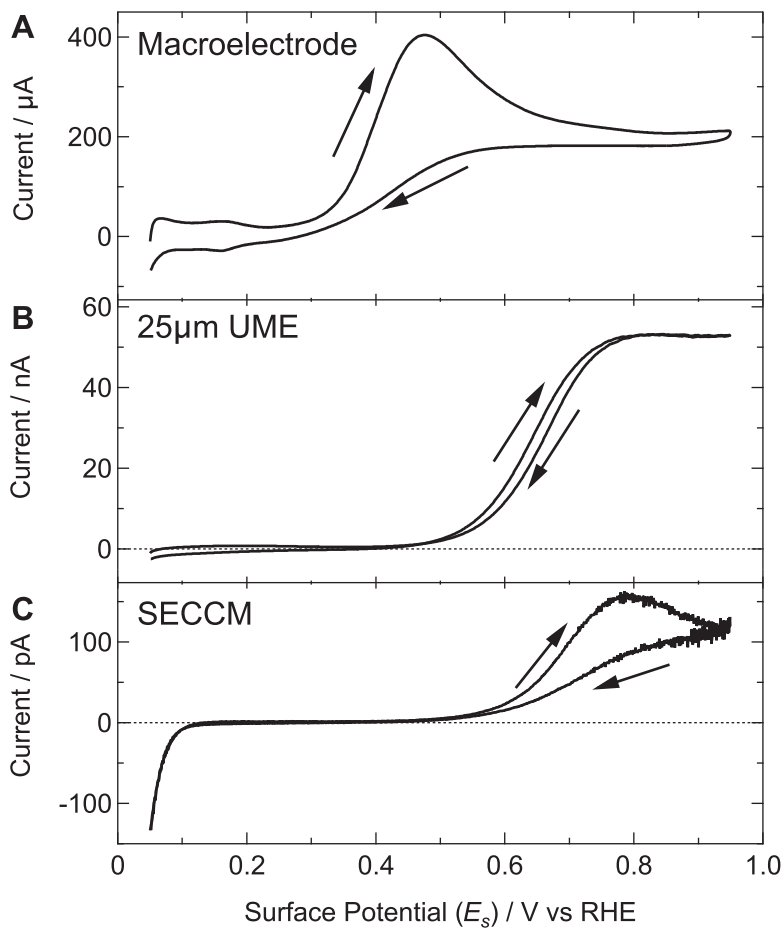


**Fig. 4.2 | Hydrazine oxidation at Pt electrodes:** Typical CVs of hydrazine oxidation at (A) a Pt wire, (B) a 25  $\mu\text{m}$  diameter Pt UME, and (C) a polycrystalline Pt foil in a SECCM setup. Note the different current scales. In all cases the CVs are recorded in deaerated electrolyte solutions containing 2 mM  $\text{N}_2\text{H}_4$  in 0.1 M  $\text{HClO}_4$ . The sweep rates are 100  $\text{mV}\cdot\text{s}^{-1}$ .

is  $1.4 \cdot 10^{-5} \text{ cm}^2 \cdot \text{s}^{-1}$  and is consistent with values reported in the literature.<sup>38,39</sup> In SECCM, the steady-state diffusion-limited current,  $i_{lim}$ , beyond the peak is 100 pA. The calculated mean mass transport coefficient,  $kt$  ( $kt = i_{lim}/nFAc$ , where  $A$  is the meniscus footprint area), in SECCM is  $1.65 \cdot 10^{-2} \text{ cm} \cdot \text{s}^{-1}$ . This is about 5% of that for an inlaid disk UME ( $kt = 4D/\pi r$ ) of the same size, which is within the typical range reported for a micrometer-sized SECCM pipet,<sup>6</sup> and similar to that of the 25  $\mu\text{m}$  diameter UME. That the SECCM voltammogram shows a slight transient response compared to the UME (cf. Fig. 4.2B and C) is because of the very different current distribution in SECCM with respect to a bulk solution. For  $\text{N}_2\text{H}_5^+$ , which is the predominant species herein, there is a large difference in mass transport rate down the two channels of the theta pipet in SECCM.<sup>6</sup> Further, note that some of the differences between the CVs in Fig. 4.2 will be due to the different electrodes used, and methods of preparation, because, as we show herein, hydrazine oxidation is very surface sensitive.

In recent work, a significant ‘activation’ of a Pt UME after scanning toward high oxidative potentials was reported. This ‘activation’ was attributed to the formation of catalytically active residual surface oxides in sequential voltammetric scans.<sup>36</sup> Several SECCM CVs were recorded in this study where the potential was scanned up to 1.45 V (see Appendix E). While there are small changes in the voltammetric signature, the responses were generally similar to the ‘stabilized’ CV reported<sup>36</sup> without the need for any initial activating scan. It should be kept in mind, however, that our surface preparation is an oxidative process (flame-annealing), which could introduce such residual oxides. Nonetheless, to avoid possible complications due to the (more extensive) formation and reduction of Pt oxides, all the CVs in SECCM imaging experiments are recorded from 0.05 to 0.95 V, focusing on the main response.

### 4.3 Voltammetric SECCM imaging

Figure 4.3A shows an EBSD image of a typical probed area of polycrystalline platinum foil. This plot shows the grain orientation of the sample in the  $41 \times 86 \mu\text{m}^2$  area (with a pixel spacing of 3  $\mu\text{m}$ ) of which the electrochemical activity is imaged in the SECCM experiments.\* We will focus on the voltammetry of the four numbered grains as they present the limiting cases of the orientations present. EBSD

---

\* At first sight, this resolution of  $14 \times 29$  pixels might seem rather low. However, one should realize that, by scanning the potential in such a wide range, the total imaging time already adds up to  $\sim 3$  hours.

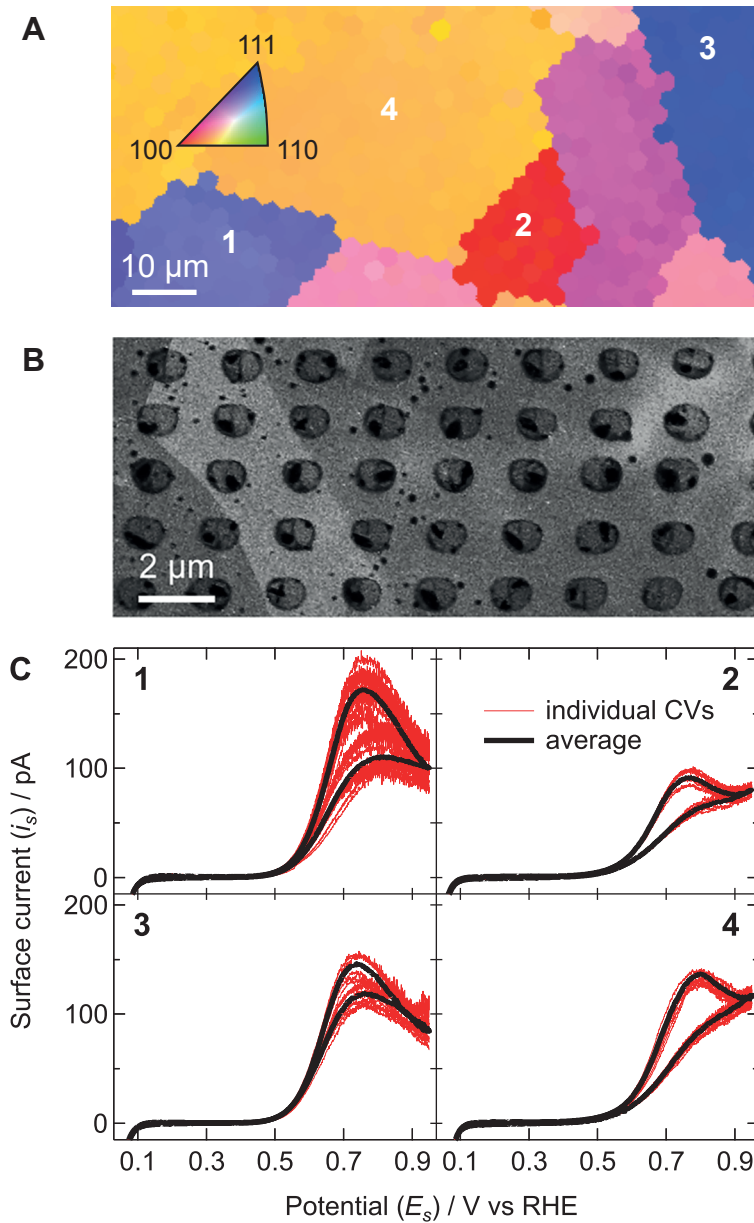


**Fig. 4.3 | Structure-activity relationships:** (A) EBSD image of the Pt foil used in the SECCM imaging experiments. The grain orientations are indicated in the triangle. (B) A typical SEM image of a part of a scanned area after SECCM imaging, showing the electrolyte residues on the sample. (C) Individual CVs (red, 7–10 for each grain) and grain-averaged CVs (black) for the number grains in (A).

results show that all the grains are high-index surfaces, but grain 1 and 3 have orientations approaching {111}, while grain 2 has an orientation approaching {100}. Grain 4 lies in between {100} and {110}.

Optical microscopy and SEM images after SECCM imaging show droplet residues on the surface due to the quick breaking of the meniscus during probe retraction. Figure 4.3B is a typical zoomed-in SEM image after an SECCM measurement. These droplet residues are fairly consistent in shape and size at the different grains, confirming the stability and reproducibility of the technique and the absence of a significant dependence of droplet wetting on the grain orientation. Additionally, the residues help to determine the exact imaged area and droplet size (meniscus footprint) after SECCM imaging (see also Appendix E).

By combining the results from SECCM, SEM, and EBSD, the position of each individual CV can be determined. Figure 4.3C shows CVs from 7 to 10 pixels obtained on each of the four numbered grains. On top of the individual CVs, an averaged CV is plotted for each grain to show the representative CV feature of that area. It is clear that the variation within a particular grain is fairly small, particularly for grain 2 and grain 4, but the orientation of the grain has a significant impact on its voltammetric response. This is not due to changes in the meniscus contact area as the footprint is reasonably consistent, as pointed out above, and also shown over a more extensive region in Appendix E. Moreover, also the ion conductance current (see Ref. [40]), which is sensitive to the electrochemical footprint shows no structural dependent features. Although all the grains are high-index surfaces, grains 1 and 3, which have contributions mainly from the {111} orientation, have very similar CVs. Grains 2 and 4, which are mainly {100} oriented, show lower peak currents and higher peak potentials. Furthermore, closer inspection reveals that, on grains 1 and 3, the current after the peak decreases reversibly (increasing again after reversal of the potential sweep direction). This is likely related to the initial stages of surface oxide formation on Pt(111) in perchloric acid, which is highly reversible.<sup>41</sup> In contrast, on grains 2 and 4 (mainly {100} orientation), the current continues to decrease after reversal of the sweep direction, mirroring the irreversibility of surface oxidation on Pt(100).<sup>41</sup> Thus, we believe surface oxidation/reduction kinetics is (one of) the factor(s) determining the shape of the voltammogram. Significantly, this effect would have remained unnoticed in (conventional) fixed-potential imaging, highlighting the considerable strength of voltammetric SECCM. Importantly, these results illustrate that hydrazine oxidation at high-index Pt surfaces is strongly structure dependent.

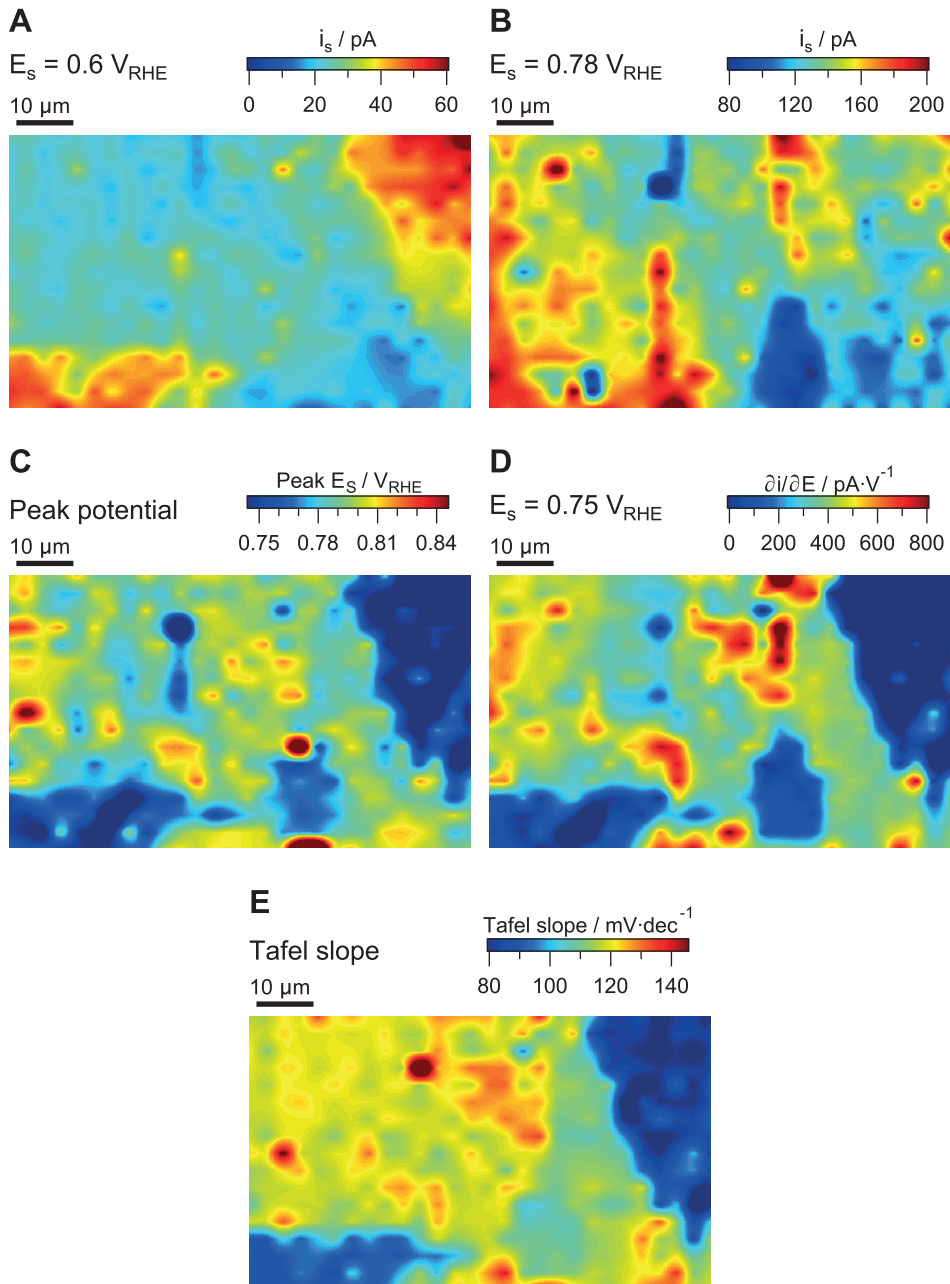


**Fig. 4.4 | Maps of SECCM data:** Various representations of the SECCM data of a single region; (A–B) activity, expressed as substrate current maps for  $E_s=0.60$  and  $0.78 \text{ V}$ ; (C) peak potential; (D)  $\partial i / \partial E_s$  at  $E_s=0.75 \text{ V}$ . Note the different color scales. (E) Tafel slope in  $\text{mV}$  per decade determined using the data from  $0.45 > E_s > 0.65 \text{ V}$ .

In addition to individual and averaged CVs, the spatially resolved reactivity can be visualized through various types of activity maps. For example, as current values were recorded at least every 1 mV during the pixel-resolved CV measurements, we can construct a series of equipotential maps by plotting the sample current ( $i_s$ ) of all pixels at a given potential as a function of spatial position. The full series can then be compiled as a movie as shown in Ref. [40], which illustrates the localized evolution of the surface current during a cyclic potential sweep. In the movie, with increasing potential, the activity of different grains starts to show up, providing a direct view of the electrochemical activity across the surface. Figure 4.4A and 4.4B are two frames of data from the  $i_s$  movie during the forward scan at potentials of 0.60 and 0.78 V respectively. In these figures, the color scales are adjusted to highlight the full current range at each potential. Such equipotential maps are conceptually similar to maps which could have been obtained with fixed potential SECCM imaging, but with our approach these are only 2 maps out of the 1800 maps that can be constructed from the data at different potentials. The chosen potentials for Fig. 4.4A and 4.4B are close to the onset of the oxidation current (Fig. 4.4A,  $E_s=0.60$  V) and the peak potential (Fig. 4.4B,  $E_s=0.78$  V). In Fig. 4.4A, grains 1 and 3 can be recognized as having higher activity, while grain 2 is more easily recognized in Fig. 4.4B.

As evident in Fig. 4.3C, SECCM CVs on this time scale typically show a peak during the oxidative potential sweep, and the potential at which this peak occurs is related semiquantitatively to the driving force required for the reaction. This is shown in Fig. 4.4C, from which it is clear that the peak occurs at lower overpotential, the higher the current in the surface activity maps in Fig. 4.4A and 4.4B. Using another approach, a high order polynomial is fitted through each pixel-resolved CV to calculate  $\partial i/\partial E_s$ , with the result at  $E_s=0.75$  V shown in Fig. 4.4D. This quantity again gives a measure of the ease of reaction, and the result is a map showing the distinct behavior of the different grains. Finally, a Tafel analysis is performed for all four grains, using the potential interval from 0.45 to 0.65 V (at the foot of the wave, where mass transport and concentration polarization can be neglected) and is shown in Fig. 4.4E. For the whole area, the apparent Tafel slope is mainly within the range of 80 to 140 mV per decade. This range is within that of the previously reported Tafel slope values, 82 mV per decade to 110 mV per decade, for polycrystalline Pt electrodes in acidic solution.<sup>29,42</sup> However, our data are showing that the precise slope is very grain-orientation dependent. The average Tafel slopes for grains from 1 to 4 are  $100\pm 12$ ,  $130\pm 2$ ,  $88\pm 3$ , and  $139\pm 3$  mV per decade,

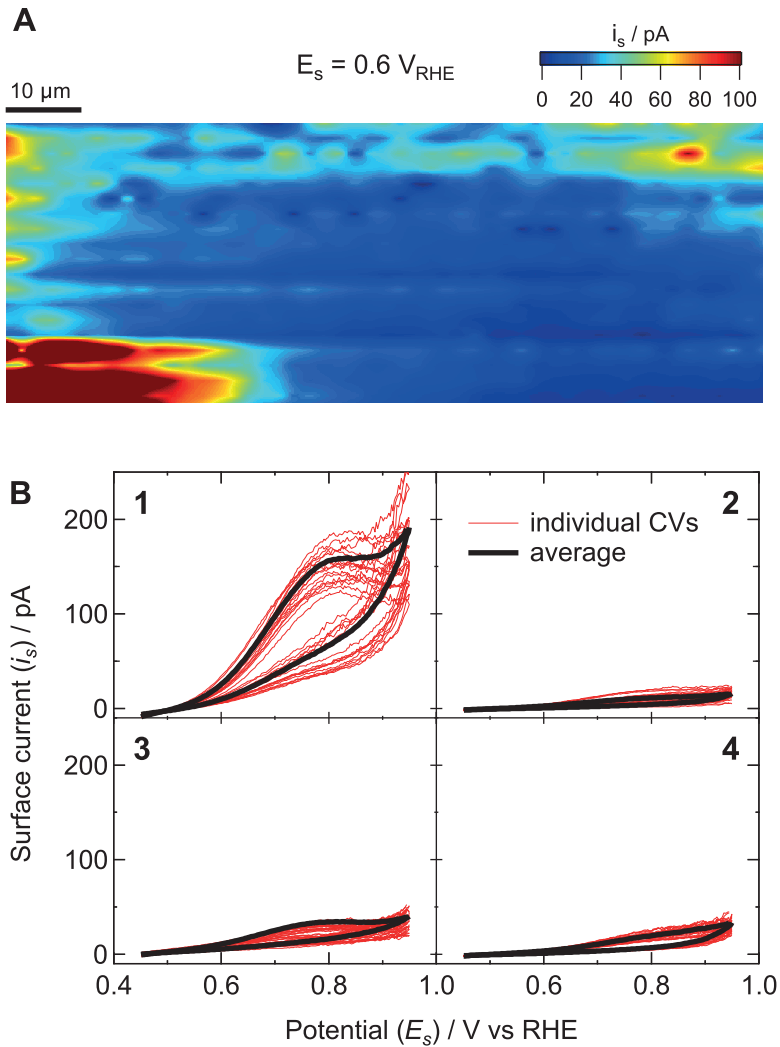


**Fig. 4.5 | Hydrazine oxidation in air:** (A) Equipotential  $i_s$  map of hydrazine oxidation at  $E_s=0.78 \text{ V}$ . (B) Individual (red, 10–20 for each grain) and averaged (black) CVs for different grains. Numbers in (B) correspond to grain areas marked in Fig. 4.3a.

respectively. By comparing Fig. 4.4A–B to 4.4C–E, it is demonstrated through the use of voltammetric SECCM that it becomes possible to visualize/identify differences (especially in the  $\partial i/\partial E_s$  maps) in electrochemical activity which would be invisible using fixed potential imaging.

## 4.4 Hydrazine oxidation in air

Besides the faradaic oxidation of hydrazine, there are also studies reporting catalytic (nonfaradaic) decomposition of hydrazine.<sup>25,43</sup> Although the nonfaradaic oxidation of hydrazine in air is slow at room temperature, it can be accelerated in the presence of catalysts, such as platinum, copper, and manganese.<sup>25,30,43</sup> Recently, we have demonstrated that the three-phase boundary in SECCM<sup>10</sup> provides high mass transport of oxygen, making SECCM is an interesting technique to study the role of  $O_2$  in the total oxidation reaction. Thus, imaging experiments are performed in the same area as shown in Fig.4.3A, after cleaning the surface, but now without using the environmental cell. CVs are recorded every 2  $\mu\text{m}$  between 0.45 and 0.95 V.

Figure 4.5A shows an equipotential  $i_s$  map extracted from the SECCM imaging experiment in air, at 0.78 V. Movies of  $i_s$  and  $i_{DC}$  for the CV measurements are available in Ref. [40]. Compared to Fig. 4.3C, Fig. 4.5A shows that, except for grain 1, the electrochemical activity of all the grains is almost completely suppressed. Similar to the approach in Fig. 4.3C, CVs recorded at grains 1 to 4 at single pixels (red) and the averaged ones (black) are shown in Fig. 4.5B. It is clear that hydrazine oxidation CVs in air exhibit different shapes and much lower current values compared with CVs in the absence of  $O_2$ . Simultaneously, the peak current, when discernible, shifts to higher overpotential.

To further understand the role of oxygen and the cause of the large differences in activity, we perform a blank SECCM experiment in air, using just the supporting electrolyte. The potential is scanned between 0.45 and 1.35 V at a sweep rate of  $0.5 \text{ V}\cdot\text{s}^{-1}$ . Averaged CVs in each of the four grains for all three imaging experiments (hydrazine oxidation in a deaerated solution, hydrazine oxidation in the presence of dissolved oxygen, and blank CVs) are summarized in Fig. 4.6. By comparing the three measurements, it is clear that, generally, the presence of oxygen leads to a decrease in the currents observed for the oxidation of hydrazine. There are two main causes of this effect.

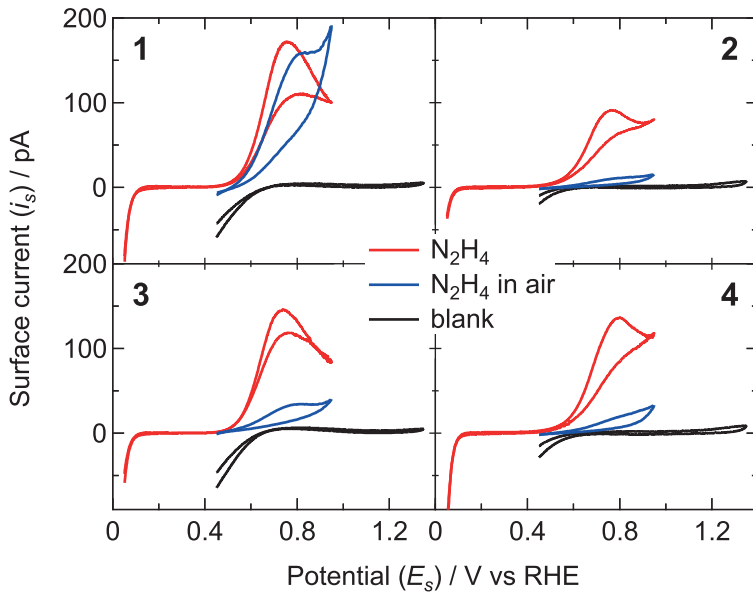
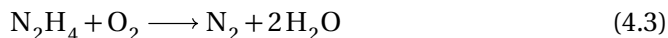


**Fig. 4.6 | The effect of air on the oxidation of hydrazine:** Comparison of  $N_2H_4$  oxidation (red) in deaerated environment,  $N_2H_4$  oxidation in air (blue), and blank (in air, black) averaged CVs for different grain orientations (numbers indicated).

First, it can be seen in the blank CVs that, at potentials below 0.65 V, there is a significant (reduction) current due to the oxygen reduction reaction (ORR), in agreement with our previous findings.<sup>10</sup> Thus, at potentials between 0.45 and 0.65 V, the oxidation of hydrazine (positive current) overlaps with the reduction of oxygen (negative current) in an aerated solution, and the overall observed current in this potential range represents the sum of the two processes. As a result, the apparent current for the oxidation of hydrazine in air in this potential range is much smaller than that of the oxidation of hydrazine in deaerated conditions (and, similarly, the reduction current of oxygen with hydrazine present is smaller (in absolute terms) than that of the reduction of oxygen in the absence of hydrazine). Second, as mentioned above, hydrazine can react with oxygen through the following reaction at a catalyst (such as platinum) surface:



This nonfaradaic (i.e., no ‘current-producing’) reaction consumes hydrazine, thereby lowering the interfacial concentration of hydrazine. In fact, this reaction is most likely exacerbated in our experimental setup, as is the ORR effect mentioned above, due to the enhanced mass transport of oxygen at the three-phase boundary.<sup>10</sup> Consequently, a lower current for the (electrochemical) oxidation of hydrazine is observed compared to a deaerated solution, as the current is directly proportional to the hydrazine concentration.

In fact, we can exploit this second mechanism to obtain the structural dependency (at least in a semiquantitative manner) of the nonfaradaic reaction between oxygen and hydrazine. By using the observed current in the presence of oxygen as a probe for the residual hydrazine concentration (that is, the hydrazine concentration after the nonfaradaic consumption of hydrazine), we can deduce the extent to which the nonfaradaic reaction takes place. Specifically, regions of the sample where there is a small decrease in current (such as grain 1) indicate low activity toward the nonfaradaic reaction, whereas a large decrease (such as grains 2, 3, and 4) represents high activity. Using this approach, we find the activity toward the nonfaradaic reaction of hydrazine and oxygen to follow the following relative order: grain 2 > grain 4 > grain 3 > grain 1. Interestingly, this is the inverse of the electrochemical activity (see Fig. 4.3C), and at least in part, this rationalizes the trend because the faradaic and nonfaradaic processes are in competition. Importantly, these results provide a novel method to probe local structure effects in nonfaradaic catalytic reactions through electrochemical measurements, an avenue we will further explore in the future. There are also clearly implications

for the optimal design of hydrazine voltammetric sensors in an aerated solution.

## 4.5 Conclusions

In this chapter, we have highlighted the considerable power of voltammetric SECCM, which combines SECCM with CV measurements, as a methodology for electrochemical imaging. Compared to traditional fixed potential imaging,<sup>5,8,10,44</sup> this approach has significant attributes. First, as CVs are recorded at every pixel of the scanned area, it is possible to probe local electrochemical currents at multiple potentials (1800 separate potentials in the deaerated hydrazine CVs herein) and thus increase imaging efficiency. Furthermore, as the meniscus breaks and droplet residues are left on the substrate, as the pipet moves to a new position on the substrate for the next measurement, it is possible to determine the exact position and surface area of each pixel. Finally, it allows for potentiodynamic information to be obtained, complementing potentiostatic information from fixed potential imaging, which both have their uses in certain situations (cf. cyclic voltammetry and chronoamperometry).

In this work, using voltammetric SECCM, we studied hydrazine oxidation at high-index Pt surfaces in air and in a deaerated environment. We found the CV characteristics of hydrazine oxidation at the Pt electrode to be strongly surface structure dependent. The reactivity of hydrazine at different surfaces can be compared from equipotential maps and dynamic movies. For the grain orientations studied here, grains having more {111} features show higher activity than grains having more {100} features. This might appear to counter studies with single-crystal electrodes, but it should be noted that the studies herein are on high-index and high-defect facets, highlighting the importance of such features in the electrocatalytic oxidation of hydrazine oxidation on practical surfaces.

Significant changes in hydrazine oxidation activity were observed in air, where oxygen transfers through the three-phase boundary of the SECCM with high rates. We found the presence of oxygen strongly decreased the detected electrochemical current for hydrazine oxidation at most of the Pt grains. The variation in activity between different grains was also much more pronounced than in the absence of air. We ascribe these changes to the overlap between the potentials for hydrazine oxidation and ORR, as well as to the nonfaradaic decomposition of hydrazine with oxygen at certain Pt facets. These results emphasize the importance of considering oxygen in the voltammetric detection of hydrazine, which could greatly affect the response of hydrazine sensors in a manner dependent on the Pt substrate used.

## References

1. Díaz-Ballote, L., Alpuche-Aviles, M. & Wipf, D. O. Fast-scan cyclic voltammetry–scanning electrochemical microscopy. *J. Electroanal. Chem.* **604**, 17–25 (2007).
2. Schrock, D. S., Wipf, D. O. & Baur, J. E. Feedback Effects in Combined Fast-Scan Cyclic Microscopy. *Anal. Chem.* **79**, 4931–4941 (2007).
3. Nebel, M., Grütze, S., Diab, N., Schulte, A. & Schuhmann, W. Microelectrochemical visualization of oxygen consumption of single living cells. *Faraday Discuss.* **164**, 19 (2013).
4. Ebejer, N., Schnippering, M., Colburn, A. W., Edwards, M. A. & Unwin, P. R. Localized high resolution electrochemistry and multifunctional imaging: Scanning electrochemical cell microscopy. *Anal. Chem.* **82**, 9141–9145 (2010).
5. Ebejer, N. *et al.* Scanning Electrochemical Cell Microscopy: A Versatile Technique for Nanoscale Electrochemistry and Functional Imaging. *Annu. Rev. Anal. Chem.* **6**, 329–351 (2013).
6. Snowden, M. E. *et al.* Scanning electrochemical cell microscopy: Theory and experiment for quantitative high resolution spatially-resolved voltammetry and simultaneous ion-conductance measurements. *Anal. Chem.* **84**, 2483–2491 (2012).
7. Lai, S. C. S., Patel, A. N., McKelvey, K. & Unwin, P. R. Definitive evidence for fast electron transfer at pristine basal plane graphite from high-resolution electrochemical imaging. *Angew. Chem. Int. Ed.* **51**, 5405–5408 (2012).
8. Güell, A. G., Ebejer, N., Snowden, M. E., MacPherson, J. V. & Unwin, P. R. Structural correlations in heterogeneous electron transfer at monolayer and multilayer graphene electrodes. *J. Am. Chem. Soc.* **134**, 7258–7261 (2012).
9. Aaronson, B. D. *et al.* Pseudo-single-crystal electrochemistry on polycrystalline electrodes: Visualizing activity at grains and grain boundaries on platinum for the  $\text{Fe}_2^+/\text{Fe}_3^+$  redox reaction. *J. Am. Chem. Soc.* **135**, 3873–3880 (2013).
10. Chen, C.-H., Meadows, K. E., Cuharuc, A., Lai, S. C. S. & Unwin, P. R. High resolution mapping of oxygen reduction reaction kinetics at polycrystalline platinum electrodes. *Phys. Chem. Chem. Phys.* **16**, 18545 (2014).
11. Bard, A. J. & Faulkner, L. R. *Electrochemical methods : fundamentals and applications* 833 (Wiley, 2001).
12. Bard, A. J., Fan, F. R. F., Kwak, J. & Lev, O. Scanning Electrochemical Microscopy. Introduction and Principles. *Anal. Chem.* **61**, 132–138 (1989).
13. Amemiya, S., Bard, A. J., Fan, F.-R. F., Mirkin, M. V. & Unwin, P. R. Scanning Electrochemical Microscopy. *Annu. Rev. Anal. Chem.* **1**, 95–131 (2008).
14. Serov, A. & Kwak, C. Direct hydrazine fuel cells: A review. *Appl. Catal., B* **98**, 1–9 (2010).
15. Yamada, K. *et al.* Investigation of PEM type direct hydrazine fuel cell. *J. Power Sources* **115**, 236–242 (2003).
16. Rees, N. V. & Compton, R. G. Carbon-free energy: a review of ammonia- and hydrazine-based electrochemical fuel cells. *Energy Environ. Sci.* **4**, 1255 (2011).
17. Elder, D. P., Snodin, D. & Teasdale, A. Control and analysis of hydrazine, hydrazides and hydrazones-Genotoxic impurities in active pharmaceutical ingredients (APIs) and drug products. *J. Pharm. Biomed. Anal.* **54**, 900–910 (2011).
18. Liu, D. Q., Sun, M. & Kord, A. S. Recent advances in trace analysis of pharmaceutical genotoxic impurities. *J. Pharm. Biomed. Anal.* **51**, 999–1014 (2010).
19. Metters, J. P., Tan, F., Kadara, R. O. & Banks, C. E. Platinum screen printed electrodes for the electroanalytical sensing of hydrazine and hydrogen peroxide. *Anal. Methods* **4**, 1272 (2012).
20. Liu, J., Li, Y., Jiang, J. & Huang, X. C@ZnO nanorod array-based hydrazine electrochemical sensor with improved sensitivity and stability. *Dalton Trans.* **39**, 8693 (2010).
21. Chakraborty, S. & Raj, C. R. Carbon nanotube supported platinum nanoparticles for the voltammetric sensing of hydrazine. *Sens. Actuators, B* **147**, 222–227 (2010).
22. Hu, G., Zhou, Z., Guo, Y., Hou, H. & Shao, S. Electrospun rhodium nanoparticle-loaded carbon nanofibers for highly selective amperometric sensing of hydrazine. *Electrochem. Commun.* **12**, 422–426 (2010).

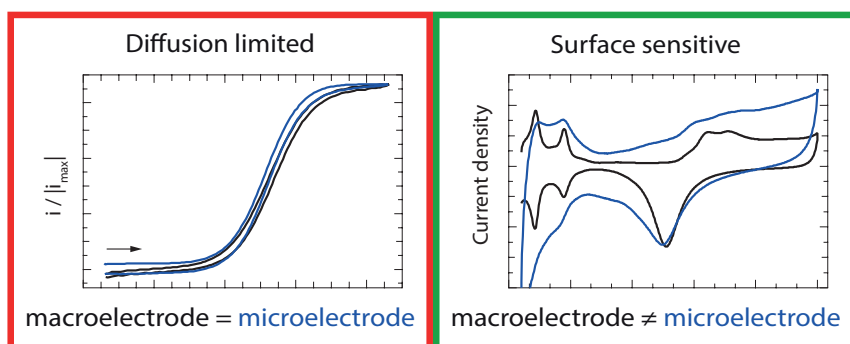
23. Moussa, M. N. H., Taha, F. I. M., Gouda, M. M. A. & Singab, G. M. The effect of some hydrazine derivatives on the corrosion of Al in HCl solution. *Corros. Sci.* **16**, 379–385 (1976).
24. Andries, V. & Couturier, D. Reduction of dissolved oxygen in water: Hydrazine and its organic substitutes. *Mater. Performance* **39**, 58–61 (2000).
25. Cuy, E. J. & Bray, W. C. The oxidation of hydrazine. II. The effect of oxygen on the decomposition of hydrazine. The reactions with ferricyanide in alkaline solution, and dichromate in acid solution. *J. Am. Chem. Soc.* **46**, 1786–1795 (1924).
26. Moon, J., Park, K., Kim, J. & Seo, G. The reduction reaction of dissolved oxygen in water by hydrazine over platinum catalyst supported on activated carbon fiber. *Appl. Catal., A* **184**, 41–48 (1999).
27. Bard, A. J. Chronopotentiometric Oxidation of Hydrazine at a Platinum Electrode. *Anal. Chem.* **35**, 1602–1607 (1963).
28. Rosca, V. & Koper, M. T. M. Electrocatalytic oxidation of hydrazine on platinum electrodes in alkaline solutions. *Electrochim. Acta* **53**, 5199–5205 (2008).
29. García, M. D., Marcos, M. L. & Velasco, J. G. On the mechanism of electrooxidation of hydrazine on platinum electrodes in acidic solutions. *Electroanalysis* **8**, 267–273 (1996).
30. Arnolds, K., Heitbaum, J. & Vielstich, W. Investigations on the Rupture of the N-N-Bond within the Anodic Oxidation and Catalytic Decomposition of Hydrazine. *Z. Naturforsch. A: Phys., Phys. Chem., Kosmophys.* **29**, 359–362 (1974).
31. Nishihara, C. *et al.* Behavior of hydrazine and its effects on the adsorption of hydrogen at Pt(322) and Pt(111) electrodes in sulfuric acid solutions. *J. Electroanal. Chem.* **338**, 299–316 (1992).
32. Álvarez-Ruiz, B., Gómez, R., Orts, J. M. & Feliu, J. M. Role of the Metal and Surface Structure in the Electro-oxidation of Hydrazine in Acidic Media. *J. Electrochem. Soc.* **149**, D35 (2002).
33. Gómez, R. & Clavilier, J. Electrochemical behaviour of platinum surfaces containing (110) sites and the problem of the third oxidation peak. *J. Electroanal. Chem.* **354**, 189–208 (1993).
34. Kinnear, S. L. *et al.* Dual-barrel conductance micropipet as a new approach to the study of ionic crystal dissolution kinetics. *Langmuir* **29**, 15565–15572 (2013).
35. Edwards, M. A., Williams, C. G., Whitworth, A. L. & Unwin, P. R. Scanning ion conductance microscopy: A model for experimentally realistic conditions and image interpretation. *Anal. Chem.* **81**, 4482–4492 (2009).
36. Aldous, L. & Compton, R. G. The mechanism of hydrazine electro-oxidation revealed by platinum micro-electrodes: role of residual oxides. *Phys. Chem. Chem. Phys.* **13**, 5279–5287 (2011).
37. Saito, Y. A Theoretical Study on the Diffusion Current at the Stationary Electrodes of Circular and Narrow Band Types. *Review of Polarography* **15**, 177–187 (1968).
38. Dudin, P. V., Unwin, P. R. & Macpherson, J. V. Electro-oxidation of hydrazine at gold nanoparticle functionalised single walled carbon nanotube network ultramicroelectrodes. *Phys. Chem. Chem. Phys.* **13**, 17146–17152 (2011).
39. Eisner, U. & Gileadi, E. Anodic oxidation of hydrazine and its derivatives. *J. Electroanal. Chem. Interfacial Electrochem.* **28**, 81–92 (1970).
40. Chen, C. H. *et al.* Voltammetric scanning electrochemical cell microscopy: Dynamic imaging of hydrazine electro-oxidation on platinum electrodes. *Anal. Chem.* **87**, 5782–5789 (2015).
41. Rodes, A., Zamakhchari, M., El Achi, K. & Clavilier, J. Electrochemical behaviour of Pt(100) in various acidic media. *J. Electroanal. Chem. Interfacial Electrochem.* **305**, 115–129 (1991).
42. Harrison, J. A. & Khan, Z. A. The oxidation of hydrazine on platinum in acid solution. *J. Electroanal. Chem.* **28**, 131–138 (1970).
43. Gaunt, H. & Wetton, E. A. M. The reaction between hydrazine and oxygen in water. *J. Appl. Chem.* **16**, 171–176 (2007).
44. Lai, S. C. S., Dudin, P. V., MacPherson, J. V. & Unwin, P. R. Visualizing zeptomole (electro)catalysis at single nanoparticles within an ensemble. *J. Am. Chem. Soc.* **133**, 10744–10747 (2011).



# 5

## The reactivity of platinum microelectrodes

Decades of catalyst research have led to the development of more and more highly active electrocatalysts. To study catalysts with large kinetic rate constants, without being hindered by the used setup, it is necessary to use specialized experimental approaches. Ultramicroelectrodes (UMEs), which have at least one dimension that is smaller than the diffusion layer thickness ( $\approx 10 \mu\text{m}$ ) but much larger than the double layer thickness (10-100 Å), are typically used to overcome limitations by mass transport and resistance. However, the customary method of UME characterization via outer sphere redox probing has serious limitations. Here, we demonstrate these shortcomings by studying outer sphere redox couples, blank voltammetry, and various catalytic reactions for platinum UMEs. A comparison to macroscale Pt electrodes shows that UMEs perform much worse for surface sensitive catalytic reactions. Our results indicate that UME data should always be accompanied by blank characterization and reactivity measurements should be interpreted extremely carefully.



This chapter is based on Jacobse, L., Raaijman, S.J. & Koper, M.T.M. *Phys. Chem. Chem. Phys.* **18**, 28451–28457 (2016).

Electrode miniaturization increases mass transport and decreases absolute currents, both of which are beneficial for situations where high kinetic rates are concerned.<sup>1,2</sup> So long as the electrode is not reduced to nanometer scale, it should be possible to directly compare their results to the macro scale world. Upon further size reduction, e.g. in the case of nanoparticles, there are plenty of examples of size dependent reactivity due to the presence of specific nanoscale effects.<sup>3-13</sup>

On a different note, it is known from literature that the selectivity of Pt for the reduction of O<sub>2</sub> to H<sub>2</sub>O (with H<sub>2</sub>O<sub>2</sub> as intermediate/sideproduct) decreases by increasing the mass transport rate.<sup>14,15</sup> These observations were attributed to the competition between the adsorption/desorption of H<sub>2</sub>O<sub>2</sub> and trace contaminants that are present even in the highest purity grade chemicals.<sup>14-16</sup> Furthermore, the results presented in Chapter 4 seem to indicate, unexpectedly, that already on the micrometer scale differences in catalytic reactivity can be observed for the oxidation of hydrazine on Pt electrodes in HClO<sub>4</sub>.<sup>17</sup> This effect cannot be explained by competitive adsorption/desorption as no stable intermediates are known for the hydrazine oxidation to N<sub>2</sub>.<sup>18,19</sup> These results call for a more in-depth comparison between the reactivity of platinum macroscale electrodes and UMEs.

As reviewed by Climent and Feliu, the characterization of platinum surfaces in electrochemistry is, for historical reasons, most often performed in dilute sulfuric acid.<sup>20</sup> In this medium, the defining features in cyclic voltammograms (CVs) are clearly visible and relatively well understood.<sup>21</sup> With the introduction of flame annealing, these so-called blank CVs (blanks) have enjoyed excellent reproducibility between different labs, making it the default method for electrode characterization. From such blanks, one can discern the presence/absence of contaminating species and specific reaction sites as used in Chapter 3.<sup>20,22</sup>

Even though such practices are now widespread within the community studying Pt electrochemistry, blank CVs of (Pt) UMEs are rarely published and if at all only for high potential scan rates<sup>23-26</sup> which makes them rather insensitive towards slow reactions. Features resulting from reactions with slow kinetics or reactions which are diffusion limited (e.g. trace contaminations) will be suppressed under these conditions. Instead, surface probes such as the [Fe(CN)<sub>6</sub>]<sup>4-/3-</sup> or [FcCH<sub>2</sub>OH]<sup>0/1+</sup> redox couple are commonly used to characterize UMEs.<sup>27-30</sup> The problem is that such outer sphere redox couples are, despite some known complications<sup>31,32</sup>, in general insensitive to surface structure, composition, and cleanliness.<sup>33</sup> The main benefits from these experiments are to determine electrical contact and gain information regarding the geometrical dimensions of the electrode,<sup>1,2</sup> but their suitability for assessing surface reactivity is highly debatable.

In this chapter, we use outer sphere redox couples, blank voltammetry, and catalytic (inner sphere) reactions to make a solid comparison between the measured catalytic reactivity of macroelectrodes and UMEs. The redox couples studied are the oxidation of ferrocenemethanol ( $[\text{FcCH}_2\text{OH}]^{0/1+}$ ) and the reduction of hexaammineruthenium ( $[\text{Ru}(\text{NH}_3)_6]^{3+/2+}$ ). Similarly, catalytic reduction and oxidation reactions are also studied. For catalytic reactions, we make another distinction: reactions that are well-catalyzed by Pt in general (largely surface insensitive), and reactions that are sensitive to the presence of specific surface sites ('defects'). The chosen reactions are the oxidation of hydrazine ( $\text{N}_2\text{H}_4$ ),<sup>17,18,34,35</sup> the oxidation of methanol ( $\text{CH}_3\text{OH}$ ),<sup>12,36-40</sup> and the reduction of nitrate ( $\text{NO}_3^-$ ).<sup>41-43</sup> For each of these reactions, the Tafel slope, onset potential, and specific activity (where applicable) are compared to the values obtained on flame-annealed platinum electrodes under similar experimental conditions. In these experiments, we employ home-made UMEs. Information on their preparation and general experimental details can be found in Appendix F.

## 5.1 Electrode characterization

### Outer sphere reactions

The performance of UMEs is typically demonstrated using a reversible redox couple and this is thus our starting point. Figure 5.1 shows the CV of the reduction of 1 mM  $[\text{Ru}(\text{NH}_3)_6]^{3+}$  (A) and the oxidation of 1 mM  $\text{FcCH}_2\text{OH}$  (B) in 0.1 KCl for a Pt UME (red) and macroelectrode (black). The voltammetry of the macroelectrode is measured in hanging meniscus configuration rotating at 2800 r.p.m. with a scan rate ( $\nu$ ) of  $50 \text{ mV}\cdot\text{s}^{-1}$ . As the hysteresis in the CV of the UME is higher than for the macroelectrode,  $\nu = 10 \text{ mV}\cdot\text{s}^{-1}$  is used instead of  $\nu = 50 \text{ mV}\cdot\text{s}^{-1}$ . It should be noted that it is experimentally impossible to rotate the macroelectrode at speeds where the mass transfer coefficients would be the same for both experiments (ca. 17.000 r.p.m.). This explains the slightly less steep current increase for the macroelectrode. Apart from that no significant differences are observed between the different electrodes. Now, it is tempting to conclude that these CVs represent good and clean UMEs. However, in the following, we will demonstrate that this is not necessarily the case.

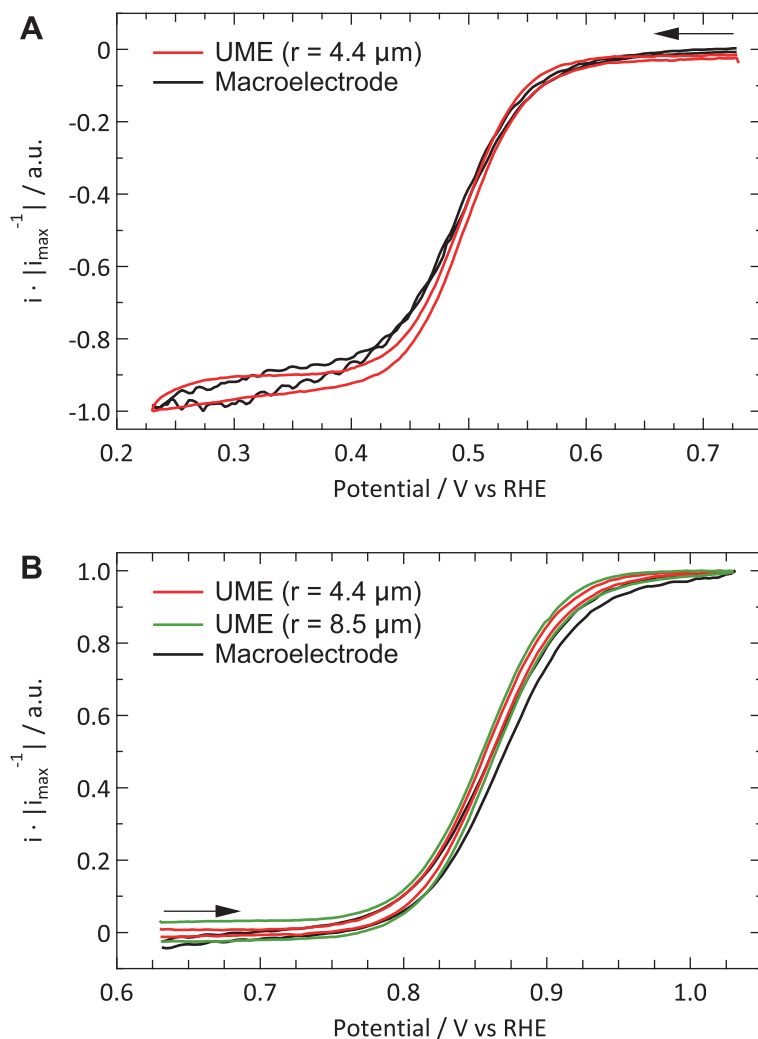


**Fig. 5.1 | Characterization by outersphere reactions:** (A) Reduction of 1 mM  $[\text{Ru}(\text{NH}_3)_6]^{3+}$  (B) Oxidation of 1 mM  $\text{FcCH}_2\text{OH}$ . The supporting electrolyte is 0.1 KCl and the shown CVs are the first cycles. The potential scan rate for the UME is  $\nu = 10 \text{ mV}\cdot\text{s}^{-1}$ . The macroelectrode CVs are measured in hanging meniscus configuration ( $f = 2800 \text{ r.p.m.}$ ), with a scan rate of  $\nu = 50 \text{ mV}\cdot\text{s}^{-1}$ . The response of a second UME in a separate experiment under identical conditions is shown in (B).

### Blank voltammetry

Outer sphere redox couples are very useful to study the geometric properties (i.e. size and shape) of an electrode. However, since they are insensitive to both surface structure and composition, they should not be the only method used to characterize a UME. Blank voltammetry is an essential tool for a full characterization, especially in the case of platinum electrodes as its voltammetric features are relatively well understood. Nevertheless, blank CVs for Pt UMEs are rarely reported and typically only at scan rates of at least  $\nu = 200 \text{ mV}\cdot\text{s}^{-1}$ .<sup>23–26</sup>

Figure 5.2 shows a decent blank voltammogram for a Pt UME (in red) compared to a flame annealed macroelectrode (in black). Although one would expect these CVs to be the same, there are some obvious differences. The hydrogen adsorption and desorption peaks (around 0.12 and 0.27 V) of the UME are not as well defined and less reversible than in the case of the macroelectrode. Also, the most negative adsorption/desorption (ca. 0.12 V) peak should be larger than the second peak (ca. 0.27 V), which it is not. The latter could in principle be explained by the production process of the thin Pt wires from which the UMEs are made. This process is known to lead to a preferential grain orientation.<sup>44</sup> Due to the small size of a UME, it is likely that only a single grain is exposed at the surface. Thus, the electrode can be considered to be a high-index single crystal. However, this mainly influences the ratio between the different hydrogen-related peaks and to a much smaller extent their sharpness.<sup>22</sup> However, this broadness might be caused by the fact that the UMEs have a relatively large roughness, as similar observations were made in Chapter 3 for the roughened Pt(111) surface.

The electrochemically active surface area of all electrodes is calculated from the hydrogen desorption integral in the region  $0.06 < E < 0.6 \text{ V}$  after subtraction of the double layer contribution, using the recently revisited value of  $230 \mu\text{C}\cdot\text{cm}^{-2}$  for a polycrystalline Pt surface in sulfuric acid.<sup>45</sup> After normalization to current densities, the UMEs typically show a larger double layer (DL) current than the macroelectrodes. One could explain this by an underestimation of the surface area of UMEs due to the less well-defined hydrogen desorption features. However, this seems in contradiction with the observation that the oxide reduction peak (ca. 0.78 V) is typically smaller for the UME than for the macroelectrode. Besides the larger DL current, one could argue that there is an additional, small, peak present around 0.45 V in the negative-going scan. Finally, the shape of the platinum oxidation region usually does not clearly show two bumps, in fact showing very few identifying features at all.

The second UME blank voltammetry (green) that is shown in Fig. 5.2 demonstrates the superiority of electrode characterization using blank voltammetry instead of an outer sphere redox couple. This blank has been measured prior to the oxidation of  $\text{FcCH}_2\text{OH}$  shown in Fig. 5.1B (green curve). Whereas the  $\text{FcCH}_2\text{OH}$  data suggests that this electrode performs well, this is contradicted by the blank voltammetry. In this case our normalization procedure (using the hydrogen desorption area) clearly leads to an underestimate of the active surface area, resulting in much too high current densities for hydrogen adsorption, oxide formation, and DL charging. Obviously, the shape also deviates significantly from what it should be. This implies that there is a process inhibiting the hydrogen desorption and oxide reduction reactions without a significant impact on outer sphere redox chemistry.

The aim of this chapter is not to obtain the perfect blank CV of a Pt UME, but merely to provide a better insight in the reliability of currently available methods to study UMEs. Within this framework, the blank shown in Fig. 5.2 (red curve) is among the best, in terms of quality and reproducibility, that we obtained. Therefore, this is considered a good starting point to study catalytic reactions. It is expected that the underestimation of the active surface area due to a blocking process also occurs, to some extent, for the other electrodes. To prove that this has only a minor effect on the observed differences, the blank CVs measured prior to the hydrazine and methanol oxidation are shown in Fig. 5.3. The blank CV measured prior to the nitrate reduction is shown in Fig. 5.6. From these blanks it is clear that the error in determining the active surface area is always smaller than a factor of 2.

## 5.2 Catalytic reactivity

### Hydrazine oxidation

Figure 5.4 compares the catalytic activity of a Pt UME and macroelectrode for the oxidation of 1 mM hydrazine in 0.5 M  $\text{H}_2\text{SO}_4$  with  $\nu = 50 \text{ mV}\cdot\text{s}^{-1}$ . The macroelectrode shows catalytic behavior that compares favorably with reports of Álvarez-Ruiz et al.,<sup>35</sup> whereas the behavior of the microelectrode does not agree with the UME ( $r = 25 \text{ }\mu\text{m}$ ) results of Aldous and Compton.<sup>34</sup> The results obtained for the oxidation 1 mM hydrazine in this work show activity akin to the most active cycle from the 10 mM hydrazine experiments by Aldous and Compton. Also, activation of the electrode as they observe when scanning to more oxidative potentials was

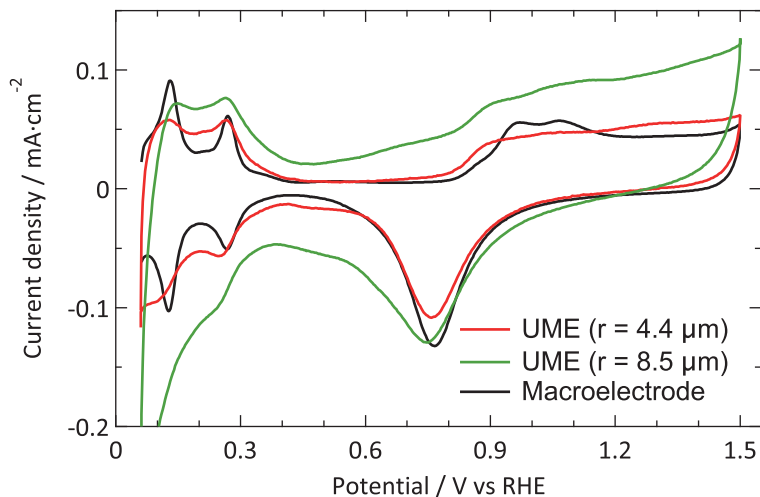


**Fig. 5.2 | Characterization by blank voltammetry:** Comparison of the blank voltammograms of platinum UMEs and a flame-annealed platinum spiral. The supporting electrolyte is 0.5 M  $\text{H}_2\text{SO}_4$  and the potential scan rate is  $\nu = 50 \text{ mV}\cdot\text{s}^{-1}$ .

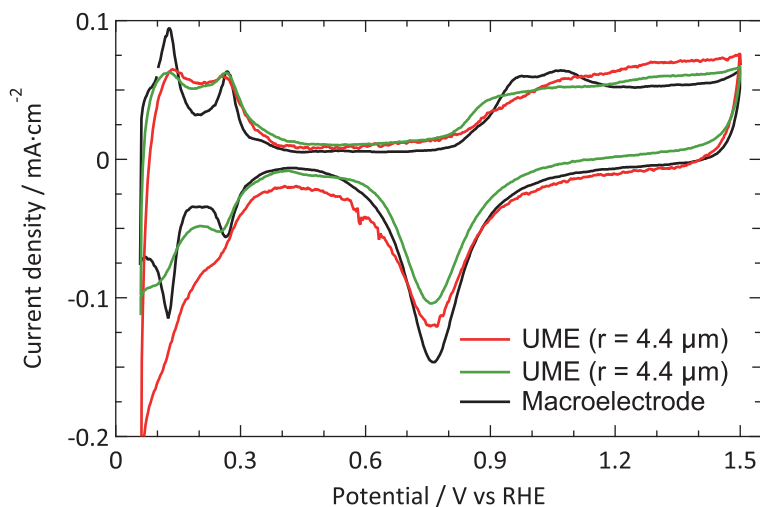


**Fig. 5.3 | Blank CVs before catalytic experiments:** blank CVs ( $\nu = 50 \text{ mV}\cdot\text{s}^{-1}$ ) of a platinum UME ( $r = 4.4 \mu\text{m}$ ) prior to the oxidation of 1 mM hydrazine (red) and 0.5 M methanol (green) in 0.5 M  $\text{H}_2\text{SO}_4$ . As the macroelectrode blanks were virtually identical, only one CV is shown (black).

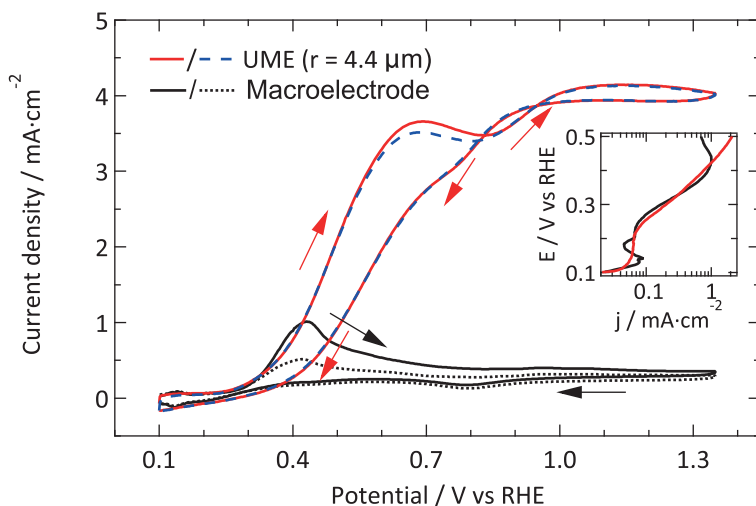


**Fig. 5.4 | Hydrazine oxidation:** First and fourth CV ( $\nu = 50 \text{ mV}\cdot\text{s}^{-1}$ ) of the oxidation of 1 mM  $\text{N}_2\text{H}_4$  in 0.5 M  $\text{H}_2\text{SO}_4$  on a Pt UME (red and dashed blue respectively) and macroelectrode (full and dotted black line respectively). The inset shows a Tafel plot of the first anodic scans.

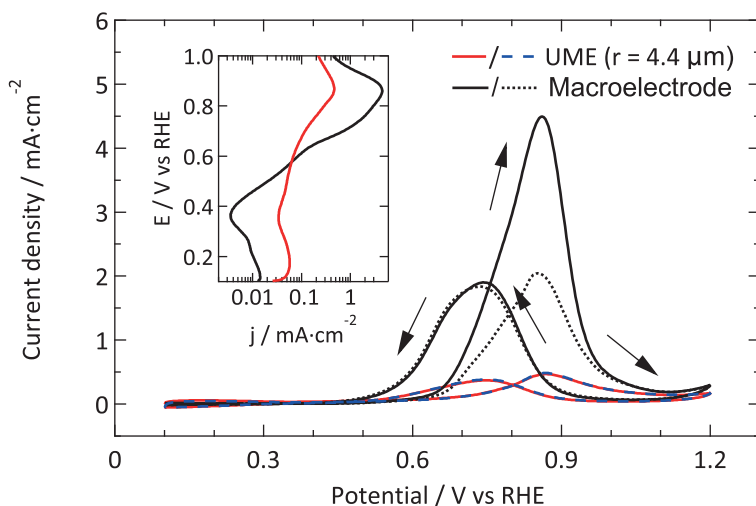


**Fig. 5.5 | Methanol oxidation:** First and fourth CV ( $\nu = 50 \text{ mV}\cdot\text{s}^{-1}$ ) of the oxidation of 0.5 M methanol in 0.5 M  $\text{H}_2\text{SO}_4$  on a Pt UME (red and dashed blue respectively) and macroelectrode (full and dotted black line respectively). The inset shows a Tafel plot of the first anodic scans.

not observed in the present study. An explanation for these differences can be found in the blank CV which is rather featureless for the data published by Aldous and Compton. Furthermore, no activation was observed when the polished microelectrode was kept at  $-0.05$  V vs. RHE for 5 minutes prior to measuring hydrazine oxidation. These observations suggest that the activation process is rather caused by the surface becoming cleaner with cycling than by the presence of residual oxides, as suggested previously.

As Pt is a very good catalyst for the oxidation of hydrazine, a diffusion limited current is observed for both electrodes. Due to the different diffusion geometries, the CVs of the macro- and microelectrode seem to be very different at first sight. However, if one takes a closer look at the characteristic features such as the onset potential and Tafel slope, it can be concluded that both electrodes show almost the same reactivity. The only (minor) difference regarding catalytic activity is the fact that the change in Tafel slope is slightly higher for the UME than for the macroelectrode. However, as the current density is limited by the diffusion of hydrazine to the surface and not by the catalytic properties of the working electrode for most of the potential range studied, it is to be expected that both electrodes show a similar behavior. Actually, this result is more or less similar to the observations for outer sphere reactions discussed above.

### Methanol oxidation

Figure 5.5 shows the catalytic activity of a Pt UME and macroelectrode towards the oxidation of  $0.5$  M methanol in  $0.5$  M  $\text{H}_2\text{SO}_4$  with  $\nu = 50$   $\text{mV}\cdot\text{s}^{-1}$ . Contrary to hydrazine oxidation, methanol oxidation depends strongly on the catalytic reactivity of specific Pt sites.<sup>35,38</sup> As we are not hindered by diffusion limitations, the CVs are similarly shaped. Moreover, this shape is in line with previous results available in literature,<sup>39,40</sup> although the ratio between peak currents during the forward and backward scan does not always agree. However, as this ratio is known to depend on scan rate,<sup>40</sup> this behavior is not completely unexpected.

Comparing the absolute reactivity, it is very clear that the UME is much less active than the macroelectrode. The good agreement between the normalized blank CVs (Fig. 5.3) confirms that this large difference (about a factor 10) cannot be explained by an error in the calculated surface areas. Furthermore, although the onset potential seems similar, the higher Tafel slope in the case of the microelectrode masks the precise onset potential.

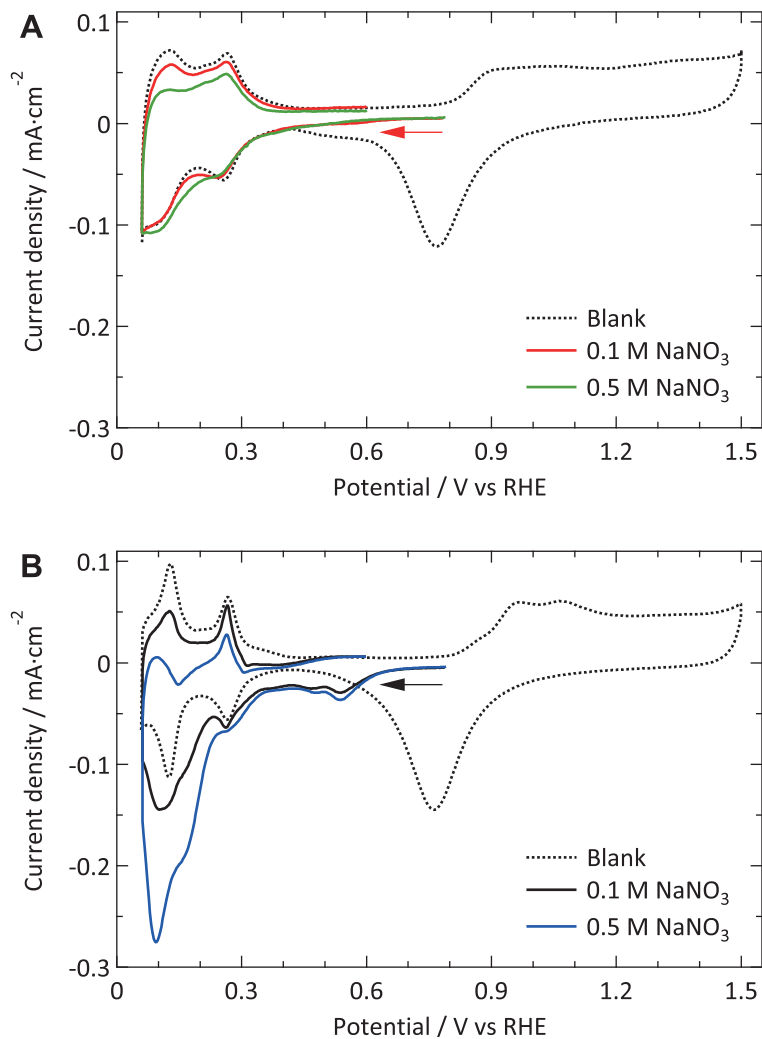


**Fig. 5.6 | Nitrate reduction:** Cyclic voltammetry ( $\nu = 50 \text{ mV}\cdot\text{s}^{-1}$ ) of the reduction of 0.1 and 0.5 M nitrate in 0.5 M  $\text{H}_2\text{SO}_4$  on (A) a Pt UME (red and green respectively) and (B) macroelectrode (black and blue respectively). The dotted lines show the blank voltammeteries measured right before the nitrate reduction experiment. The same scale is used for both graphs.

### Nitrate reduction

Figure 5.6 shows the catalytic activity of a Pt UME (A) and macroelectrode (B) for the reduction of 0.1 and 0.5 M nitrate in 0.5 M  $\text{H}_2\text{SO}_4$  with  $\nu = 50 \text{ mV}\cdot\text{s}^{-1}$ . The corresponding blanks are shown together with the nitrate reduction experiments, to give a better indication of the current that is actually related to nitrate reduction. As nitrate reduction overlaps with hydrogen adsorption/desorption, the Tafel plots of these experiments do not provide additional insight. For the macroelectrode, the results are similar to the observations in literature.<sup>41</sup> However, the current for the UME deviates barely from its blank response. As the UME shows so little reactivity, nothing sensible can be said about the onset potential.

One additional remark should be made regarding the voltammetric features that the regular-sized platinum electrode shows in the region  $0.5 < E < 0.6 \text{ V}$  vs. RHE. These peaks are likely due to the fact that the starting potential is relatively positive, and is actually also present on the microelectrodes after keeping the starting potential at 0.8 V vs. RHE for 5 seconds prior to measuring the CV. Considering that the indirect nitrate reduction starts at 0.8 - 0.9 V,<sup>41</sup> keeping the potential at 0.8 V for some time possibly introduces some nitrite near the surface, which could explain this additional feature observed.

## 5.3 UME vs. macroelectrode

In general, we can summarize the data for the catalytic reactions as exhibiting the same features as the outer sphere and blank results. Reactions that are relatively insensitive to the arrangement of the surface atoms (or their very nature) show the same reactivity for UMEs and macroelectrodes. However, for slow, more structure-sensitive reactions the UMEs are outperformed by macroelectrodes. The data suggest that the difference does not lie in the onset potential, but in the absolute current density. Also, from the blanks there is no solid evidence that a preferred grain orientation causes these differences. Thus, the most likely explanation is that part of the surface is blocked by contaminant species. As the most reactive sites will typically also bind strongest to contaminants\*, it makes sense that the largest effect is observed for slow, strongly catalytic reactions that occur preferentially at these sites.

---

\* When using platinum electrodes, methanol oxidation favors 'defect' sites and nitrate reduction is known to be very sensitive to coadsorbing species.<sup>3</sup>

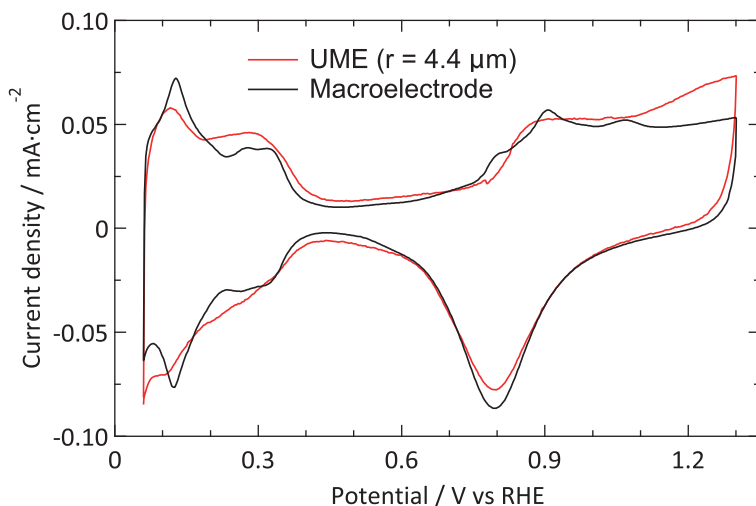


**Fig. 5.7 | Characterization in HClO<sub>4</sub>:** Blank CVs ( $\nu = 50 \text{ mV}\cdot\text{s}^{-1}$ ) of a platinum UME and macroelectrode in 0.1 M HClO<sub>4</sub>.

A crucial distinction lies in the source of the contamination: is it introduced during the preparation/cleaning of the UME, or are UMEs much more sensitive due to faster diffusion and smaller surface area as compared to macroelectrodes. Significantly, no improvement was observed after cleaning the UME with an O<sub>2</sub> plasma. Thus, if UMEs are inherently contaminated to a larger degree because flame-annealing is not an option, the source of the contamination is probably not organic in nature.

Even though the cleanest chemicals available in our lab were used, the level of contamination might be relevant on this scale. For example, the sulfuric acid used (Fluka, for trace analysis) contains, according to the manufacturer's specifications, among others,  $\leq 0.1 \text{ mg/kg Cl}^-$  ions. Assuming the maximum concentration, this means that our 0.5 M H<sub>2</sub>SO<sub>4</sub> electrolyte contains  $1.41 \cdot 10^{-7} \text{ M}$  chloride. Using a diffusion coefficient for chloride of  $2.0 \cdot 10^{-5} \text{ cm}^2 \cdot \text{s}^{-1}$ , the surface of our UME (roughness factor  $\approx 10$ ) can be fully covered with Cl<sup>-</sup> within approx. 20 minutes. This suggests that a significant fraction of the surface could be poisoned by chloride within the experimental time frame.

A similar argumentation was used by Katsounaros et al. who studied the effect of chloride ions, catalyst loading, and electrode rotation speed on the reduction of H<sub>2</sub>O<sub>2</sub>.<sup>15</sup> On the other hand, the cell used for the UME experiments has a rather small electrolyte volume (15 mL), such that the total number of chloride ions

present is of the same order of magnitude as the amount needed to generate a single adlayer. Finally, we consider the concentrations of other contaminants, e.g. organic carbon from the ultrapure water (<5 ppb) or nitrates from the glassware cleaning, to be too low to play a role here. Thus, the most plausible explanation is that the contamination originates from the (UME) preparation. It is noteworthy to mention that another often used supporting electrolyte,  $\text{HClO}_4$ , typically contains a 100-fold higher concentration of  $\text{Cl}^-$  than  $\text{H}_2\text{SO}_4$ . Although it proved to be more difficult to obtain good blank voltammeteries in perchloric acid electrolytes, the best ones we obtained (Fig. 5.7) are not inferior to the ones in sulfuric acid.

## 5.4 Conclusions

Despite the widespread application of UMEs, the customary method of electrochemical characterization via outer sphere redox probing is insufficient if the reactivity of the electrode is studied. In this study we provide a better insight in this subject by not only measuring outer sphere redox couples, but also blank CVs and catalytic reactivity of Pt UMEs. Reactions are chosen for which plenty of data on macroelectrodes is available from the literature. To validate the UME results, the data for macroelectrodes have been measured as well for comparison.

Activity for the reduction of  $[\text{Ru}(\text{NH}_3)_6]^{3+}$  and the oxidation of  $\text{FcCH}_2\text{OH}$  agree very well when comparing UME responses to annealed electrodes. The onset potential is virtually identical, and a minor difference in Tafel slope can be explained by the diffusion rates for the UME being faster than experimentally possible for a macroelectrode. Also in the case of a reaction for which Pt is known to be a very good catalyst, the oxidation of  $\text{N}_2\text{H}_4$ , no significant differences between the UME and macroelectrode are observed.

However, for reactions that depend stronger on surface structure, significant differences are observed. Blank CVs of the UME do not show the well-defined hydrogen and oxide related peaks that are observed for a polycrystalline electrode. Furthermore, the normalized current in the DL region is too high, while simultaneously the oxide reduction current is too low. The CVs for methanol oxidation on Pt are similarly shaped, but the current density for the UME is about an order of magnitude lower than expected based on the electrochemical surface area. The effect is even more drastic for the reduction of nitrate, with the UME exhibiting hardly any catalytic activity. The voltammeteries do not provide a means to identify a specific contaminant as no clear additional peaks were observed, although this does not imply that none were present.

Concluding, the most active sites on the UME surface seem to be blocked, with drastic consequences for reactions which depend strongly on the presence of these sites. Although the responsible process is not yet fully elucidated, there seem to be two reasonable explanations; either there is something bound so strongly to the surface (e.g. residual from the UME preparation) that it is very difficult to obtain a clean sample without flame-annealing, or diffusion is so fast that the surface easily becomes covered by trace contaminants in the electrolyte within the experimental time frame. The amount of contaminants in the used chemicals is too low to result in a significant coverage of the UME. Thus, it seems most plausible that the limited possibilities to clean the UMEs prior to use are the source of the observed effects.

Although it is uncommon to publish blank voltammograms for UMEs, our comparison to macroelectrodes shows that there is a crucial mismatch between the catalytic reactivities of these electrodes. Unfortunately, none of the widely used cleaning methods for UMEs provides an electrode cleanliness similar to flame annealing. Thus, in many cases the reactivity of UMEs will be underestimated if no proper electrochemical characterization is performed. Obviously, this may have severe consequences for the interpretation and reproducibility of data produced using UMEs.

## References

1. Zoski, C. G. Ultramicroelectrodes: Design, Fabrication, and Characterization. *Electroanalysis* **14**, 1041–1051 (2002).
2. Forster, R. J. Microelectrodes - Retrospect and prospect. *Encycl. Electrochem.* **3**, 160–195 (2002).
3. Koper, M. T. M. Structure sensitivity and nanoscale effects in electrocatalysis. *Nanoscale* **3**, 2054–2073 (2011).
4. Gilliam, R. J., Kirk, D. W. & Thorpe, S. J. Effect of electrode size on catalytic activity. *Electrochem. commun.* **9**, 875–878 (2007).
5. Gilliam, R., Kirk, D. & Thorpe, S. Dependence of catalytic activity on electrode size. *Electrochem. commun.* **9**, 2276–2279 (2007).
6. Zhou, W. P. *et al.* Morphology-dependent activity of Pt nanocatalysts for ethanol oxidation in acidic media: Nanowires versus nanoparticles. *Electrochim. Acta* **56**, 9824–9830 (2011).
7. Nesselberger, M. *et al.* The particle size effect on the oxygen reduction reaction activity of Pt catalysts: influence of electrolyte and relation to single crystal models. *J. Am. Chem. Soc.* **133**, 17428–33 (2011).
8. Chumillas, S. *et al.* Size and diffusion effects on the oxidation of formic acid and ethanol on platinum nanoparticles. *Electrochem. commun.* **13**, 1194–1197 (2011).
9. Tan, T. L., Wang, L.-L., Zhang, J., Johnson, D. D. & Bai, K. Platinum nanoparticle during electrochemical hydrogen evolution: adsorbate distribution, active reaction species, and size effect. *ACS Catal.* **5**, 2376–2383 (2015).
10. Kabbabi, A., Gloaguen, F., Andolfatto, F. & Durand, R. Particle size effect for oxygen reduction and methanol oxidation on Pt/C inside a proton exchange membrane. *J. Electroanal. Chem.* **373**, 251–254 (1994).

11. Park, S., Xie, Y. & Weaver, M. J. Electrocatalytic pathways on carbon-supported platinum nanoparticles: Comparison of particle-size-dependent rates of methanol, formic acid, and formaldehyde electrooxidation. *Langmuir* **18**, 5792–5798 (2002).
12. Rhee, C. K. *et al.* Size effect of Pt nanoparticle on catalytic activity in oxidation of methanol and formic acid: comparison to Pt(111), Pt(100), and polycrystalline Pt electrodes. *Langmuir* **25**, 7140–7 (2009).
13. Frelink, T., Visscher, W. & van Veen, J. A. R. Particle size effect of carbon-supported platinum catalysts for the electrooxidation of methanol. *J. Electroanal. Chem.* **382**, 65–72 (1995).
14. Chen, S. & Kucernak, A. Electrocatalysis under Conditions of High Mass Transport Rate: Oxygen Reduction on Single Submicrometer-Sized Pt Particles Supported on Carbon. *J. Phys. Chem. B* **108**, 3262–3276 (2004).
15. Katsounaros, I., Meier, J. C. & Mayrhofer, K. J. J. The impact of chloride ions and the catalyst loading on the reduction of H<sub>2</sub>O<sub>2</sub> on high-surface-area platinum catalysts. *Electrochim. Acta* **110**, 790–795 (2013).
16. Scherson, D. A. & Tolmachev, Y. V. Impurity Effects on Oxygen Reduction Electrocatalysis at Platinum Ultramicroelectrodes: A Critical Assessment. *Electrochem. Solid-State Lett.* **13**, F1 (2010).
17. Chen, C. H. *et al.* Voltammetric scanning electrochemical cell microscopy: Dynamic imaging of hydrazine electro-oxidation on platinum electrodes. *Anal. Chem.* **87**, 5782–5789 (2015).
18. García, M. D., Marcos, M. L. & Velasco, J. G. On the mechanism of electrooxidation of hydrazine on platinum electrodes in acidic solutions. *Electroanalysis* **8**, 267–273 (1996).
19. Rosca, V. & Koper, M. T. M. Electrocatalytic oxidation of hydrazine on platinum electrodes in alkaline solutions. *Electrochim. Acta* **53**, 5199–5205 (2008).
20. Climent, V. & Feliu, J. M. Thirty years of platinum single crystal electrochemistry. *J. Solid State Electrochem.* **15**, 1297–1315 (2011).
21. Vidal-Iglesias, F. J., Arán-Ais, R. M., Solla-Gullón, J., Herrero, E. & Feliu, J. M. Electrochemical characterization of shape-controlled Pt nanoparticles in different supporting electrolytes. *ACS Catal.* **2**, 901–910 (2012).
22. Solla-Gullón, J., Rodríguez, P., Herrero, E., Aldaz, A. & Feliu, J. M. Surface characterization of platinum electrodes. en. *Phys. Chem. Chem. Phys.* **10**, 1359–73 (2008).
23. Tavares, M. C., Machado, S. A. S. & Mazo, L. H. Study of hydrogen evolution reaction in acid medium on Pt microelectrodes. *Electrochim. Acta* **46**, 4359–4369 (2001).
24. Cook, D. A. *An investigation into the electrochemical properties of nanostructured metals and their application as amperometric biosensors* PhD thesis (University of Southampton, 2005), 34–40.
25. Zhan, D., Velmurugan, J. & Mirkin, M. V. Adsorption/desorption of hydrogen on Pt nanoelectrodes: evidence of surface diffusion and spillover. *J. Am. Chem. Soc.* **131**, 14756–60 (2009).
26. Fromondi, I., Shi, P., Mineshige, A. & Scherson, D. A. In situ, time-resolved normal incidence reflectance spectroscopy of polycrystalline platinum microelectrodes in aqueous electrolytes. *J. Phys. Chem. B* **109**, 36–9 (2005).
27. Aoki, K., Zhang, C., Chen, J. & Nishiumi, T. Fabrication of glass-coated electrodes with nano- and micrometer size by means of dissolution with HF. *Electrochim. Acta* **55**, 7328–7333 (2010).
28. Chen, S. & Kucernak, A. The Voltammetric Response of Nanometer-Sized Carbon Electrodes. *J. Phys. Chem. B* **106**, 9396–9404 (2002).
29. Guo, J., Ho, C.-N. & Sun, P. Electrochemical Studies of Chemically Modified Nanometer-Sized Electrodes. *Electroanalysis* **23**, 481–486 (2011).
30. Sur, U. K., Dhason, A. & Lakshminarayanan, V. A Simple and Low-Cost Ultramicroelectrode Fabrication and Characterization Method for Undergraduate Students. *J. Chem. Educ.* **89**, 168–172 (2012).
31. Peter, L., Dürr, W., Bindra, P. & Gerischer, H. The influence of alkali metal cations on the rate of the [Fe(CN)<sub>6</sub>]<sup>4-/3-</sup> electrode process. *J. Electroanal. Chem.* **71**, 31–50 (1976).
32. Beriet, C. & Pletcher, D. A microelectrode study of the mechanism and kinetics of the ferro/ferricyanide couple in aqueous media: The influence of the electrolyte and its concentration. *J. Electroanal. Chem.* **361**, 93–101 (1993).
33. Xiao, X., Pan, S., Jang, J. S., Fan, F.-R. F. & Bard, A. J. Single nanoparticle electrocatalysis: effect of monolayers on particle and electrode on electron Transfer. *J. Phys. Chem. C* **113**, 14978–14982 (2009).

34. Aldous, L. & Compton, R. G. The mechanism of hydrazine electro-oxidation revealed by platinum micro-electrodes: role of residual oxides. *Phys. Chem. Chem. Phys.* **13**, 5279–5287 (2011).
35. Álvarez-Ruiz, B., Gómez, R., Orts, J. M. & Feliu, J. M. Role of the Metal and Surface Structure in the Electro-oxidation of Hydrazine in Acidic Media. *J. Electrochem. Soc.* **149**, D35 (2002).
36. Herrero, E., Franaszczuk, K. & Wieckowski, A. Electrochemistry of methanol at low index crystal planes of platinum: an integrated voltammetric and chronoamperometric study. *J. Phys. Chem.* **98**, 5074–83 (1994).
37. Lai, S. C. S., Lebedeva, N. P., Housmans, T. H. M. & Koper, M. T. M. Mechanisms of carbon monoxide and methanol oxidation at single-crystal electrodes. *Top. Catal.* **46**, 320–333 (2007).
38. Housmans, T. H. M., Wonders, A. H. & Koper, M. T. M. Structure sensitivity of methanol electrooxidation pathways on platinum: an on-line electrochemical mass spectrometry study. en. *J. Phys. Chem. B* **110**, 10021–31 (2006).
39. Iwasita, T. Electrocatalysis of methanol oxidation. *Electrochim. Acta* **47**, 3663–3674 (2002).
40. Jiang, J. & Kucernak, A. Solid polymer electrolyte membrane composite microelectrode investigations of fuel cell reactions. II: voltammetric study of methanol oxidation at the nanostructured platinum micro-electrode|Nafion® membrane interface. *J. Electroanal. Chem.* **576**, 223–236 (2005).
41. De Groot, M. T. & Koper, M. T. M. The influence of nitrate concentration and acidity on the electrocatalytic reduction of nitrate on platinum. *J. Electroanal. Chem.* **562**, 81–94 (2004).
42. Dima, G. E., Beltramo, G. L. & Koper, M. T. M. Nitrate reduction on single-crystal platinum electrodes. *Electrochim. Acta* **50**, 4318–4326 (2005).
43. Dima, G. E., de Voors, A. C. A. & Koper, M. T. M. Electrocatalytic reduction of nitrate at low concentration on coinage and transition-metal electrodes in acid solutions. *J. Electroanal. Chem.* **554-555**, 15–23 (2003).
44. Greenwood, G. On the Cold-Working of Platinum Wires and the Fibrous Texture Thereby Produced. *Zeitschrift für Krist. - Cryst. Mater.* **78**, 242–250 (1931).
45. Chen, Q.-S., Solla-Gullón, J., Sun, S.-G. & Feliu, J. M. The potential of zero total charge of Pt nanoparticles and polycrystalline electrodes with different surface structure: The role of anion adsorption in fundamental electrocatalysis. *Electrochim. Acta* **55**, 7982–7994 (2010).

# A | EC-STM methods and general data processing

## A.1 Methods

The experiments described in Chapters 2-3 were carried out with the home-built EC-STM setup described previously.<sup>1-3</sup> This setup has proven to deliver high-resolution images, also on relatively rough surfaces, while still operating with significant scanning speeds. To allow for long-term experiments, for maintaining accurate control over the potentials, and for a high degree of cleanliness, we developed a new EC-STM cell with a reversible hydrogen reference electrode (RHE) that is compatible with the STM. A coiled platinum wire is used as counter electrode.

STM tips are electrochemically etched from Pt<sub>80</sub>Ir<sub>20</sub> wire (Goodfellow) and coated with electrophoretic paint (Clearclad HSR) and polyethylene to minimize faradaic contributions to the tunneling current ( $I_t$ ).<sup>4</sup> The Pt(111) sample (cut and polished <0.1°, Surface Preparation Laboratory, Zaandam, The Netherlands) is prepared by repeated cycles of mild etching ( $\pm 2$  V vs Pt, for 2.5 s at 50 Hz in an acidified CaCl<sub>2</sub> solution), flame annealing (5 min at  $\sim 1250$  K), and cooling in a reducing atmosphere (1:4 H<sub>2</sub>/Ar mixture). After the last cooling step, the surface is protected with ultrapure water ( $>18.2$  M $\Omega$ ·cm, Millipore Milli-Q) saturated with H<sub>2</sub>/Ar. After each experiment the sample is sonicated in acetone to remove the black residue left by the Viton o-seal.

All parts of the electrochemical flow cell and the electrolyte reservoir are cleaned in freshly prepared piranha (3:1 v/v H<sub>2</sub>SO<sub>4</sub> (Sigma-Aldrich, Puriss. p.a.) and H<sub>2</sub>O<sub>2</sub> (Merck)) followed by at least five times boiling in ultrapure water. The tubing through which the electrolyte flows, is cleaned with a diluted piranha solution and extensively rinsed with ultrapure water. The 0.1 M HClO<sub>4</sub> electrolyte is prepared from high-purity perchloric acid (Merck suprapur) and purged with N<sub>2</sub> for at least 2 hours prior to the experiment.

Before starting the experiment, the surface quality and cleanliness was checked by (large scale) STM imaging and cyclic voltammetry. Under these conditions the sample potential ( $U_s$ ) is not scanned above 0.85 V vs. RHE to prevent any change in the surface structure. Directly before and after each oxidation-reduction cycle, we

again record CVs up to 0.85 V to monitor the appearance of possible contaminants in between the oxidation experiments. All CVs are performed with the tip fully retracted ( $\sim 1 \mu\text{m}$  away) and at a fixed potential ( $U_t=0.45 \text{ V}$ ) to minimize the number of tip switches. Performing the ORCs with a retracted tip also prevents changes in the local sample potential due to the extremely small distance and large potential difference between the two electrodes. Such local potential changes would imply that the imaged area is no longer representative for the entire electrode surface. After each oxidation-reduction sequence (single ORCs for cycle 1-50, five ORCs for cycle 55-100, and ten ORCs for cycle 110-170) an STM image is acquired. During imaging the sample and tip potentials are fixed at  $U_s=0.4 \text{ V}$  and  $U_t=0.45 \text{ V}$ , respectively. This approach leads to a total data acquisition time of  $\sim 17$  hours. Unless mentioned otherwise, all data processing is performed with home-written routines using WaveMetrics Igor Pro software.

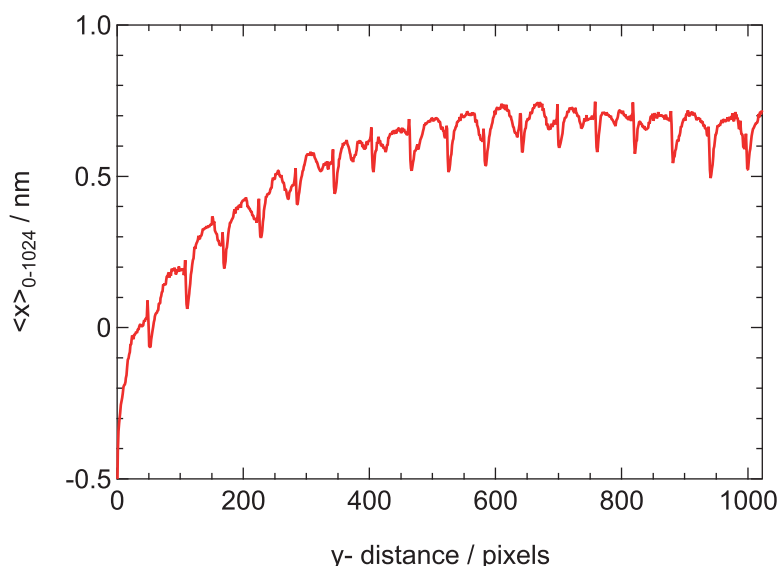


**Fig. A.1 | Distortion correction:** the average height along the x-direction, which is subtracted to correct for the creep and electrolyte flow distortions.

## A.2 EC-STM images

Our EC-STM data contain two distortions that need to be removed before applying a quantitative analysis. Firstly, as we retract the tip during the cyclic voltammetry, there is some creep in the  $z$ -direction which decays logarithmically along the slow scanning direction ( $y$ -direction). Furthermore, horizontal bands are observed in the images. The frequency of these bands corresponds to the frequency of the pump that regulates the electrolyte flow. As this behavior disappears over time, we attribute it to a faradaic current on the tip due to the presence of trace amounts of  $O_2$ . These distortions can be seen in the raw image which is shown in Fig. A.2A. Both distortions are removed by subtracting from each scan line ( $x$ -direction) the average value of that line. The magnitude of the correction is shown in Fig. A.1. After this correction, the sample tilt is removed by subtracting the best average fit of a plane through a single terrace. This results in the image that is shown in Fig. A.2B. Finally, in the analysis to determine site densities (Chapter 3), the image is corrected for the thermal drift, the result of which is shown in Fig. A.2C. Even though the thermal drift is small, it was found to have a small effect on the fitted nanoisland structures. The (time-dependent) drift vector is determined using cross-correlation functions on the whole set of images.

## A.3 Cyclic voltammetry

Our bipotentiostat and STM electronics operate separate from each other, but all the data is saved by the STM control software, and therefore perfectly aligned in time.<sup>5</sup> From these data we reconstruct cyclic voltammograms that are comparable to those measured with what is typically called ‘current integration mode’ for commercial (bi)potentiostats.

The charge related to hydrogen desorption is used as a measure for the number of available adsorption sites. This charge is determined by integrating the anodic current for sample potentials below 0.4 V after subtracting a (potential-independent) double layer current. Figure A.3 illustrates the determination of the hydrogen desorption charge for the pristine surface and after 8, 31, and 170 ORCs.

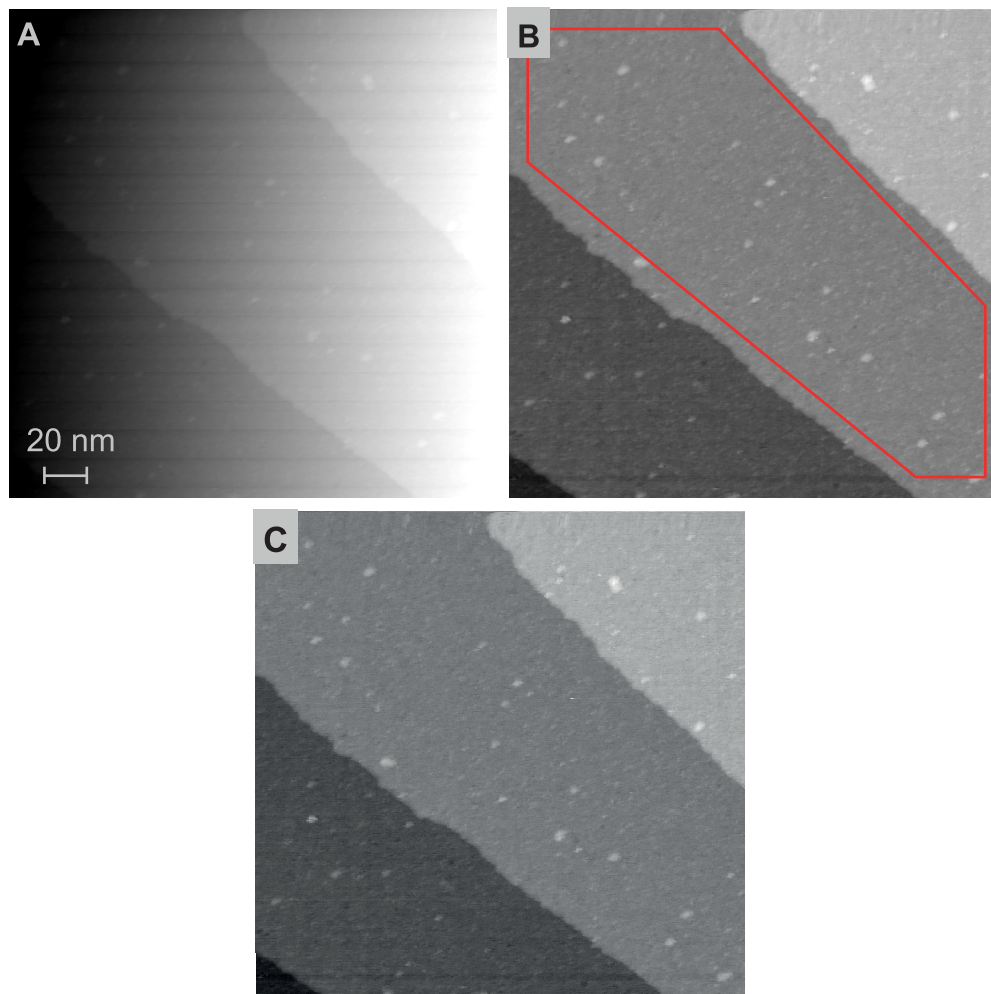


**Fig. A.2 | Image processing:** Panel (A) shows the raw EC-STM image of the pristine surface. (B) The same data after correcting for the distortions by creep, electrolyte pumping, and sample slope. The red line indicates the single terrace that is used for our analysis. (C) After applying the thermal drift correction.

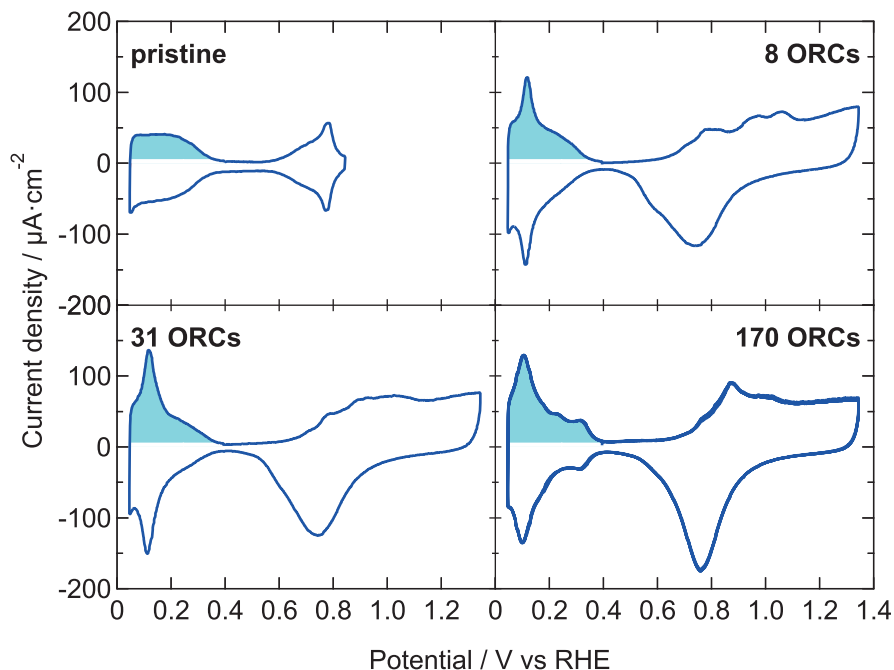


**Fig. A.3 | Hydrogen desorption charge determination:** the light blue areas indicate the charge related to the desorption of hydrogen for the pristine surface and after 8, 31, and 170 ORCs.

## References

1. Yanson, Y. I. & Rost, M. J. Structural Accelerating Effect of Chloride on Copper Electrodeposition. *Angew. Chemie Int. Ed.* **52**, 2454–2458 (2013).
2. Yanson, Y. I., Schenkel, F. & Rost, M. J. Design of a high-speed electrochemical scanning tunneling microscope. *Rev. Sci. Instrum.* **84**, 023702 (2013).
3. Rost, M. in *Encyclopedia of Interfacial Chemistry: Surface Science and Electrochemistry* 180–198 (Elsevier, 2018).
4. Güell, A. G., Díez-Pérez, I., Gorostiza, P. & Sanz, F. Preparation of reliable probes for electrochemical tunneling spectroscopy. *Anal. Chem.* **76**, 5218–5222 (2004).
5. Rost, M. J. *et al.* Scanning probe microscopes go video rate and beyond. *Rev. Sci. Instrum.* **76**, 053710 (2005).



# B | Roughening analysis of Pt(111)

## B.1 Vacancy evolution

Remainders of the oxidation-reduction process could be an alternative explanation for the observation of the ‘depressions’ with a depth smaller than one monolayer. However, such ‘residual oxides’ should disappear over time, as they are thermodynamically unstable. Previously, the presence of ‘residual oxides’ was used to explain the increased reactivity of a Pt ultramicroelectrode towards the oxidation of hydrazine.<sup>1</sup> Thus activation already decreased significantly over the course of several minutes. Our oxidation-reduction cycles are separated by  $\sim 15$  min., while we continuously record all signals. During this period we take three images. Figure B.1 shows one example of three subsequent images displaying the same part of the surface. During this set of images, the ‘depressions’ do not shrink and/or disappear. This static behavior makes it unlikely that the vacancy islands are actually ‘residual oxides’.

## B.2 Scaling analysis

As stated in the main text, the three power law dependencies that should be evaluated to (dis)prove scaling are:

$$\begin{aligned}\xi_{\perp} &\sim t^{\beta} \\ \xi_{\parallel} &\sim t^{1/z} \sim t^{\beta/\alpha} \\ \xi_{\perp} &\sim \xi_{\parallel}^{\alpha}\end{aligned}\tag{B.1}$$

Scaling occurs when this analysis leads to consistent values for the scaling exponents ( $\alpha$ ,  $\beta$ , and  $z$ ). Although this analysis is typically performed for a continuous evolution in time ( $t$ ), it was also demonstrated to be valid for situations where the evolution occurs in discrete steps (cycle numbers).<sup>2</sup> Figure B.2A to C show the results from the height-difference correlation analysis according to the power laws in Eq. B.1. Panel (A) shows the surface width as function of cycle number, (B) the parallel correlation length as function of cycle number, and (C) the surface width as function of parallel correlation length. These data are absolute values, whereas

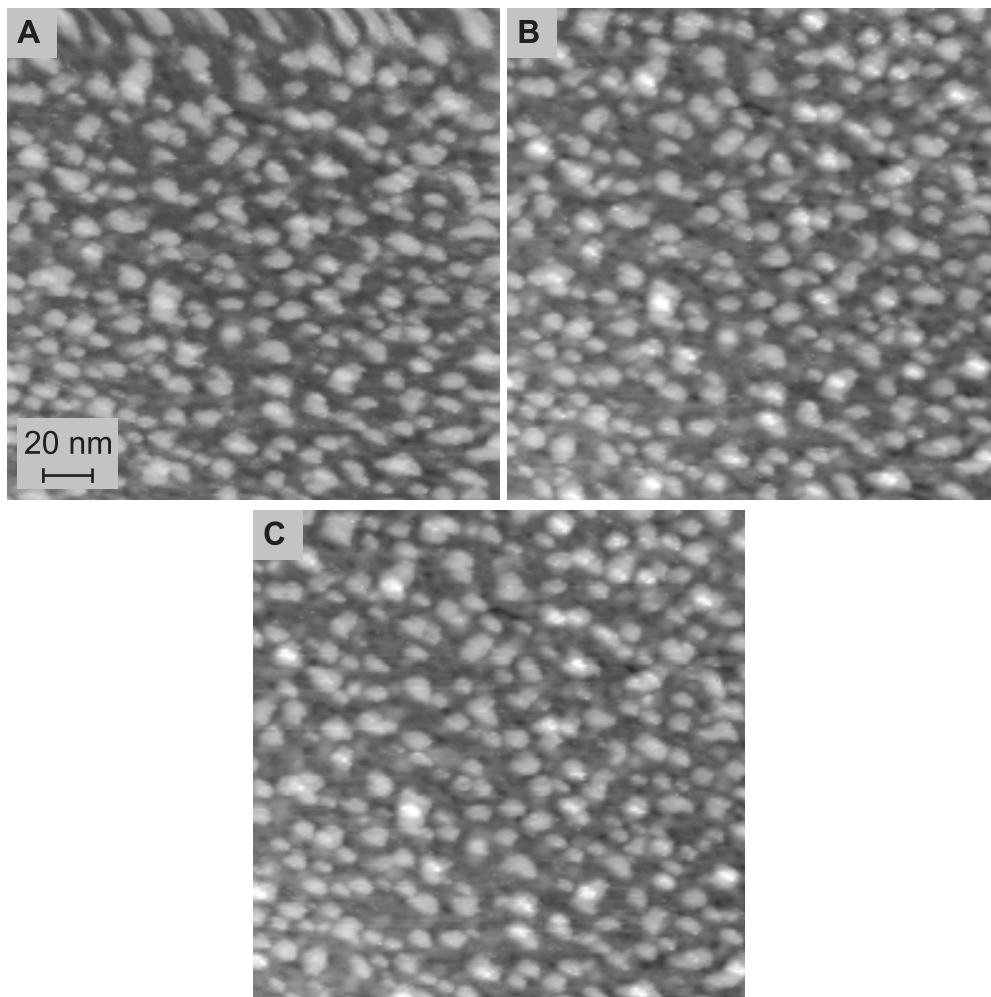


**Fig. B.1 | Time evolution of the vacancy islands:** three subsequent EC-STM images displaying the same area of the surface cropped to  $100 \times 100 \text{ nm}^2$ . The time for recording all three images was  $\sim 15$  min. During this time, the sample is kept at a constant, reducing potential ( $U_s = 0.4 \text{ V}$ ). These examples originate from a different set of data than those shown in the rest of the text.

values relative to the pristine surface would be necessary to determine the scaling exponents. However, this would lead to problems in panels (B) and (C) because most  $\Delta\xi_{\parallel}$  would be negative as  $\xi_{\parallel}(0) = 2.67$  nm. The value for  $\beta$  shown in Fig. 2.5B ( $\beta = 1.06 \pm 0.04$  during the first 15 ORCs, page 23) is determined after correcting for the offset of the perpendicular correlation length ( $\Delta\xi_{\perp}(0) = 0.026$  nm) of the pristine surface. Nonetheless, the changing slope of the surface width indicates directly that scaling does not occur over the full range of 170 oxidation-reduction cycles (ORCs). This is expected as we distinguish two regimes: initially a ‘nucleation & early growth’ regime, which is followed by a ‘late growth’ regime. From the STM images and the correlation between the roughness and cyclic voltammetry, we argue that the transition between these regimes should occur between the 20<sup>th</sup> and 31<sup>st</sup> ORC. Scaling could still occur in each of these two regimes. However, the behavior of the parallel correlation length in the first 10 cycles (Fig. B.2B) demonstrates that scaling does not occur during the ‘nucleation & early growth’ regime.

Figure B.2D to F show the power law dependencies during the ‘late growth’ regime. The analysis of the correlation coefficient suggests that the ‘late growth’ regime starts ultimately at cycle 31. However, cycle 31-33 are omitted from the scaling analysis, as the values for  $\xi_{\perp}$  strongly deviate from the power law dependence shown in Fig. B.2F. From the power law fits, we find  $\alpha = 0.91 \pm 0.09$ ,  $1/z = 0.54 \pm 0.07$ , and  $\beta = 0.69 \pm 0.02$ . These values do not form a single consistent description according to Eq. B.1 and thus we have to conclude that scaling does also not occur in the ‘late growth’ regime between cycle 34 and 170. However, the ideal scaling exponents are only reached asymptotically when a transition is involved between two regimes. From Fig. B.2D it seems that  $\beta$  decreases after  $\sim 75$  ORCs ( $\Delta$  cycle number = 41), whereas the other exponents remain constant. In this range we indeed find a smaller  $\beta$  ( $\beta_{75-170} = 0.62 \pm 0.05$ ), but due to the larger noise in  $\xi_{\parallel}$  it is not possible to accurately determine  $1/z$  and  $\alpha$ . Nonetheless, this observation suggests that scaling might be observed for even more extensive roughening experiments.

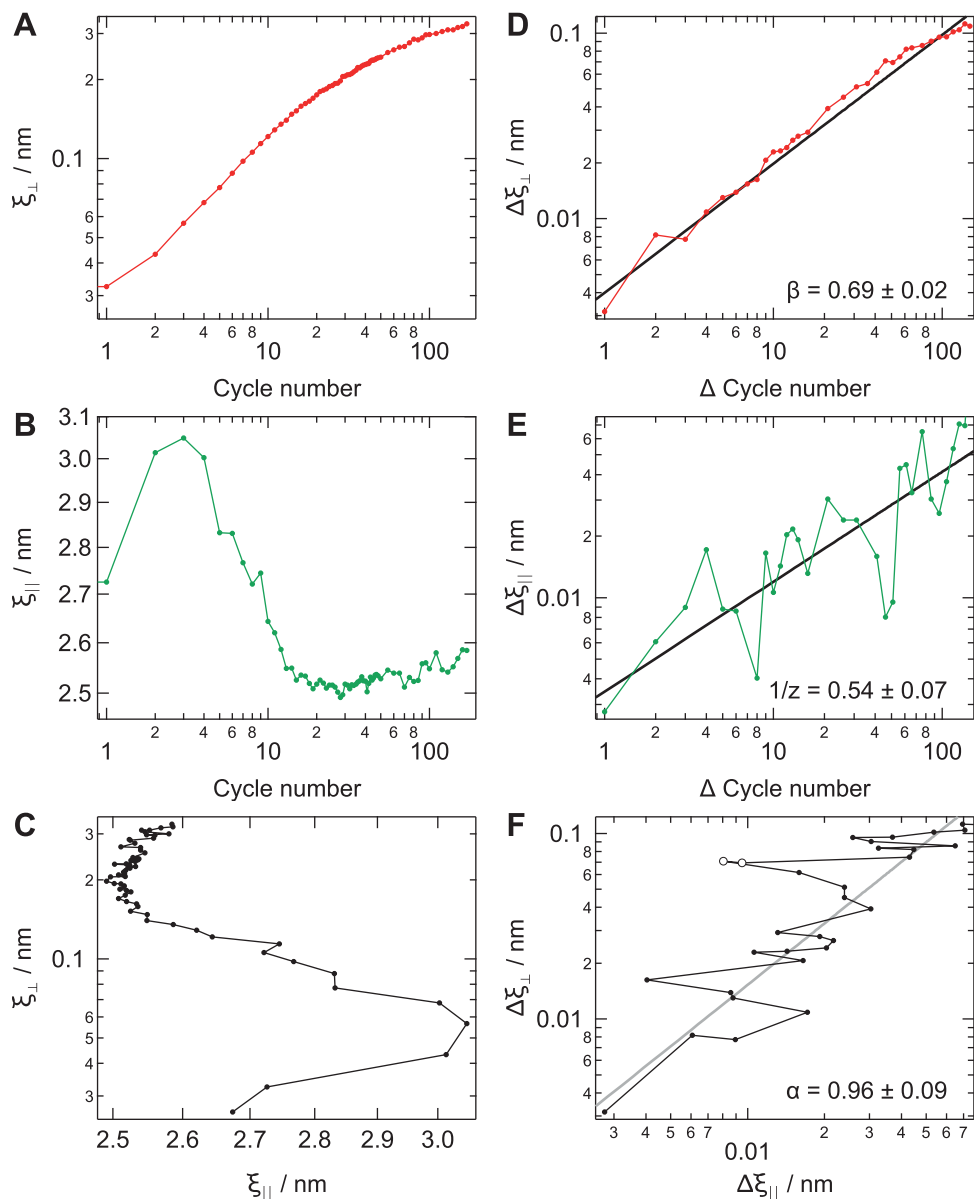


**Fig. B.2 | Roughness evolution during oxidation-reduction cycles:** (A-C) roughness evolution during all 170 ORCs. Panel B indicates directly that scaling does not occur. (D-F) roughness evolution during ‘late growth’ regime. The two values in (E) indicated with open symbols are considered outliers in the determination of  $\alpha$ . All values are relative to those determined after 34 oxidation-reduction cycles. Note that the (0,0) data point is not visible in this logarithmic plot. The straight lines are the power law fits to the data.

### B.3 Correlation coefficient

We define the cumulative correlation coefficient, quantifying the correlation between the hydrogen desorption charge and the surface width, as:

$$r(n) = \frac{\sum_{i=0}^n (q_{H,i} - \overline{q_{H,(0-n)}})(\xi_{\perp,i} - \overline{\xi_{\perp,(0-n)}})}{\sqrt{\sum_{i=0}^n (q_{H,i} - \overline{q_{H,(0-n)}})^2} \cdot \sqrt{\sum_{i=0}^n (\xi_{\perp,i} - \overline{\xi_{\perp,(0-n)}})^2}}, \quad (\text{B.2})$$

in which  $n$  is the cycle number.  $\overline{q_{H,(0-n)}}$  and  $\overline{\xi_{\perp,(0-n)}}$  are the mean hydrogen desorption charge and the mean surface width of the appropriate interval respectively. The validity of  $r(n)$  is determined by calculating its probable error as defined in the literature:<sup>3</sup>

$$\text{probable error} = \frac{0.6745(1-r^2)}{\sqrt{N}}, \quad (\text{B.3})$$

where  $N$  is the number of data points taken into account.

### References

1. Aldous, L. & Compton, R. G. The mechanism of hydrazine electro-oxidation revealed by platinum micro-electrodes: role of residual oxides. *Phys. Chem. Chem. Phys.* **13**, 5279–5287 (2011).
2. You, H. & Nagy, Z. Oxidation-reduction-induced roughening of platinum (111) surface. *Phys. B Condens. Matter* **198**, 187–194 (1994).
3. Eells, W. C. Formulas for Probable Errors of Coefficients of Correlation. *J. Am. Stat. Assoc.* **24**, 170–173 (1929).



# C | Surface site identification of roughened Pt(111)

## C.1 Average nanoisland

Determination of the average atomic island growth shapes starts from the drift-corrected EC-STM images as described in Appendix A. Subsequently, we have to; identify the individual islands and their boundaries; correct the height offset of the image (due to background subtraction); calculate the average measured island; and finally fit an fcc lattice to these average shapes. In the following, we describe the various steps in detail. Figure C.1 visualizes the overall process.

The initial island identification is performed using the built-in treshold and watershed functions in the GWYDDION SPM software.<sup>1</sup> A combination of Laplace filtering and constructing Voronoi cells is used to determine the island boundaries, see Fig C.1A. At this point, we filter out features that were identified as islands, but which are most likely tip effects, see the turquoise islands in Fig. C.1A. Not only are these islands significantly smaller, but in the STM images they are also poorly resolved, indicating tunneling via a double tip. The existence of these small islands leads to a bimodal island ‘footprint’ distribution. We can easily filter them out by applying a treshold to this distribution. For the averaging process, we find that the position of the absolute maximum within an island boundary yields slightly more accurate center positions compared to those found by the GWYDDION watershed function: we find that it leads to sharper average island shapes. The difference in center locations between these two methods is comparable to the size of the data points in Fig. C.1A. The entire surface is lifted with the absolute minimum of the considered surface area, in order to prevent averaging artifacts based on negative values. Finally, the average island is calculated via:

$$H(\mathbf{r}) = \frac{\sum_{n=1}^{n=n_{max}} h_n(\mathbf{r} - r_{0,n})}{n_{max}}, \quad (\text{C.1})$$

where  $H(\mathbf{r})$  is the average island,  $h_n$  is the  $n^{\text{th}}$  island, centered around  $(r_{0,n})$ , and  $n_{max}$  is the total number of analysed islands. An example of the averaging procedure is shown in Fig. C.1B.

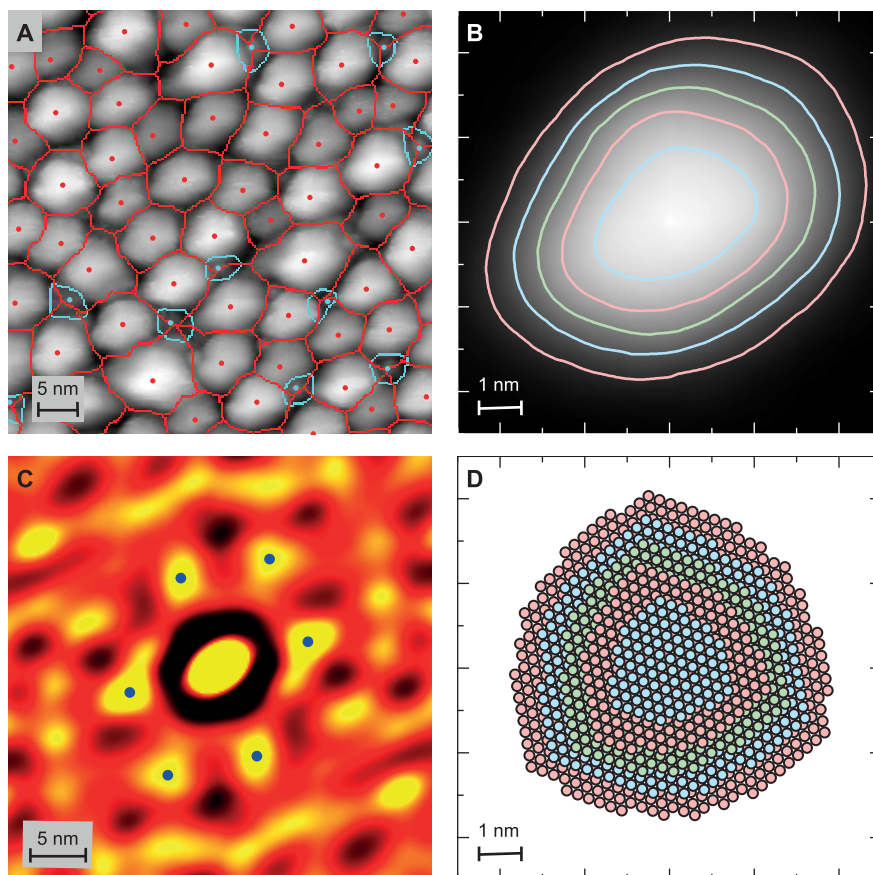


**Fig. C.1 | Nanoisland averaging and structure determinations:** (A) part of a background-corrected EC-STM image (after 110 ORCs) indicating the island centers and their boundaries. The turquoise dots and lines indicate islands that are considered to be tip effects, the red data is the final input for the averaging procedure. (B) Averaged nanoisland. The contour lines indicate heights of integer monolayers within this averaged island. (C) Result of a 2D autocorrelation analysis of the background-corrected EC-STM image shown in (A). The first order maxima (indicated by the dark blue markers) from all images are used to determine the lattice orientation. (D) The fitting result. The colors of the different atomic layers are the same as those of the contour plot in (B).

## C.2 Structural fits

Both 2D autocorrelation functions and height-difference correlation functions of the different STM images resemble a (distorted) hexagonal pattern, as expected from the Pt(111) symmetry. This is exemplified in Fig. C.1C. To reduce the number of fitting variables, the (distorted) hexagonal structure was used to fix the rotation of the fcc lattice in the fitting process. In principle, however, this approach does not provide means to distinguish between the  $\{100\}$  and  $\{111\}$  direction. Nonetheless, as the islands are only slightly asymmetric and the steps at the  $\{100\}$ -side ‘roughen’, this does not significantly hamper our analysis.

Any STM experiment always suffers from convolution between the surface features and the shape of the STM tip. If the shape of the tip is known, one can correct the images to some extent.<sup>2</sup> Such deconvolution calculations consist of the erosion of the STM image ( $A(\mathbf{r})$ ) by a so-called structure element ( $b(\mathbf{r})$ ) that describes the tip geometry:

$$A_{deconvoluted}(\mathbf{r}) = (A \ominus b)(\mathbf{r}) = \min_{\mathbf{s} \in B} [A(\mathbf{r} + \mathbf{s}) - b(\mathbf{s})], \quad (\text{C.2})$$

where  $\min$  indicates the minimum,  $B$  is the space in which  $b(\mathbf{r})$  is defined.<sup>3</sup> A typical tip can be described as a cone ending in a spherical apex. Deconvolution calculations, illustrated in Fig. C.2, indicate that our tip has a tip radius of about 1.5 nm. For larger radii, imaging artefacts clearly start to appear, as can be seen from the changing island shape and the thin lines that run in between the islands. This effect, most dramatically observed in Fig. C.2F, implies an overestimation of the convolution. On top of this, however, the asymmetry in the average island (Fig. C.1B) indicates that the tip used in this experiment does have a significant radial asymmetry. From repeated, similar experiments with other tips, of which some data are shown in Fig. C.3, we conclude that this asymmetry is indeed a tip effect and that the formed islands exhibit the expected threefold symmetry. If one would intend to correct the data for both the tip asymmetry and size (without additional tip characterization), the asymmetry would have to be removed first to prevent artefacts due to overestimation of the tip radius. However, implementing this in an analytical routine is far from trivial. The asymmetry seems to have the largest influence on our analysis, which is why we employ a threefold island symmetry as boundary condition in the fitting procedure to correct for it. As any tip size/shape will always lead to an overestimation of the island shape, we argue that the minimum height in all directions of the threefold symmetry describes the real island shape most accurately. This approach also minimizes the general

tip convolution effect, but no additional corrections are applied to further reduce this.

With the threefold minimum as boundary condition, and using the offset in the x- and y-direction as fit parameters, we consider the island structure for which the number of atoms underneath the average island contour is largest to be the best fitting result. We choose this approach because it is much more likely that an STM measurement overestimates the actual surface height (e.g. due to adatom/adsorbate diffusion or tip convolution), than that it underestimates the surface height. In the case that multiple structures occur which contain the same (maximum) number of atoms, the island structure that leads to the smallest fitting error (chi-square) with respect to the average island contour is preferred.

### C.3 Site densities

To fully capture the electrochemical reactivity in the site densities, it is necessary to take into account the spacing between step edges in the different layers. Thus, in the three relevant directions, we distinguish step sites and various facet sites: ‘wide facets’, ‘narrow facets’, and ‘low index facets’. We label the islands sides according to the geometry of the corresponding step sites, i.e. {100}-, {110}-, and {112}-side (‘100% kinked’). In principle the {110} step edge can also be described as {111} step edge. However, this assignment would complicate describing the full surface due to the shape of the {111} step unit cell. Also, the description from a {110} step edge makes the facet assignment intuitively better comparable to that of the {100} step edge. Figure C.4 gives an overview of the different unit cells used for counting these site densities; Table C.1 gives the corresponding site description. The most intuitive way to understand the site assignment, is by looking at the terrace sites adjacent to the actual ‘defect’ site. Note that, instead a trapezoidal unit cell, we use small triangular sites for this description (*vide infra*). Looking at how these triangular terrace sites are surrounded by sites belonging to a ‘defect’ in a different atomic layer, we distinguish four different possibilities: (1) the terrace sites are completely separated from each other, these are ‘separated defects’; (2) the terrace sites are touching, the ‘defects’ are still considered to be separated (e.g. step sites are still counted as steps and not yet as facets), but the terrace sites are now listed as ‘wide facets’; (3) the terrace sites have adjacent sites, both ‘defect’ and terrace sites are now counted as ‘narrow facets’; (4) terrace sites are overlapping or completely missing, these are the ‘low index facets’. This assignment is slightly complicated for corner sites, which is why ‘wide facets’ are not used for

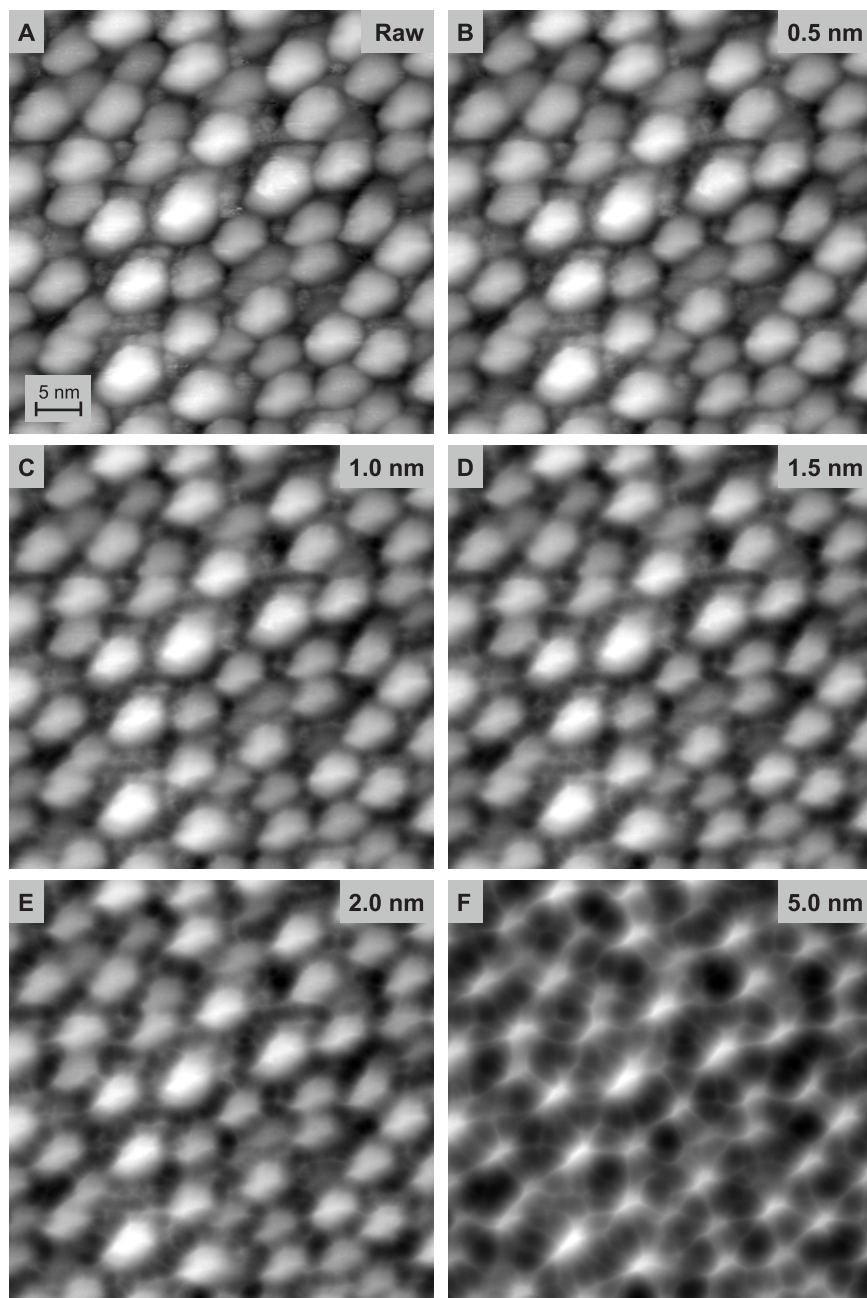


**Fig. C.2 | Tip deconvolution results:** (A) Part of an original EC-STM image. (B)-(F) The same data after applying the erosion operation<sup>2</sup> using tip radii of 0.5, 1.0, 1.5, 2.0, and 5.0 nm, respectively. The opening angle of the cone is fixed at 60°. The color scale is the same in all images. Note the sharp features and lines between the islands that appear for tips larger than 1.5 nm. As they are smaller than one atom, the tip radius is too large.

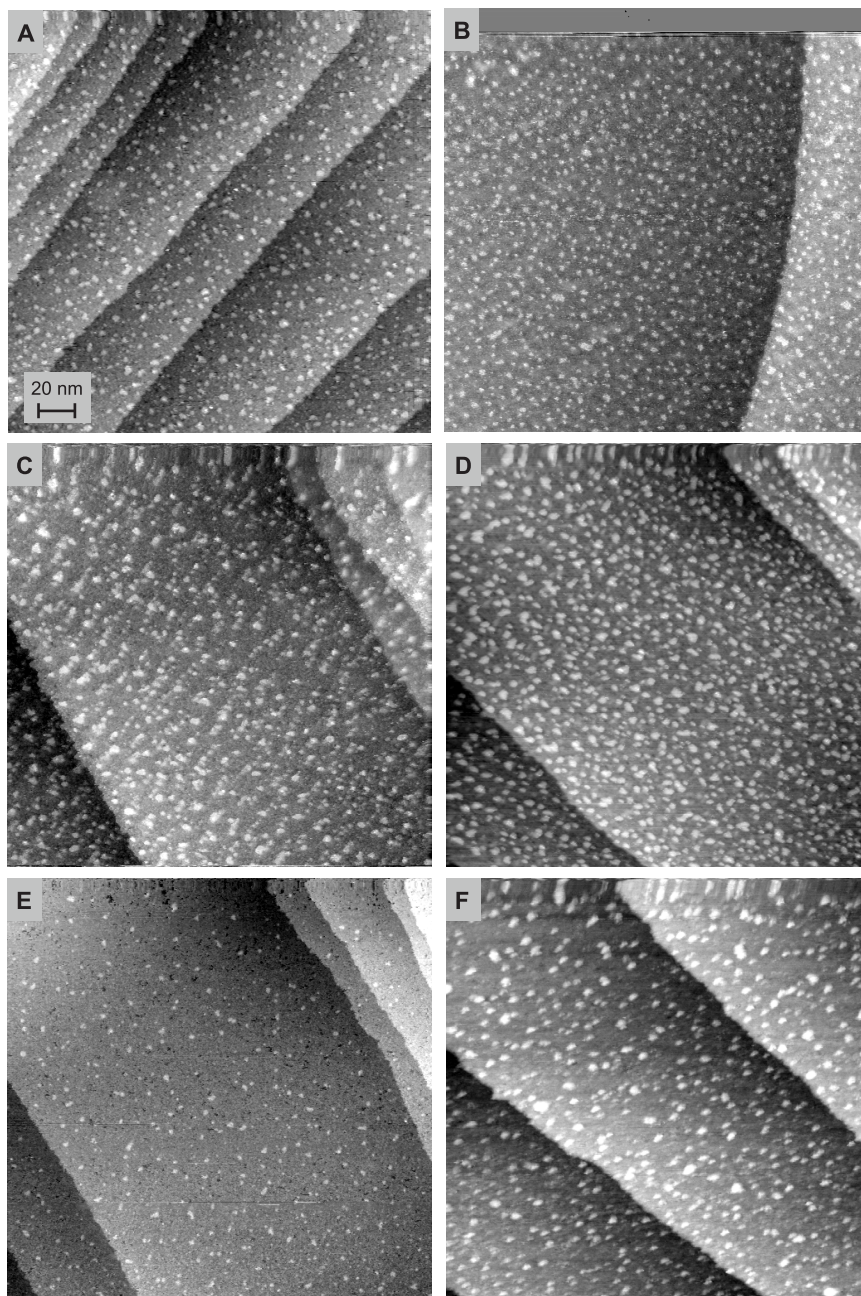


**Fig. C.3 | Island shape comparison:** EC-STM images from different experiments after some potential cycles. The images show neither that the islands do have a clear asymmetry in shape nor that the direction of the step edge influences the island asymmetry. This supports the argument that the observed asymmetry (clearest in Fig. C.1B) originates from a tip effect. All images are approximately 230x230 nm<sup>2</sup>.

corners. Instead, if the terrace site contains one and/or two undercoordinated atoms, both the terrace and the corner itself are counted as ‘narrow facets’. If the terrace site is missing, the corner forms a ‘low index facet’. Note that at the {111}- and {112}-side, we could increase the surface slope even further by forming {111}-facets and {210}-facets, respectively. However, such sites are not observed in the average island structure. Table C.1 also mentions the formation of {211} and {221} kink facets, which are not shown in Fig. C.4. Such sites occur on a step edge that forms a ‘narrow facet’ (green), when one of the kink sites is translated one atomic distance along the step edge.

To be able to assign all sites on the surface, it is sometimes necessary to use sites that are smaller than whole unit cells. To determine the correct site densities, one must therefore apply the appropriate prefactors: two triangular terrace sites form one full terrace site; steps, facets, and kinks in the {100} and {111} direction consist of two times  $1/2$  site; the steps/facets in the {112} direction of two times 1 site; and corner sites count as  $1/2$  site. Table C.2 gives the counts of the different sites as indicated by the colored planes in Fig. C.4. Figure SC.5 shows all the individual site densities as counted from the series of average island structures. In Fig. 3.2 (page 33), these site densities were summarized in either the {100} or {111} direction. To do this, the densities of corner sites and {112}-related sites were equally split over these two classes. Figure C.6 shows the correlations between the charge of the  $A_{2-4}$  peaks and the corresponding surface sites as discussed in Chapter 3. Despite the value of the correlation coefficient, there is a clear discrepancy in the correlation in Fig. C.6A, which originates from the fast increase of the  $A_2$  peak during the first three cycles (see Fig. 3.2 on page 33). The underlying reasons for this behavior could be the formation of vacancy edge sites with a {110} geometry. Another explanation could be that some of these step sites were already present at the initial surface and get ‘cleaned’ during the ORCs. Neglecting the data of the first three cycles to determine the correlation coefficient, we obtain a correlation coefficient of 0.93. The grey line in Fig. C.6 shows the correlation between the {110} facet sites and the  $A_4$  charge after applying a moving average (with a width of 5 datapoints) filter to the site densities. This leads to a significantly larger correlation coefficient (0.93 vs. 0.54.). The large variation in the facet site densities is considered to be a fitting artefact, as the absolute densities of these sites are rather low.

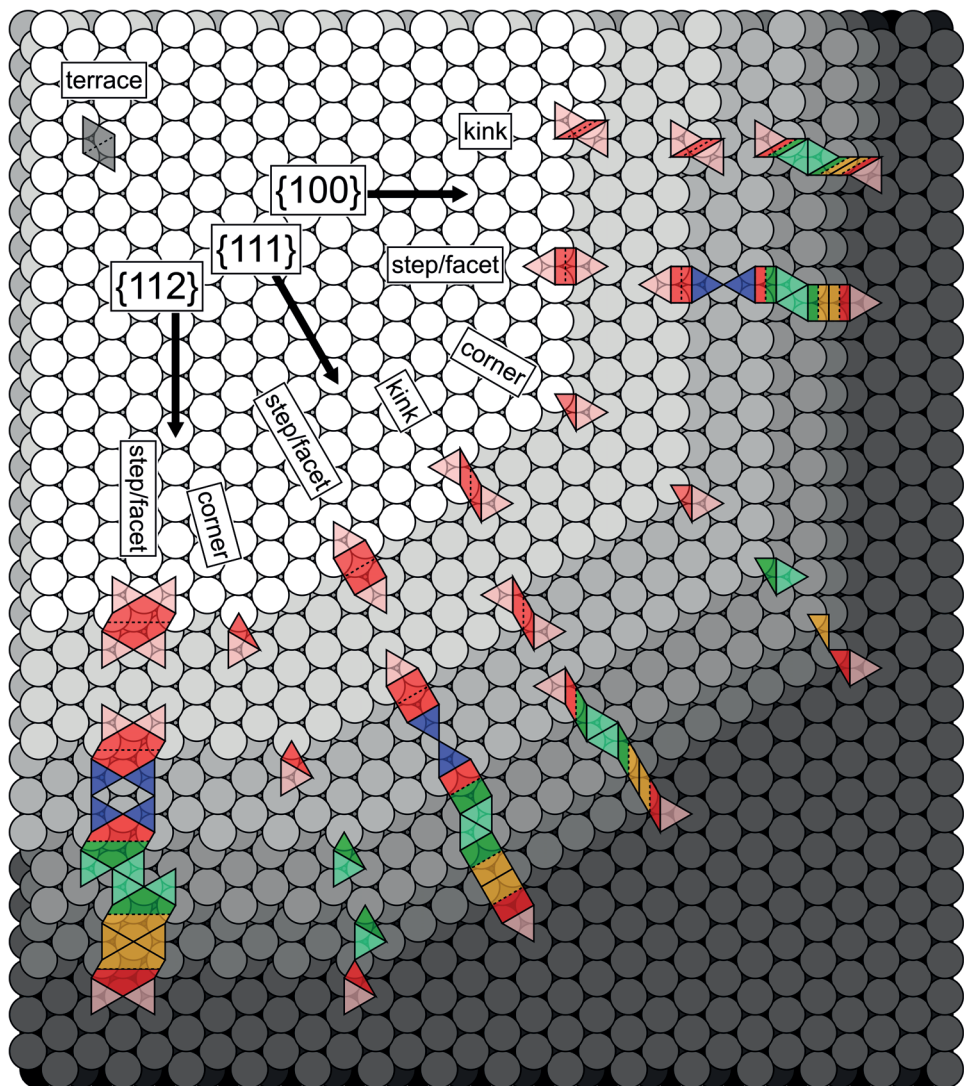


**Fig. C.4 | Site assignment:** Assignment of the different parts of the unit cells to 'separated defects', 'wide facets', 'narrow facets', and 'low index facets' (red, blue, green, and yellow, respectively) Note that for 'wide facets' only the terrace sites are expected to show different behavior, the step itself is considered a 'separated defect'. Terrace sites belonging to 'separated defects' and 'narrow facets' are indicated in light red and light green, respectively. The geometry of 'wide facet' kink sites is explained in the text, but not shown here.

**Table C.1 | Site assignment:** Overview of all different surface geometries that were considered in the counting process. ‘T’ indicates terrace sites, belonging to a specific ‘defect’ geometry as indicated by its subscript label.

Direction/Type	‘Separated defect’	‘Wide facet’	‘Narrow facet’	‘Low index facet’
{100}	‘Defect’	{100} step	{311} step	{100} facet
	Terrace	{100} kink $T_{\{100\}-step}$ $T_{\{100\}-kink}$	{100} kink {211} facet {211} kink	{100} kink facet {311} kink {311} facet {311} kink
{111}	‘Defect’	{110} step	{110} step	{110} facet
	Terrace	{110} kink $T_{\{110\}-step}$ $T_{\{110\}-kink}$	{110} kink {221} facet {221} kink	{110} kink facet {331} kink {331} facet {331} kink
{112}	‘Defect’	{112} step	{112} step	{531} facet
	Terrace	$T_{\{112\}-step}$	{753} facet	{531} facet
Corner $_{\{100\}-\{111\}}$	‘Defect’	Corner	Corner	LI Corner
	Terrace	$T_{corner}$	$T_{corner}$	-
Corner $_{\{111\}-\{112\}}$	‘Defect’	Corner	Corner	Narrow Corner
	Terrace	$T_{corner}$	$T_{corner}$	Narrow Corner

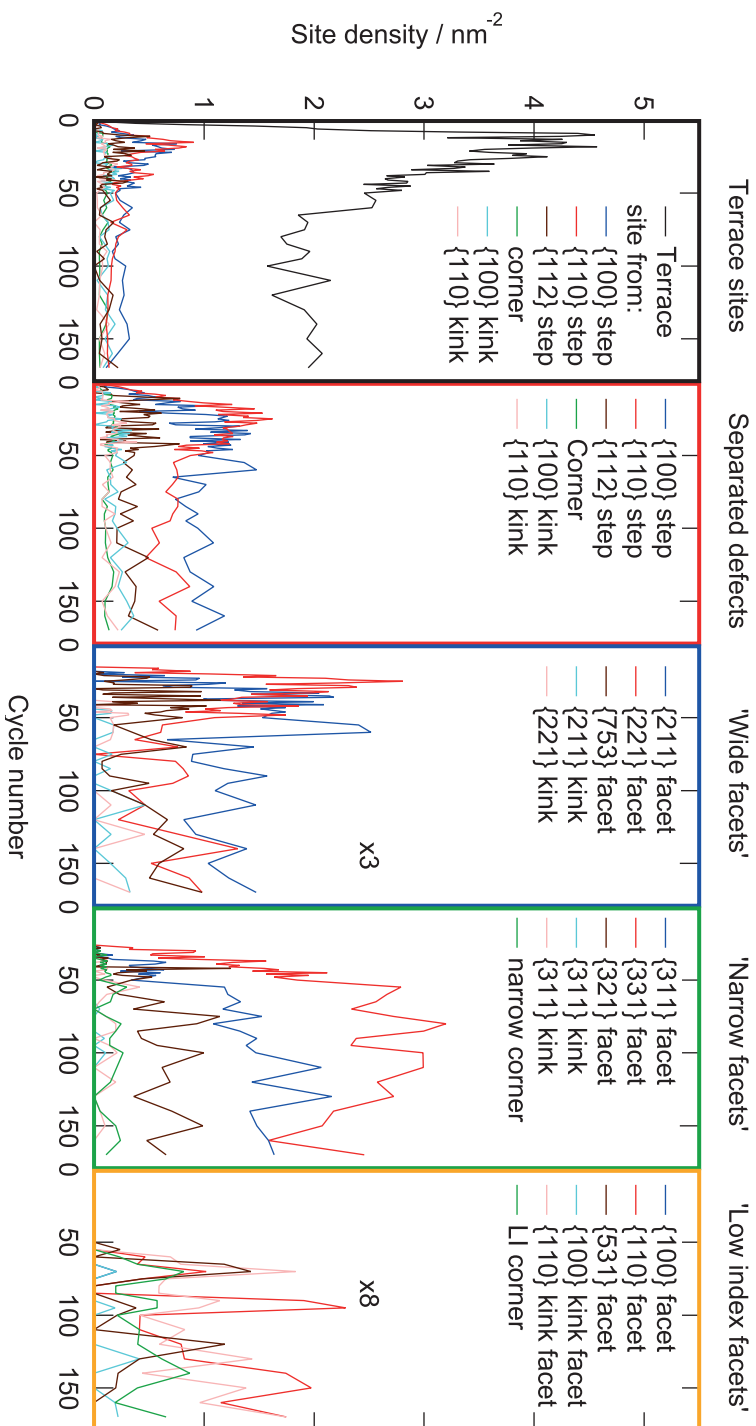
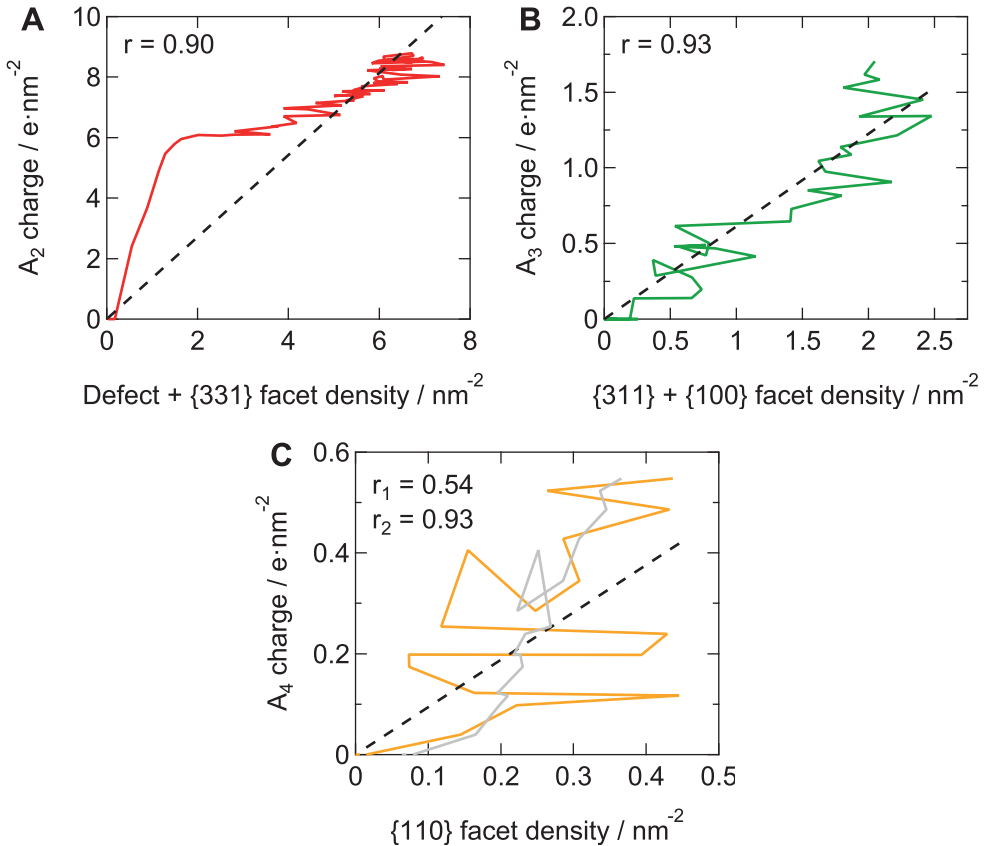


Fig. C.5 | Individual site densities: The evolution of the site densities for all different surface geometries considered.

**Table C.2 | Counting example:** Site counts of the colored sites in Fig. C.4 after normalization.

Type	Normalized site counts
{100} step/facet	3 {100}-steps; 2 $T_{\{100\}\text{-step}}$ ; 1 {211} facet; 2 {311} facets; 1 {100} facet
{111} step/facet	3 {110}-steps; 2 $T_{\{110\}\text{-step}}$ ; 1 {221} facet; 2 {331} facets; 1 {110} facet
{112} step/facet	6 {112}-steps; 4 $T_{\{112\}\text{-step}}$ ; 2 {753} facets; 4 {321} facets; 2 {531} facets
{100} kink	3 {100}-kinks; 3 $T_{\{100\}\text{-kink}}$ ; 2 {311} kink facet; 1 {100} kink facet
{111} kink	3 {110}-kinks; 3 $T_{\{110\}\text{-kink}}$ ; 2 {331} kink facet; 1 {110} kink facet
Corner <sub>{100}-{111}</sub>	1.5 Corner; 1.5 $T_{\text{corner}}$ ; 1 Narrow corner; 0.5 LI corner
Corner <sub>{111}-{112}</sub>	1.5 Corner; 1.5 $T_{\text{corner}}$ ; 2 Narrow corners

**Fig. C.6 | Correlations between peak charge and site densities:** (A)  $A_2$  charge vs the density of ‘separated defects’ + {331} facets. (B)  $A_3$  charge vs the density of {311} + {100} facet sites. (C)  $A_4$  charge vs the density of {110} facet sites. A detailed motivation behind these correlations is provided in Chapter 3.

## C.4 CV fits

Methods to determine the different contributions to the hydrogen region of Pt CVs have been discussed in literature before. Here, we use the approach described by McCrum and Janik, who fit an inverse hyperbolic cosine to the broad terrace feature and gaussian functions to the ‘defect’-peaks.<sup>4</sup> To capture the changing shape of the  $A_2$ -peak, it turns out that this peak needs requires fitting with a summation of two gaussians centered around the same potential. To obtain good fits and limit the degrees of freedom, the (111) terrace feature is fixed for all CVs. An example of the fitting result (after 150 cycles) is shown in Fig. C.7.

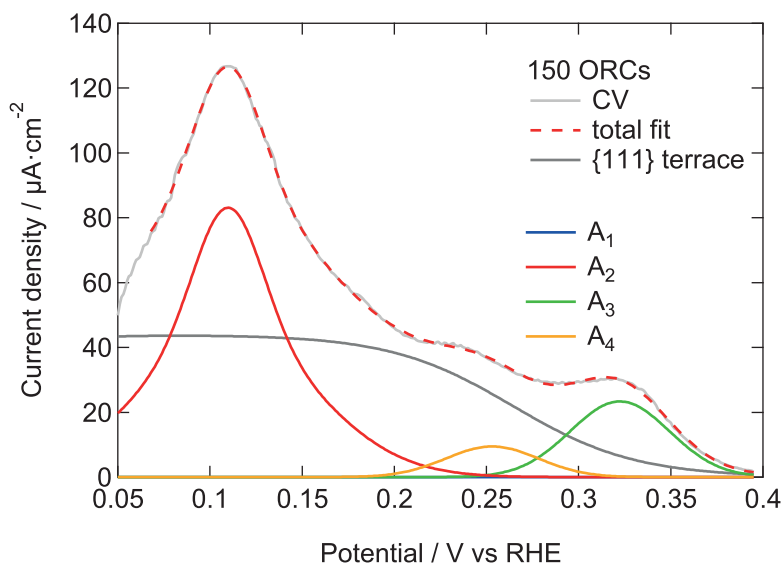


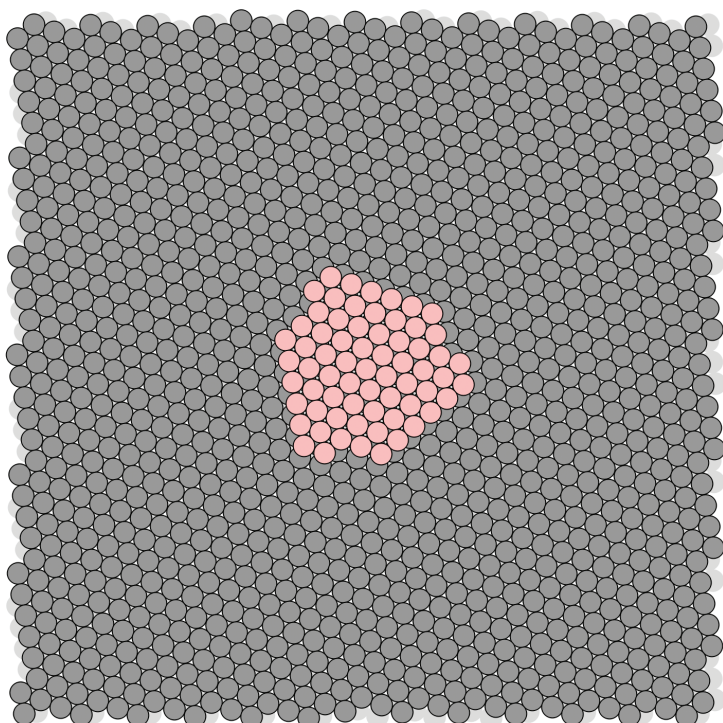
**Fig. C.7 | CV fitting:** Example of the charge determination for the different contributions to the hydrogen desorption reaction.

## References

1. Nečas, D. & Klapetek, P. Gwyddion: an open-source software for SPM data analysis. *Cent. Eur. J. Phys.* **10**, 181–188 (1 2012).
2. Villarrubia, J. Algorithms for scanned probe microscope image simulation, surface reconstruction, and tip estimation. *J. Res. Natl. Inst. Stand. Technol.* **102**, 425 (1997).
3. Soille, P. *Morphological Image Analysis* 392. eprint: 1011.1669 (Springer Berlin Heidelberg, 2004).
4. McCrum, I. T. & Janik, M. J. Deconvoluting Cyclic Voltammograms To Accurately Calculate Pt Electrochemically Active Surface Area. *J. Phys. Chem. C* **121**, 6237–6245 (2017).

# D | Platinum nanoisland structures

This appendix contains the series of nanoisland structures, belonging to Chapter 3. The data are directly accessible via the digital version of this thesis using an appropriate pdf viewer (e.g. Acrobat Reader). Other movies, containing results described in Chapters 2-4 can be accessed via the supplementary information of the corresponding publications.





# E | Details on SECCM experiments

## E.1 Methods

Fresh electrolyte solutions are prepared before each experiment from ultrapure water (SELECT-HP, Purite, 18.2 M $\Omega$ -cm resistivity at 25 °C), HClO<sub>4</sub> (ca. 70% solution in water, Acros Organics), and hydrazine monohydrate (Acros Organics). Pd-H<sub>2</sub> is used as a quasi-reference counter electrode (QRCE) for SECCM and as a reference electrode (RE) for macroscale and microscale experiments. This electrode is prepared by evolving hydrogen on a Pd wire (99.9% purity, 0.25 mm thickness; Alfa Aesar) in a supporting electrolyte (0.1 M HClO<sub>4</sub>) solution. All potentials are reported against the reversible hydrogen electrode ( $E_{\text{Pd-H}_2}^{\ominus} = 50 \text{ mV vs RHE}$ ).<sup>1</sup>

Macroscopic CV measurements are carried out in a traditional three-electrode setup. A polycrystalline Pt wire is used as the working electrode, with the Pd-H<sub>2</sub> RE and another Pt wire as the counter electrode. Prior to each experiment these Pt electrodes are cleaned by flame-annealing. The exposed surface area of the working electrode is on the order of a few tens of mm<sup>2</sup> and varies somewhat between different experiments. No attempt is made to determine the exact electroactive surface area, as the hydrogen underpotential deposition region of the CV contains oxygen reduction reaction features for the experiments performed in the presence of oxygen.

A 25  $\mu\text{m}$  diameter Pt-disk ultramicroelectrode (UME) is prepared by sealing a Pt microwire into glass.<sup>2</sup> It is then polished on a 0.1  $\mu\text{m}$  diamond-lapping disc (PSA, Buehler) until a flat surface was obtained. Before use, the Pt UME is prepared by further mechanical polishing (MasterPrep 0.05  $\mu\text{m}$  alumina polishing suspension, Buehler) and finally through the use of a clean polishing pad without alumina, followed by thorough rinsing with ultrapure water. For experiments under deaerated conditions, the electrolyte solution (10 mL) is flushed with N<sub>2</sub> for 30 min before the measurements.

A polycrystalline Pt foil (>99.95% purity, 0.010 mm thickness; Advent Research Materials) is used as the sample (working electrode) for the SECCM imaging experiments. Prior to each experiment, the foil is cleaned by rinsing with ultrapure water and flame-annealing. An area of interest on the foil is marked by focused ion beam milling (JEOL 4500, JEOL). Scanning electron microscopy (SEM) images

of the Pt sample were recorded after each imaging experiment on a Zeiss SUPRA 55 variable-pressure field emission-scanning electron microscope. Electrolyte residues from the SECCM meniscus in the hopping mode employed are observed with SEM and provide valuable information about the exact droplet size and measurement location (*vide infra*). Before each new experiment, all residues from any previous imaging are cleaned by immersing the foil in a diluted  $\text{H}_2\text{SO}_4$  solution overnight. SECCM data analysis is performed in Matlab (R2014B, Mathworks) and visualized using WaveMetrics Igor Pro software.

Electron backscatter diffraction (EBSD) images of the polycrystalline Pt sample, in the same area of the SECCM measurements, are recorded on a Zeiss SUPRA 55 FE-SEM equipped with an EDAX TSL EBSD system. Before performing EBSD measurements, the Pt foil is cleaned carefully. The measurements are carried out at 20 kV at a working distance of 25 mm on a substrate tilted at  $70^\circ$ , with a data collection step of  $2.5\ \mu\text{m}$ . The EBSD data is analyzed using Orientation Imaging Microscopy software.

## E.2 Cyclic voltammetry

Figure E.1 shows CVs of hydrazine oxidation at a Pt UME and a Pt foil in a SECCM setup. Three subsequent cycles are recorded in both experiments. Different from CVs in Fig. 4.2 (page 55), these CVs are obtained by sweeping the potential up to a higher value (1.45 V vs RHE) to oxidize the Pt surface more extensively. CVs from the Pt UME and in the SECCM setup show very similar characteristics. Independent of the cycle number, under both conditions, hydrazine oxidation shows a pre-wave peak at around 0.70 V and a diffusion-controlled plateau at high potential range. The CVs shown here are similar to the ‘stabilized’ CVs reported in a fairly recent study<sup>3</sup> which required significant pre-activation. However, unlike the results of that study, we did not observe any shifts in potentials upon repeated cycling despite some variations in electrochemical current. Thus, to limit the scan time for SECCM imaging, only a single CV (first cycle) was recorded at each pixel.

## E.3 Droplet residues

Figure E.2 shows a SEM image of a scanned area on a Pt foil after performing a voltammetric SECCM imaging in an aerated environment. The black dots are the droplet residues left on the surface due to the quick break of droplets during pipet retracting. It can be seen that the footprints of most droplets are consistent in size,

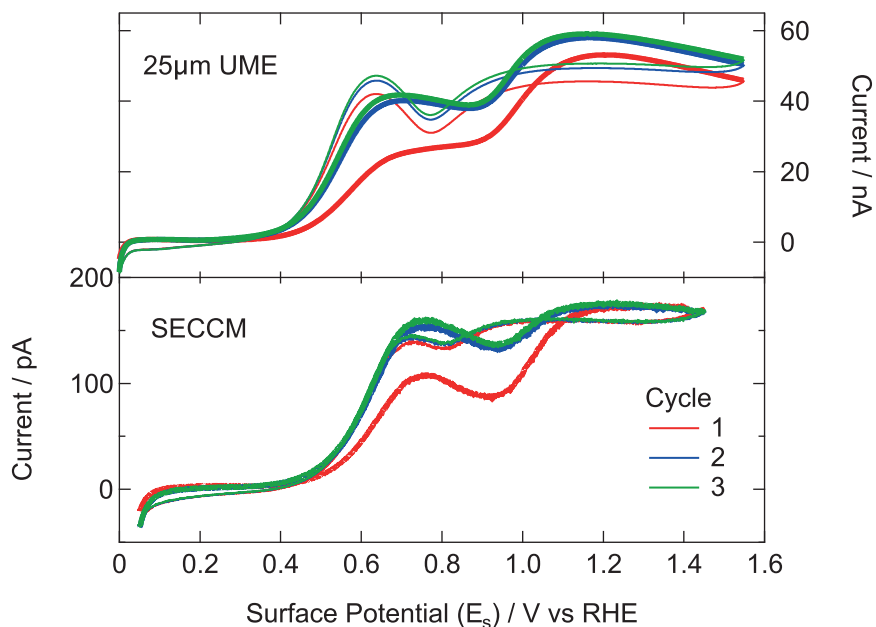


**Fig. E.1 | Hydrazine oxidation at large overpotentials:** First three CV cycles of hydrazine oxidation at a Pt UME (top) and at a Pt foil (bottom) in an SECCM setup. The thick lines indicate the anodic scan, the thin lines the cathodic scan. For both experiments, nitrogen was flowed to deaerate the electrolyte solution. The electrolyte is 2 mM  $\text{N}_2\text{H}_4$  in 0.1 M  $\text{HClO}_4$  and the potential scan rate is  $100 \text{ mV}\cdot\text{s}^{-1}$ .

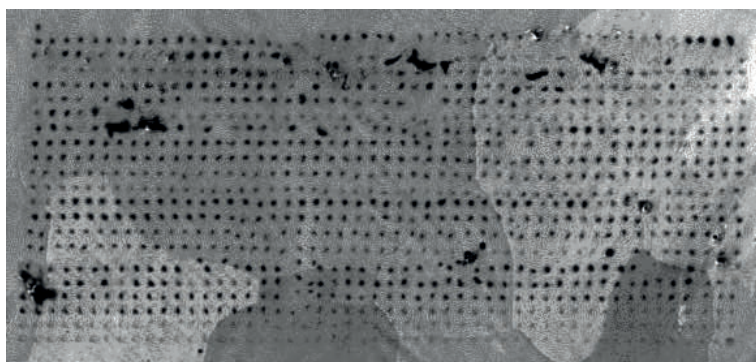


**Fig. E.2 | SECCM droplet residues:** SEM image showing the droplet residues after a SECCM imaging experiment.

indicating the stability of droplets in voltammetric SECCM imaging and, most importantly, grain structure-independent droplet wetting.

#### E.4 Quantitative multimicroscopy

The SEM data showing the SECCM droplet residues contain, as stated before, extremely useful information about the imaging experiment. Because the analysis of the data in chapter 4 is rather qualitative, no effort is made to extract all the detailed information. In the simplest case, the SEM images give the exact location of the pixels in the SECCM maps, and also give a rough indication of the stability of the droplet cell. The ion conductance current from the SECCM experiment confirms in this case the absence of any major issues with the imaging experiment.

A more detailed analysis could enable a more quantitative correlation of the observed structure-activity relationships. In such an approach, high-resolution SEM images deliver not only information on thermal drift, which distorts the SECCM maps, but also details about scanning artefacts and ‘defect’ pixels. Importantly, it would be possible to normalize the SECCM sample current to the cell footprint determined by SEM, leading to the determination of current densities. Although the 2D-interpolated and ‘raw’ maps as shown in Fig. 4.4 (page 59) are a useful, visually attractive, and (for our analysis) accurate way to represent the data, it might obscure what is really measured in the experiments. To illustrate this, Fig. E.3 shows three different representations of the data shown in Fig. 4.4. Figure E.3A shows the typical way of displaying SECCM data, a 2D interpolated version, which was also shown in Fig. 4.4. Figure E.3B is a surface-filling representation of the raw data. This visualization is particularly useful during the data analysis, because it gives a clear and quick overview of the data set. Figure E.3C shows the data in a way that is closest to the way it was truly measured. This last representation would serve best as input to apply distortion corrections and unit conversions. After processing, the 2D interpolated version could be expected to be the clearest way to represent the data. However, one should always be aware of the possible presence of highly localized effects, which could disappear upon interpolation. An example of such effects, is the increased activity of CO<sub>2</sub> electroreduction at grain boundaries of a polycrystalline gold electrode.<sup>4</sup>

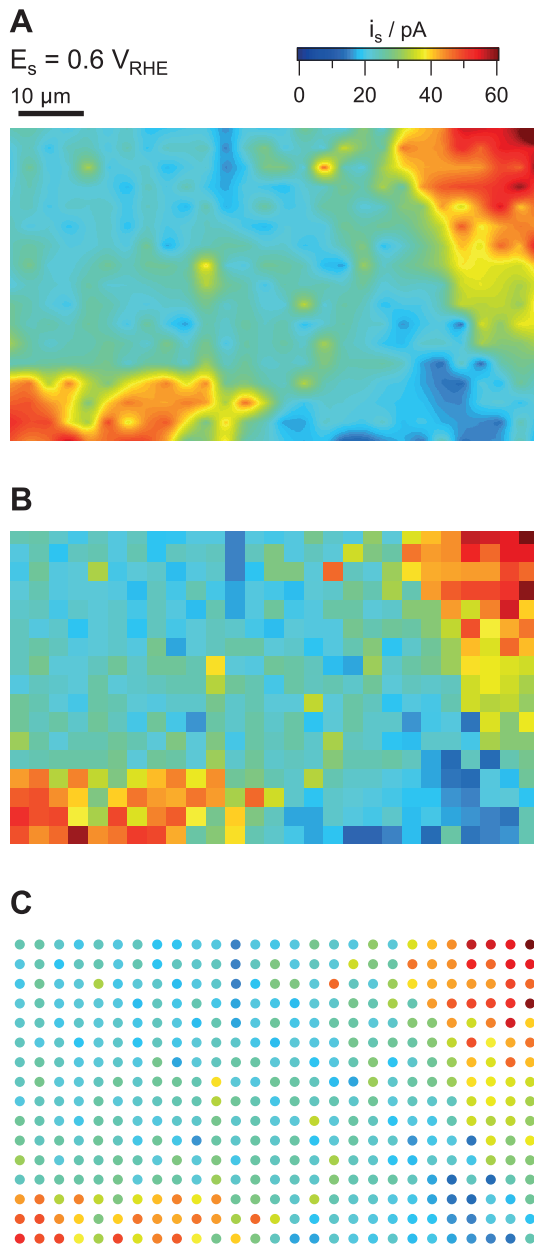


**Fig. E.3 | SECCM data visualization:** Various representations of the same SECCM data: (A) 2D linear interpolation; (B) surface filling 'raw' data; and (C) Raw data with appropriate (set) pixel position and size, which should serve as input for distortion corrections and unit conversions.

## References

1. Vasile, M. J. & Enke, C. G. The Preparation and Thermodynamic Properties of a Palladium-Hydrogen Electrode. *J. Electrochem. Soc.* **112**, 865 (1965).
2. Macpherson, J. V. & Unwin, P. R. Determination of the Diffusion Coefficient of Hydrogen in Aqueous Solution Using Single and Double Potential Step Chronoamperometry at a Disk Ultramicroelectrode. *Anal. Chem.* **69**, 2063–2069 (1997).
3. Aldous, L. & Compton, R. G. The mechanism of hydrazine electro-oxidation revealed by platinum micro-electrodes: role of residual oxides. *Phys. Chem. Chem. Phys.* **13**, 5279–5287 (2011).
4. Mariano, R. G., McKelvey, K., White, H. S. & Kanan, M. W. Selective increase in CO<sub>2</sub> electroreduction activity at grain-boundary surface terminations. *Science* **358**, 1187–1192 (2017).

## F | UME methods

UMEs were prepared from platinum wire (50  $\mu\text{m}$  diameter, Goodfellow, 99.99 %) which was electrochemically etched to the desired thickness.<sup>1,2</sup> Next, the wire was dipped in freshly prepared piranha (3:1 v/v  $\text{H}_2\text{SO}_4$  (Sigma-Aldrich, Puriss. p.a.) and  $\text{H}_2\text{O}_2$  (Merck)) for a few seconds and rinsed with ultrapure ( $>18.2 \text{ M}\Omega\cdot\text{cm}$ , Millipore Milli-Q) water. The electrode was made by sealing the wire into a soda lime glass capillary using a butane torch. The absence of bubbles surrounding the seal was confirmed using optical microscopy. A microdisk was exposed by polishing with increasingly fine-grained sandpaper, after which alumina (Kemet  $\alpha$ -alumina powder solution) or diamond paste (Kemet diamond emulsion) was used for a final polish on a microcloth (Buehler). To finish, the electrode was rinsed thoroughly with ultrapure water, acetone (Sigma-Aldrich, 99 % Puriss.) and ethanol (Sigma-Aldrich, 99.8 % Puriss. p.a.) after which it was sonicated (Branson 2510, Branson) in ultrapure water to remove any residues of the polishing process. When the UME was used for experiments, mechanical polishing and sonicating were applied only when blank voltammetry indicated this to be necessary, to increase reproducibility and ‘lifetime’ of the electrode (e.g. Pt/glass seal, surface conditions).

Different previously reported (see e.g. Ref. [2–5]) UME cleaning methods were used to prepare the UME for daily use of which the following routine gave the best and most reproducible results. At the start of each day, the UME was subsequently rinsed with ultrapure water; sonicated in ultrapure water (5 min.); cycled 500 times between 0.06 and 1.60 V vs. RHE (0.5 M  $\text{H}_2\text{SO}_4$  at  $1 \text{ V}\cdot\text{s}^{-1}$ ) to yield a blank voltammogram that was reproducible over multiple days when the same pretreatment was applied. In between experiments on the same day, the electrode was rinsed with ultrapure water and cycled (same conditions as before) 100 times. At the end of the day, the UME was cycled 500 times once again, rinsed with ultrapure water and stored in a desiccator until the next use. Adsorption of CO by bubbling through the electrolyte or from methanol decomposition followed by CO stripping, commonly used to clean Pt nanoparticles<sup>6,7</sup>, was also tested to clean the UMEs. However, this did not improve the blank voltammeteries while increasing the risk of introducing contamination. The platinum electrodes used for comparison (referred to as macroelectrode) have a much larger geometric

surface area (tens of  $\text{mm}^2$ ) than the UMEs and were cleaned by annealing in a butane flame.

All glassware was cleaned by initially boiling in a 3:1 v/v mixture of sulfuric acid (Sigma-Aldrich, Puriss. p.a.) and nitric acid (Sigma-Aldrich, ACS reagent grade) and stored in permanganate solution ( $1 \text{ g}\cdot\text{L}^{-1} \text{ KMnO}_4$  dissolved in  $0.5 \text{ M H}_2\text{SO}_4$ ) in-between experiments. Prior to each experiment, trace amounts of residual permanganate and manganese oxide were removed with dilute piranha, after which the glassware was cleaned by repeated boiling in ultrapure water. Electrolyte solutions were prepared by dissolving the appropriate amount of chemicals in 25 or 100 mL ultrapure water. The electrolyte was purged of oxygen by bubbling argon for 20 minutes.

Two different set-ups were used. The macroelectrode experiments were carried out in a two-compartment electrochemical cell with the reference separated by a Luggin capillary. Microelectrode measurements were carried out in a one-compartment cell in a Faraday cage situated on a weighted table. A Pt wire was used as a counter electrode (CE). A reversible hydrogen electrode (RHE) (blank CVs and catalytic reactions) and a  $\text{Ag}|\text{AgCl}|\text{KCl}_{\text{sat}}$  electrode (outer sphere redox reactions) were employed as reference electrodes. All potentials are reported versus the reversible hydrogen electrode scale. Potentials were controlled using a potentiostat/galvanostat from either Autolab (PGSTAT12) or Bio-Logic (SP-300).  $[\text{Ru}(\text{NH}_3)_6] \cdot 3 \text{ Cl}$  (Acros organics, 98%),  $\text{FcCH}_2\text{OH}$  (Aldrich, 97%), methanol (Fluka, 99.9% LC-MS CHROMASOLV),  $\text{N}_2\text{H}_4 \cdot \text{H}_2\text{O}$  (Sigma-Aldrich, 98%),  $\text{NaNO}_3$  (Sigma-Aldrich),  $\text{KCl}$  (Sigma-Aldrich, ACS reagent grade),  $\text{H}_2\text{SO}_4$  solution (Fluka, for trace analysis), and hydrogen and argon (Linde 6.0) were used as received.

All data shown here (except the green curves in Fig. 5.1B and 5.2 on page 72 and 75, respectively) result from a single UME. Other Pt UMEs always showed similar behavior. The geometrical surface area of the electrode was determined via the limiting current of the outer sphere redox couples, assuming a microdisk geometry. Both redox couples were measured in triplo and yielded very similar values for the disk radius ( $4.2 \pm 0.01$  and  $4.5 \pm 0.05 \mu\text{m}$  for  $[\text{Ru}(\text{NH}_3)_6]^{3+}$  and  $\text{FcCH}_2\text{OH}$  respectively). The average radius of  $4.4 \mu\text{m}$  is in line with observations from optical microscopy.

The electrochemically active surface area was calculated from the hydrogen desorption integral in the region  $0.06 < E < 0.6 \text{ V}$  after subtraction of the double layer, using the recently revisited value of  $230 \mu\text{C}\cdot\text{cm}^{-2}$  for a polycrystalline Pt

surface in sulfuric acid.<sup>6</sup> The ratio between the electrochemically active and geometrical surface area yielded roughness factors that were typically in the 10-12 range, which is reasonable comparing the size of the the UME with the polishing material.

## References

1. Forster, R. J. Microelectrodes - Retrospect and prospect. *Encycl. Electrochem.* **3**, 160–195 (2002).
2. Zoski, C. G. Ultramicroelectrodes: Design, Fabrication, and Characterization. *Electroanalysis* **14**, 1041–1051 (2002).
3. Sun, T., Blanchard, P.-Y. & Mirkin, M. V. Cleaning nanoelectrodes with air plasma. *Anal. Chem.* **87**, 4092–5 (2015).
4. Evans, S. A. G. *et al.* Detection of Hydrogen Peroxide at Mesoporous Platinum Microelectrodes. *Anal. Chem.* **74**, 1322–1326 (2002).
5. Fromondi, I., Shi, P., Mineshige, A. & Scherson, D. A. In situ, time-resolved normal incidence reflectance spectroscopy of polycrystalline platinum microelectrodes in aqueous electrolytes. *J. Phys. Chem. B* **109**, 36–9 (2005).
6. Chen, Q.-S., Solla-Gullón, J., Sun, S.-G. & Feliu, J. M. The potential of zero total charge of Pt nanoparticles and polycrystalline electrodes with different surface structure: The role of anion adsorption in fundamental electrocatalysis. *Electrochim. Acta* **55**, 7982–7994 (2010).
7. Solla-Gullon, J., Montiel, V., Aldaz, a. & Clavilier, J. Synthesis and electrochemical decontamination of platinum- palladium nanoparticles prepared by water-in-oil microemulsion. *J. Electrochem. Soc.* **150**, E104–E109 (2003).



# Summary and Outlook

Heterogeneous catalysis plays an important role in many industrial processes. Most of these processes use energy generated by the combustion of fossil fuels and can only be applied efficiently on a large scale. Using electrochemistry, it is possible to use electricity, preferably from a sustainable source, to directly drive chemical reactions. Additionally, as these processes run at low temperatures and pressures, they can easily be applied at various scales.

In most applications, the electrocatalysts will exhibit a large surface area to volume ratio, for example using nanoparticles. To fully understand fundamental electrochemical processes at the length scale of these nanoparticles, it is necessary to use specialized experimental techniques. In this thesis, the stability and activity of platinum electrode surfaces are studied at the nano- and micrometer scale using Electrochemical Scanning Probe Microscopy (EC-SPM) techniques.

Chapters 2 and 3 describe the roughening of an atomically flat Pt(111) electrode upon repetitive oxidation and reduction using Electrochemical Scanning Tunneling Microscopy (EC-STM). This potential cycling is similar to switching on and off an electrochemical device, during which significant electrode degradation is known to occur particularly at the positively charged electrode. Previous studies already showed that the roughening process leads to the formation of nanoislands on the electrode surface. However, it remained unclear how these nanoparticles nucleate and evolve during prolonged potential cycling. Also, the data available from literature was unable to explain the relationship between the changing surface structure and its electrochemical features.

In our EC-STM experiments, the overall electrochemical reactivity was measured while monitoring the evolution of the surface structure of a single (111) terrace. In Chapter 2, the total charge related to electrochemical hydrogen adsorption was correlated to the roughness of the imaged terrace. With this analysis, we demonstrated that the roughening process can be separated into two different regimes. Initially, we mainly observed the nucleation and slight lateral growth of nanoislands ('nucleation and early growth' regime). Once we could no longer distinguish the unaffected terrace between the nanoislands, the existing islands continued to grow mainly in height ('late growth' regime). In the 'late growth' regime, each newly formed surface site contributes equally to both the surface roughness and the integrated hydrogen adsorption signal, as we found a strong correlation between these two signals.

However, the overall correlation between electrochemical reactivity and surface structure, could not yet explain the complex evolution of the different hydrogen adsorption features, especially in the beginning of the roughening process. As this signal is known to be sensitive to the (local) surface structure, one would expect to be able to disentangle the different contributions. This is the topic of Chapter 3, where we show that we can extract the average atomic island structures from the EC-STM images. In these island structures, we determined the densities of various surface site geometries and correlated these to the charge belonging to the different hydrogen adsorption features. This analysis provided us with the electrochemical fingerprint of ‘defect’-, facet-, and vacancy-sites which form during the roughening process. Thus, we could pinpoint the individual peaks in the electrochemical hydrogen adsorption signal to the presence of specific surface sites. Furthermore, it also gave an insight into the stability of such sites under potential cycling conditions.

Chapter 4 zooms out a bit from the atomic level to the micrometer scale. This chapter focuses on the relationship between the grain orientation of a polycrystalline platinum electrode and its local electrochemical reactivity towards hydrazine oxidation. To study this very active catalytic system, we employed a new mode of Scanning Electrochemical Scanning Cell Microscopy (SECCM). In this mode, voltammetric SECCM, it is possible to perform a full electrochemical experiment at every position at the surface. This enabled us to visualize differences in electrochemical reactivity that would remain unnoticed in traditional, fixed-potential, electrochemical imaging.

One of the strengths of (voltammetric) SECCM is that it is easily combined with other (*ex situ*) experimental techniques or SECCM experiments. Using Electron Backscatter Diffraction, we found that the differences in electrochemical reactivity are correlated to the orientation of the grains in the sample. Furthermore, we performed the same experiment, at the same part of the sample, without a protective gas atmosphere. These experiments showed that the presence of oxygen dramatically decreases the reactivity, again in a grain-dependent manner.

With increasingly specialized experimental techniques, there is also an increased risk of introducing contaminations that strongly affect the measurement. For example, the EC-STM results presented in Chapters 2 and 3 would not have had the same value if the electrochemical signal would not have shown the features of a clean system. Unfortunately, many studies do not present their results

in such a complete way. Instead, spatially resolved data is often presented in combination with electrochemical data measured in a different experiment, using a different cell, and sometimes even using a different sample.

Similar issues play a role in many studies using ultramicroelectrodes (UMEs), as is described in Chapter 5. UMEs are very useful to overcome diffusion limitations and electrolyte resistances, e.g. in case of a highly active catalytic system and/or a weakly conducting electrolyte. However, Pt UMEs cannot be cleaned in the same way as large electrodes (by flame-annealing), which might result in a contaminated electrode surface. Moreover, they are typically characterized by measuring their reactivity using reactions that are insensitive to the surface structure or even its composition. In Chapter 5 we have shown that it is not at all trivial to obtain a sufficiently clean UME. All the commonly used cleaning methods led to blank voltammograms that are inferior to those measured on flame-annealed electrodes. As a result, UMEs showed a decreased reactivity towards surface sensitive reactions. Nonetheless, results obtained with the commonly used characterization methods were not affected at all.

## Outlook

The work in this thesis resolves several phenomena that would not be visible relying on only standard electrochemical techniques. These results are of particular interest for the communities studying fundamental platinum electrochemistry, improved fuel cell and electrolyser catalysts, and electrochemical sensors.

However, beyond the direct results presented here, it is worthwhile to also have a look at the future possibilities using these EC-SPM techniques. Although the EC-STM results were already extensively analyzed in Chapters 2 and 3, there is still much to learn from these data. Considering the roughening of the (111) terrace, it is interesting to analyze the nucleation site locations and the overall mass transport. Such analyses give insight in how and how much the electrode surface is restructured during each potential cycle.<sup>1</sup> It is expected that these phenomena are strongly influenced by the structure of the oxidized surface, which for now, still remains unresolved. In our experiments, we have not only captured the roughening of the atomically flat terrace, but also that of the step edges. As a 'real' electrocatalyst will contain many of such sites, it would be very interesting to have a more in-depth look at the nanoislands that form at the step edges. Thus, these topics are indeed the focus of current data analyses.

In a broader perspective, there is a wide variety of possible studies to perform using EC-STM. Obviously, it would be interesting to follow the surface structure while studying catalytic conversions, instead of the surface reactions studied here. Another approach would be to analyze the tip current in more detail. Although one always makes an effort to minimize the faradaic contribution to this signal, there is always a small contribution left. However, the origin of this signal is not fully understood, especially under tunneling conditions. In any case, the interaction (in terms of both current and potential) between the tip and the sample when their double layers are (almost) overlapping deserves more attention. Such studies should be able to provide insight in the possibilities to perform spatially resolved electrochemical experiments while also imaging the surface structure. The first steps in this direction are already available in the literature<sup>2</sup> and are also a topic in our own ongoing studies.

Some insights on possibilities to extract more data from the voltammetric SECCM experiments were provided in Appendix E. There, it was described that the correlation between surface topography and activity can be quantified much better by a more sophisticated analysis of the different types of available data. The (future) challenges for SECCM, and for electrochemical imaging in general, are both the resolution (both spatial and current) and imaging speed. The development of specialized probes and imaging modes have led to significant progress in recent years.<sup>3,4</sup> As an example, recent results report the activity of a single MoS<sub>2</sub> edge plain towards hydrogen evolution.<sup>5</sup> Furthermore, using fast-scanning protocols, electrochemical reactivity can be visualized during a potential sweep with a total imaging time approaching 4 s per frame.<sup>6</sup>

Finally, considering that EC-STM is most powerful for smooth, homogeneous samples and SECCM can handle rough, heterogeneous samples, these approaches complement one another. It is therefore interesting to observe that both sides are making significant progress in studying structure-activity relationships at the nanoscale. Combining the expertise on fast, high-resolution topographical imaging and handling sensitive electrochemical systems is most definitely going to help both communities push forward.

## References

1. Rost, M. J., Jacobse, L. & Koper, M. T. M. The Dualism between Adatom- and Vacancy-based Single Crystal Growth Models (to be submitted).
2. Pfisterer, J. H., Liang, Y., Schneider, O. & Bandarenka, A. S. Direct instrumental identification of catalytically active surface sites. *Nature* **549**, 74–77 (2017).
3. Frontiers in Nanoscale Electrochemical Imaging: Faster, Multifunctional, and Ultrasensitive. *Langmuir* **32**, 7993–8008 (2016).
4. Bentley, C. L., Kang, M. & Unwin, P. R. Scanning electrochemical cell microscopy: New perspectives on electrode processes in action. *Curr. Opin. Electrochem.* **6**, 23–30 (2017).
5. Bentley, C. L., Kang, M. & Unwin, P. R. Nanoscale Structure Dynamics within Electrocatalytic Materials. *J. Am. Chem. Soc.* **139**, 16813–16821 (2017).
6. Momotenko, D., Byers, J. C., McKelvey, K., Kang, M. & Unwin, P. R. High-Speed Electrochemical Imaging. *ACS Nano* **9**, 8942–8952 (2015).



# Samenvatting

Om een chemische reactie plaats te laten vinden, moeten de reagerende moleculen elkaar onder precies de juiste omstandigheden treffen. De kans dat dit spontaan gebeurt is over het algemeen zeer klein en dus is ook de reactiesnelheid erg laag. Een industrieel proces is alleen rendabel als die reactiesnelheid flink opgeschroefd wordt. Een effectieve manier om dit te bereiken, is door gebruik te maken van een katalysator. Een ideale katalysator is namelijk in staat om de reactanten bij elkaar te brengen zodat de reactie gemakkelijk verloopt, zonder daarbij zelf verbruikt te worden. Doordat katalysatoren een grote energiebesparing opleveren, worden ze toegepast in zo goed als alle chemische productieprocessen. Toch is er nog veel ruimte voor verbetering: in de praktijk blijkt dat deze katalytische processen nog steeds grote hoeveelheden energie en ook katalysatormateriaal verbruiken. Daarnaast staat de chemische industrie voor de uitdaging om haar energiebron te veranderen van fossiele brandstof naar duurzame alternatieven zoals zonne-energie. Duurzame energie wordt voornamelijk geproduceerd in de vorm van elektriciteit. Om die reden is het interessant om de directe omzetting van elektrische stroom in chemische verbindingen (en andersom) te bestuderen. Elektrochemie is het vakgebied dat zich met dergelijke omzettingen bezig houdt.

Platina is een veelgebruikte elektro-katalysator, voornamelijk bekend door de toepassing in brandstofcellen in bijvoorbeeld auto's. Helaas is platina erg schaars en kostbaar en dus is het zaak om het zo effectief mogelijk te gebruiken. Het onderzoek in dit proefschrift beschrijft fundamenteel onderzoek naar de reactiviteit en oppervlaktestructuur van platina model-elektroden en de relatie tussen deze twee eigenschappen. Hierbij maken we gebruik van technieken die vallen onder elektrochemische rastersondemicroscopie (electrochemical scanning probe microscopy, EC-SPM). Door een kleine sonde over het te bestuderen oppervlak te bewegen, is het mogelijk om de lokale structuur en/of reactiviteit van de elektrode af te beelden. In het ultieme geval kan dit zelfs met een resolutie waarbij individuele atomen van elkaar te onderscheiden zijn (in één nm kun je ongeveer 3 miljoen platina atomen naast elkaar kwijt).

Hoofdstukken 2 en 3 beschrijven de degradatie van een atomair vlak, hexagonaal georiënteerd Pt(111) oppervlak (een Pt(111) eenkristal) op atomaire schaal. Deze degradatie wordt veroorzaakt doordat het oppervlak afwisselend geoxideerd (hoge potentiaal) en gereduceerd (lage potentiaal) wordt. Dit proces is te vergelijken met wat er in een brandstofcel gebeurt op het moment dat deze aan- of

uitgeschakeld wordt. Voor deze experimenten gebruiken we een elektrochemische rastertunnelmicroscopie (electrochemical scanning tunneling microscope, EC-STM). Een EC-STM gebruikt een scherp elektrisch geleidend naaldje om het oppervlak af te tasten. Als het naaldje en het oppervlak elkaar *nét* niet raken, loopt er een kwantummechanische tunnelstroom tussen deze twee elektroden. Doordat deze stroom sterk afstandsafhankelijk is, is het mogelijk om met zeer hoge resolutie afbeeldingen van oppervlaktestructuren te maken. Meestal worden dit soort metingen onder vacuum en bij lage temperaturen uitgevoerd om de resolutie zoveel mogelijk te optimaliseren. Het bijzondere aan onze metingen is dat ze zijn uitgevoerd onder elektrochemische condities (*in situ*). Zo kunnen we de verruwing van het oppervlak stapsgewijs volgen en direct correleren aan de, tegelijkertijd gemeten, elektrochemische reactiviteit.

Hoofdstuk 2 liet zien dat er tijdens het verruwingsproces vele kleine nano-eilandjes op het oppervlak van de elektrode groeien. Tegelijkertijd was er ook een toename in de hoeveelheid waterstofatomen die elektrochemisch aan het oppervlak gebonden kan worden. De correlatie tussen deze twee signalen hielp om het totale proces te scheiden in twee verschillende regimes. In eerste instantie zagen we vooral nucleatie en, in mindere mate, laterale groei van eilanden (het 'nucleatie en vroege groei' regime). Echter, zodra het hele oppervlak bedekt was met eilanden, stopte de nucleatie en groeiden de bestaande eilanden alleen nog maar in de hoogte (het 'late groei' regime).

Hoewel deze data een goed beeld geven van de degradatie van het Pt(111) oppervlak, is de analyse nog niet gedetailleerd genoeg om de verschillende pieken in het elektrochemische signaal uit te kunnen leggen. Aangezien die pieken veroorzaakt worden door verschillende lokale (atomaire) oppervlaktestructuren, is deze informatie zeer waarschijnlijk toch uit de EC-STM data te halen. In Hoofdstuk 3 keken we dan ook in meer detail naar deze data. Na een uitgebreide analyse bleek het mogelijk de atomaire structuur van de nano-eilandjes te bepalen. Deze structuren bevatten allerlei verschillende atomaire ordeningen (zogenaamde stappen, kinks, en corners) die direct gerelateerd bleken te zijn aan de verschillende bijdragen aan het elektrochemische signaal. Ook vacatures (gaten die gevormd worden als je individuele atomen uit het oppervlak wegneemt) bleken een duidelijk herkenbaar signaal te geven.

Het goed gedefinieerde oppervlak dat gebruikt werd in de EC-STM metingen staat ver weg van een daadwerkelijke toepassing. Daarvoor zijn dit soort elektroden gewoonweg veel te duur. In een echte toepassing kun je dan ook veel meer

variëteit in oppervlaktestructuur verwachten. In Hoofdstuk 4 bestudeerden we een platina elektrode met allerlei verschillende oppervlaktestructuren (een zogenaamde polykristallijne elektrode). Om de lokale elektrochemische reactiviteit van deze elektrode te bepalen gebruiken we raster-electrochemische-celmicroscopie (scanning electrochemical cell microscopy, SECCM). In een SECCM experiment wordt de elektrochemische cel gevormd door een scherpe glascapillair met een kleine druppel elektrolyet aan het uiteinde. Alleen het gedeelte van de platina elektrode dat in contact staat met de druppel elektrolyet, kan leiden tot een elektrochemisch signaal. In onze metingen leverde dat een lokaal elektrochemisch signaal op met een resolutie van ongeveer 1  $\mu\text{m}$  (0.0001 mm).

Tot nu toe was SECCM alleen gebruikt om de reactiviteit van een elektrode af te beelden bij een constante potentiaal. Voor onze experimenten hebben we de werkwijze enigszins aangepast zodat het mogelijk is om op iedere positie op het oppervlak een volledige stroom-spannings curve (een zogenaamd cyclisch voltammogram, CV) te meten. Op deze manier hebben we laten zien dat de oxidatie van hydrazine (een mogelijke brandstof voor brandstofcellen) sterk afhankelijk is van de oppervlaktestructuur van de elektrode. Daarnaast blijkt ook dat de reactiviteit sterk afneemt in de aanwezigheid van zuurstof, en ook deze afname is structuurafhankelijk.

Voor de metingen in Hoofdstukken 2-4 zijn veel complexere experimentele opstellingen nodig dan voor standaard elektrochemische metingen zoals CVs. Daardoor neemt ook de kans op de aanwezigheid van verontreinigingen toe, wat een significant effect kan hebben op de resultaten. Voor de interpretatie van deze resultaten is het dan ook noodzakelijk om er zeker van te zijn dat dit niet het geval is. Bijvoorbeeld, de EC-STM afbeeldingen in Hoofdstuk 2 en 3 zouden veel aan waarde verliezen als we niet tegelijkertijd hadden kunnen aantonen dat het hele systeem schoon genoeg is. Helaas is deze benadering niet standaard; veel studies die specialistische technieken als EC-STM gebruiken, vergelijken hun data met metingen uit apart uitgevoerde experimenten in een andere elektrochemische cel en soms zelfs met een andere elektrode.

Vergelijkbare problemen komen voor bij de toepassing van platina ultramicroelektrodes (UMEs, zoals beschreven in Hoofdstuk 5. UMEs zijn kleine elektrodes (<10  $\mu\text{m}$ ) die veel gebruikt worden om katalytische reactiekinetiek te meten, maar ook als tip bij een ander soort elektrochemische microscopie: raster-electrochemischmicroscopie (scanning electrochemical microscopy, SECM, zie ook pagina 7). UMEs bestaan meestal uit een dun draadje, ingesloten in glas

zodat alleen de kopse kant in contact is met het elektrolyet. In kinetische studies, heeft het gebruik van UMEs verschillende voordelen bij het bestuderen van erg reactieve systemen en/of slecht geleidende elektrolyten. Het grote nadeel is dat UMEs niet gerepareerd kunnen worden in een gasvlam, wat de gebruikelijke methode is voor platina elektrodes. Vreemd genoeg gebeurt de karakterisatie van UMEs over het algemeen door de reactiviteit te meten voor reacties die ongevoelig zijn voor oppervlaktestructuur en samenstelling. In Hoofdstuk 5 hebben we laten zien dat het verkrijgen van een schoon, goed gedefinieerd UME signaal verre van zelfsprekend is. Ook tonen we aan dat UMEs relatief inactief zijn voor reacties die sterk afhankelijk zijn van de structuur van het elektrode-oppervlak, terwijl dit niet terug te zien is in de veelgebruikte karakterisatiemetingen.

Het werk in dit proefschrift geeft een gedetailleerd beeld van elektrochemische processen die moeilijk te doorgronden zijn door alleen gebruik te maken van standaard elektrochemische technieken. Onze resultaten zijn niet alleen van groot belang om fundamentele platina elektrochemie goed te begrijpen, maar zijn ook relevant voor het ontwikkelen van nieuwe generaties brandstofcellen en elektrochemische sensors. In het algemeen kan er gesteld worden dat het combineren van afbeeldingstechnieken en elektrochemische metingen leidt tot vele nieuwe inzichten over (de dynamiek van) oppervlaktestructuren onder elektrochemische condities en het effect daarvan op de elektrochemische reactiviteit.



# List of publications

## Chapter 2

Correlation of surface site formation to nanoisland growth in the electrochemical roughening of Pt(111)

Jacobse, L., Huang, Y.-F., Koper, M.T.M. & Rost, M.J. *Nat. Mater.* **17**, 277–282 (2018)

- Duurzame elektrodes voor waterstofeconomie  
Jacobse, L., Rost, M.J. & Koper, M.T.M. *Nederlands Tijdschrift voor Natuurkunde* **84**(9) (2018)
- Eilandjes van platina  
Dijkgraaf, A. *C2W* **114**(3) 15 (2018)
- Observing a changing platinum electrode  
te Roller, E., Leiden University Newsletter 2 (2018)

## Chapter 3

Atomic-scale identification of the electrochemical roughening of platinum

Jacobse, L., Rost, M.J. & Koper, M.T.M. submitted

## Chapter 4

Voltammetric scanning electrochemical cell microscopy: dynamic imaging of hydrazine electro-oxidation on platinum electrodes

Chen, C.H., Jacobse, L., McKelvey, K., Lai, S.C.S., Koper, M.T.M., & Unwin, P.R. *Anal. Chem.* **87**, 5782–5789 (2015)

## Chapter 5

The reactivity of platinum microelectrodes

Jacobse, L., Raaijman, S.J. & Koper, M.T.M. *Phys. Chem. Chem. Phys.* **18**, 28451–28457 (2016)

## Other publications

LEED analysis of a nickel cylindrical single crystal

Mom R.V., Hahn C., Jacobse L. & Juurlink L.B.F. *Surf. Sci.* **613**, 15–20 (2013)

Reaction dynamics of initial O<sub>2</sub> sticking on Pd(100)

den Dunnen A., Wiegman S., Jacobse L. & Juurlink L.B.F. *J. Chem. Phys.* **142**(21), (2015)

The molecular dynamics of adsorption and dissociation of O<sub>2</sub> on Pt(553)  
Jacobse L., den Dunnen A. & Juurlink L.B.F. *J. Chem. Phys.* **143**(1), (2015)

Coverage-dependent adsorption and desorption of oxygen on Pd(100)  
den Dunnen A., Jacobse L., Wiegman S., Berg O.T. & Juurlink L.B.F. *J. Chem. Phys.*  
**144**(24), 244706 (2016)

Highlights from the Faraday Discussion on Single Entity Electrochemistry, York,  
UK, August–September 2016  
Actis, P., Bentley, C. L., Edwards, M. A., & Jacobse, L. *Chem. Commun.* **52**,  
13934–13940 (2016)

Simultaneous scanning tunneling microscopy and synchrotron X-ray measure-  
ments in a gas environment  
Mom R.V., Onderwaater W.G., Rost M.J., Jankowski M., Wenzel S., Jacobse L.,  
Alkemade P.F.A., Vandalon V., van Spronsen M.A., van Weeren M., Crama L., van  
der Tuijn P.C., Felici R., Kessels W.M.M., Carla F., Frenken J.W.M. & Groot I.M.N.  
*Ultramicroscopy* **182**, 233–242 (2017)

Heterogeneous catalytic oxidation of simple alcohols by transition metals  
Jacobse, L., Vink, S.O., Wijngaarden S & Juurlink, L.B.F. *J. Chem. Ed.* **94**(9) 1285–1287  
(2017)

Misconceptions in the exploding flask demonstration resolved through students'  
critical thinking  
Spierenburg, R., Jacobse, L., de Bruin, I., van den Bos, D.J., Vis, D.M. & Juurlink,  
L.B.F. *J. Chem. Ed.* **94**(9) 1209–1216 (2017)

- Studenten ontrafelen werking klassiek experiment  
Moezelaar, R. *Nemo Kennislink* (2017)
- De Platina Katalysator  
Science 071, *Sleutelstad FM* (2017)
- Tweedejaars halen wetenschappelijk tijdschrift met scheikundepr  
van Dijk, J. *Leiden University Newsletter* 9 (2017)

The dualism between adatom- and vacancy-based single crystal growth models  
Rost, M.J., Jacobse, L. & Koper, M.T.M. to be submitted

# Curriculum vitae

Leon Jacobse was born on June 3<sup>rd</sup> 1990 in Rotterdam and raised in the lowest point of The Netherlands: Nieuwerkerk a/d IJssel. From 2002-2008 he performed his high school studies at the Coornhert Gymnasium in Gouda. Beyond several in-house extracurricular projects, he also participated in two projects organized by Leiden University: in 2006 he joined the Leiden Advanced Pre-university Program for TOP students (LAPP-TOP) on Astronomy; and in 2007-2008 he joined the prestigious Pre-University College, studying topics varying from philosophy to history of medicine.

It was Pre-University College that introduced Leon to the research at the Leiden Institute of Chemistry via a three-week internship in organic synthesis. This project played a significant role in his decision to start the BSc program Molecular Science & Technology in 2008. His thesis research was performed with Dr. Ludo Juurlink in the Catalysis and Surface Chemistry (CASC) group and eventually contributed to his first scientific publication.

After graduating in 2011, Leon spend a year in the board of the study association for chemistry: Chemisch Dispuut Leiden. Apart from many general activities, he was mainly involved in educational affairs. These tasks connected really well to his minor studies: Education in Chemistry, for which he spent half a year teaching chemistry at the Wolfert van Borselen high-school in Rotterdam.

For his MSc studies, Leon returned to the CASC group, collaborating with Dr. Ludo Juurlink and Angela den Dunnen. In 2013, he graduated cum laude on his research regarding the interaction between gas-phase oxygen and well-defined platinum and palladium surfaces.

Although Leon stayed within the same research group for his PhD, the type of research changed drastically from surface science to electrochemistry. Under the guidance of Prof. dr. Marc Koper he started studying the relationship between local reactivity and surface structure of platinum surfaces under electrochemical conditions. In an exchange project with the group of Prof. dr. Patrick Unwin at the University of Warwick, he contributed to the development of a new mode for imaging local electrochemical reactivity (voltammetric scanning electrochemical cell microscopy). Back in Leiden his research focused on the atomic scale surface dynamics of Pt(111) using electrochemical scanning tunneling microscopy together with Dr. Marcel Rost and Dr. Yi-Fan Huang.

During his PhD, Leon supervised several students in their research projects and contributed intensively to the 'General and Inorganic Chemistry' freshman's course. His affinity with teaching also showed within the CASC group, where he was involved in courses on the use of IGOR and LaTeX software. Finally, he gave oral presentations on his scientific results at various (inter)national conferences, among which; the annual Dutch chemistry and electrochemistry symposia (2015 and 2016, respectively); the annual meetings of the International Society of Electrochemistry in 2017 and 2018; and the spring meetings of the Deutsche Physikalische Gesellschaft in 2017 and 2018.

Starting from December 2018, Leon will continue this scientific career as a postdoctoral fellow at the DESY (Deutsches Elektronen-Synchrotron) NanoLab in Hamburg with Prof. dr. Andreas Stierle, studying model electrocatalysts under *operando* conditions.

